A Microflow Cytometry-based Agglutination Immunoassay for On-site Antigen or Antibody-based Medical Diagnosis

BY JIANXI QU, M.SC.

A Thesis Submitted to the School of Graduate Studies in Partial Fulfilment of the Requirements for the Degree of Master of Applied Science

McMaster University

MASTER OF APPLIED SCIENCE (2021) McMaster University

(School of Biomedical Engineering) Hamilton, Ontario

TITLE: A Microflow Cytometry-based Agglutination Immunoassay for On-site Antigen or Antibody-based Medical Diagnosis

AUTHOR: Jianxi Qu, M.Sc.

SUPERVISOR: Professor Chang-qing Xu

NUMBER OF PAGES: xv, 104

Abstract

On-site medical diagnosis is of great importance as it can provide cost-effective, user-friendly, and time-saving diagnosis, especially for individuals who live in resource-limited environments. The microflow cytometry-based agglutination immunoassay (MCAIA) for on-site antigen or antibody-based medical diagnosis was proposed. A method that is based on the average transit time of assay mixtures for quantitative detection of antigens of antibodies was proposed and verified by experimental results.

C-reactive protein (CRP) detection was used to illustrate the principle of antigen detection by the MCAIA. A linear relationship between the proportion of monomers and the concentration of CRP was established when data was analyzed using amplitude. A linear relationship between the average transit time and the concentration of CRP was established. A limit of detection (LOD) of 0.09 mg/L and an assay range up to 1 mg/L were achieved when data was analyzed using transit time. The total assay time was approximately 10 min and only a 10 μL sample was needed for each detection.

Severe acute respiratory syndrome coronavirus 2 (SARS-CoV-2) antibody detection was chosen as a model to demonstrate the principle of antibody detection by the MCAIA. A relationship between the average transit time and the concentration of SARS-CoV-2 immunoglobulin M (IgM) was established. A LOD of 0.06 mg/L and an assay range up to 1 mg/L were achieved. A relationship between the average transit time and the concentration of SARS-CoV-2 immunoglobulin G (IgG) was established. A LOD of 0.1

mg/L and an assay range up to 1 mg/L was achieved. The assay time of the SARS-CoV-2 antibody detection was approximately 30 min and only a 10 μL sample was needed for each test.

The proposed MCAIA can be broadly applied to other kinds of antigens or antibodies for on-site detection by replacing the corresponding antibodies or secondary antibodies specific to the targeted analyte. The compacted setup is competitive with other technologies for the medical diagnosis of antigens and antibodies.

Acknowledgements

Pursuing my master's degree at McMaster University has been an excellent experience for me. However, without the help from the following people, the project might not have come to fruition as it now has.

First, I would like to express my sincere thanks to my supervisor Dr. Chang-qing Xu. His instructive guidance greatly helped me to study in meaningful ways. His constant encouragement keeps me confident that the project was on the right track. His extensive knowledge inspired me to be enthusiastic throughout the research effort for this study. Thanks a lot, Dr. Xu.

Secondly, I would like to thank Yushan Zhang, who provided me the microfluidic chips and taught me how to operate the microflow cytometry. I want to thank Dr. Tianyi Guo, who provided help where necessary towards LabVIEW. I also need to express my gratitude to my group member Tyler Kashak who helped me with the usage of the power meter. Indeed, teamwork makes the dream work.

Thirdly, I would like to thank Mathieu Chenier, who provided many valuable suggestions for the Mitacs project about the SARS-CoV-2 antibody detection. His solid basic knowledge of Biology helped me a lot during the work. I would also like to offer appreciation to Dr. Lan Chen, who taught me to conduct flow cytometry.

Finally, a big thanks to my family, who never questioned me about my research focus, and

who have been behind the scenes supporting me since day one. Your love, encouragement, and understanding has helped me overcome a lot of difficulties. Thank you.

I deeply hope that everyone can stay safe during this pandemic, and the world will be back to normal soon.

Table of Contents

List of Figures

List of Tables

List of Abbreviations

MCAIA	Microflow Cytometry-based Agglutination Immunoassay
CRP	C-reactive protein
LOD	Limit of Detection
SARS-CoV-2	Server Acute Respiratory Syndrome Coronavirus 2
RT-PCR	Reverse Transcription-polymerase Chain Reaction
IgM	Immunoglobulin M
IgG	Immunoglobulin G
MERS	Middle East Respiratory Syndrome
MERS-CoV	MERS Coronavirus
LFIA	Lateral Flow Immunoassay
IL-6	Interleukin-6
BMI	Body Mass Index
PMN	Polymorphonuclear Leukocytes
EDTA	Ethylenediaminetetraacetate
SLE	Systemic Lupus Erythematosus
COPD	Chronic Obstructive Pulmonary Disease
AP	Acute Pancreatitis
CD	Crohn's Diseases
CVD	Cardiovascular Disease
WHO	World Health Organization
ELISA	Enzyme-linked Immunosorbent Assay
IEMA	Immunoenzymometric Assay
MBs	Magnetic Beads

DNA	Deoxyribonucleic Acid
BSA	Bovine Serum Albumin
SSC	Side-scattered
FSC	Forward Scattered
COVID-19	Coronavirus Disease-19
RNA	Ribonucleic Acid
S Protein	Spike Protein
M Protein	Matrix Protein
E Protein	Envelope Protein
N Protein	Nucleocapsid Protein
ACE2	Angiotensin-converting Enzyme 2
RBD	Receptor Binding Domain
ssRNA	Single-stranded RNA
SARS-CoV	Server Acute Respiratory Syndrome Coronavirus
PCR	Polymerase Chain Reaction
mRNA	message RNA
CT	Computed Tomography
CLIA	Chemiluminescence Immunoassay
AP	Alkaline Phosphatase
HRP	Horseradish Peroxidase
PMT	Photomultiplier Tube
DAQ	Data Acquisition
PDMS	Polydimethylsiloxane
PB	Phosphate Buffer

PBS	Phosphate Buffered Saline
MAIA	Microscopic Agglutination Immunoassay
SD	Standard Deviation
FCAIA	Flow Cytometry-based Agglutination Immunoassay
SSC-A	Side-scattered Area
FSC-A	Forward Scattered Area
H_2O_2	Hydrogen Peroxide
RFU	Relative Fluorescence Unites
AUR	Amplex Ultrared Reagent
TMB	Tetramethylbenzidine

Chapter 1 Introduction

This research discussed in this thesis aims to provide an accurate and rapid MCAIA for on-site antigen or antibody-based medical diagnoses. CRP, and SARS-CoV-2 IgM and IgG are used as two model analytes to verify this method for the quantitative detection of antigens and antibodies, respectively.

1.1 Motivation

1.1.1 The significance of on-site medical diagnosis

A testing location situated approximately 5 to 8 kilometers from a field office or laboratory is described as on-site [1]. On-site medical diagnosis provides medical diagnoses to individuals at locations other than specialized hospitals or institutions but with the same diagnostic capability. On-site medical diagnosis helps patients reduce the time they spend obtaining routine diagnoses, especially patients who live in resource-limited areas. Additionally, rapid on-site medical diagnosis is vital for the survival of individuals with not only acute diseases but also some chronic diseases; deterioration of health conditions can occur due to acute diseases and some chronic diseases can result in sudden death as well [2][3]. On-site medical diagnosis has been applied for various diseases, especially for those that require needle aspiration. Needle aspiration can provide preliminary diagnostic results, informing later clinical decisions [4]. For example, rapid on-site diagnosis of lung cancer by transbronchial needle aspirations is capable of improving the yield of diagnosis, thereby providing prompt treatment plans [5]. For infectious diseases, Y.C. *et al*. have

developed a rapid antigen detection immunoassay for on-site diagnosis of Middle East respiratory syndrome (MERS), which enabled fast screening for MERS coronavirus (MERS-CoV) infections. The MERS assay was developed based on the lateral flow immunoassay (LFIA), and the visual discernible positive or negative results can be read within 30 min. Moreover, no expensive equipment or professional technicians are required for this test [6]. H.X. *et al*. have designed an on-site diagnosis system for rapid aerosol SARS-CoV-2 nucleic acid that provides results within 15 min. The detection platform was also equipped with an on-site sampling system which can be used to monitor the spread of airborne SARS-CoV-2 [7]. On-site medical diagnosis is of great importance as it is cost-effective, time-efficient, user-friendly, and simple.

1.1.2 The requirement of on-site medical diagnosis

During the past several decades, many improvements and scientific advancements on the technology relating to medical diagnosis have been made. The realization of automation for laboratory-based testing has made testing results more reliable and time-efficient. However, the accessibility to high-level laboratory diagnosis is limited because most of the testing sites are centralized. In addition, the requirement of expensive equipment, experienced technicians, and regular maintenance of facilities make laboratory testing unfeasible for patients from some developing countries and resource-limited settings [8]. On-site medical diagnosis can provide a solution to these issues. With on-site medical diagnosis, patients can obtain testing results within one hour or less and swift measurements can be taken immediately. In general, on-site medical diagnosis should aim to be completed

within one hour, and the reliability of testing results should be comparable to other accepted methods. Moreover, the system for the diagnosis should be user-friendly and operable by workers with nonspecialized trainings.

1.2 On-site CRP detection

CRP is a well-known biomarker of inflammation or tissue damage. CRP plays a significant role in the diagnosis of some diseases. In this research, on-site CRP detection was used to verify the proposed MCAIA for on-site antigen detection.

1.2.1 The clinical significance of CRP detection

1.2.1.1 The discovery of CRP

The discovery of human CRP started with the research reported by William S. Tillet and Thomas Francis in 1930. When conducting serological reactions at the hospital of the Rockefeller Institute, they noticed that the sera obtained from patients severely diseased with lobar pneumonia were capable of precipitating with a third fraction of pneumococci. However, the precipitation phenomenon was no longer evident when the patients recovered from pneumonia. Sera of patients suffering from staphylococcus infection, streptococcus infection, and rheumatic fever precipitated the non-protein material extracted from pneumococci as well [9]. The soluble non-protein constituent of pneumococci, later named as Fraction C, was demonstrated to be a carbohydrate of Pneumococcus [10]. Further studies done by Theodore J. Abernethy and Oswald T. in 1940 showed that the reactive component in the sera, which played a role in precipitating with the C polysaccharide, was a protein and calcium ions were an indispensable part of the interaction. Additionally, they

found that the precipitation reaction, caused by bacterial infections, was a nonspecific immune reaction rather than a particular antibody-antigen interaction [5].

1.2.1.2 The structure of CRP

CRP is defined as an acute-phase protein since the serous level of CRP can increase to as high as 1000-fold within 24 to 48 hours after an individual is introduced to an infectious disease. CRP levels drop exponentially after the cessation of acute stimuli with a half-life of approximately 5 to 7 hours. The acute phase change is an expression of the host's immune response to an inflammation. Infection is not the only initiator of an acute phase response of CRP. Other conditions, such as trauma, tissue infarction, and advanced cancer can cause the changes as well [11]. Not only can CRP be categorized as an acute-phase reactant based on its well-known biological properties, but it is also a member of the pentraxin family due to its special conserved physiological structure and specific Ca^{2+}-dependent binding sites. CRP consists of five identical protomers or subunits which are non-covalently connected to each other by forming a doughnut-shaped symmetric pentameric appearance. Each subunit is made up of 206 amino acid residues and has a molecular weight of 23070 Da. The residues 36 and 78 are responsible for disulfide coupling. During the precipitation reaction, two Ca^{2+} will bind to each subunit and allow CRP to bind to ligands. If Ca^{2+} is not present, binding will not occur as this process is Ca^{2+}-dependent.

Three different forms of human CRP are shown in Figure 1-1. The rhomboid crystals of CRP, illustrated in Figure 1-1 (a), demonstrate that CRP can be effectively isolated and

crystallized from the phosphocholine-CRP complex by a designed experiment [12]. Figure 1-1 (b) shows the phosphocholine-CRP complex in the context of fully calcified CRP. Phosphocholine molecules (black and orange) are bound to a shallow site of each subunit [13]. Figure 1-1 (c) exhibits the relationship among subunits, calcium ions, and phosphocholine molecules. The phosphocholine-CRP complex is formed between human CRP and phosphocholine molecules in the presence of Ca^{2+}. Together, five identical subunits constitute a pentameric structure of CRP. Each protomer has a binding site and thus can bind a phosphocholine (grey chain-shaped molecules) in the company of calcium ions (grey spheres). The structure in Figure 1-1 (c) is reproduced from Protein Data Bank in Europe file with ID: 1B09 with permission.

(a) 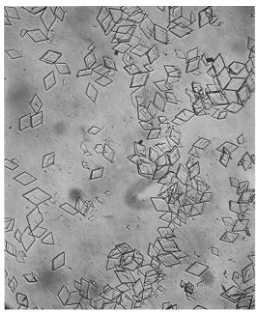 (b) 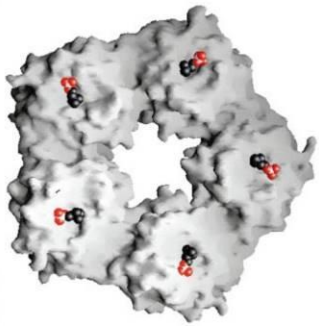 (c) 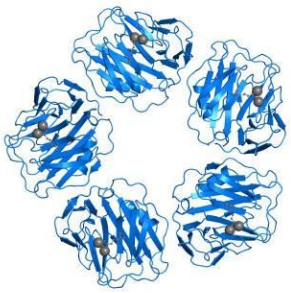

Figure 1-1: Three different forms of human CRP. (a) the crystals of CRP isolated and crystallized from human serum (× 100 magnification) [14]; (b) the binding of phosphocholine molecules (black and orange) to entirely calcified human CRP [13] (reproduce with permission); (c) the physiological structure of the human CRP complex viewed from the five-fold symmetry axis.

In different species, the following three criteria are used to evaluate whether a protein can be defined as CRP: first, it must consist of some nearly identical protomers (molecular weight of 20000 to 30000 kDa) to form a symmetrical oligomer; second, it must be capable

of binding phosphocholine in the presence of calcium ions; and thirdly, it should cross-react with human CRP.

1.2.1.3 The circulation of CRP in human

CRP is the main acute phase reactant in humans. It is primarily synthesized by the liver in response to inflammatory stimuli. Other sites, such as the kidneys, arteries, and heart, can produce CRP as well. CRP expression in human hepatic cells is mainly modulated by the inflammatory cytokine interleukin-6 (IL-6), but the inducing role of IL-6 is significantly enhanced by the cooperation of interleukin-1β. These two factors are known for their role in triggering protein production in hepatocytes [15].

In healthy normal individuals, CRP is a serum trace-element. Compared with other biomarkers, CRP levels sparsely vary over long periods of time and are unaffected by diurnal or seasonal changes. Primary research done in 1981 showed that 99% of a total of 468 normal British individuals aged between eighteen to sixty-three had serum CRP levels lower than 10 mg/L and 90% of them had the levels no greater than 3 mg/L. 0.8 mg/L CRP was the median value of the tested volunteers [16]. In 2005, a study about the distributions of CRP levels in America indicated that nearly 90% of Americans had CRP levels less than 10 mg/L. The median value of CRP in Americans was 2.1 mg/L and there were no significant racial differences. Older individuals had slightly higher CRP levels. Men had lower CRP levels than women with the median value being 1.6 mg/L and 2.7 mg/L, respectively [17]. A study about the distribution of CRP levels in 6107 Japanese adults aged older than 30 showed that a quarter of the tested subjects had CRP levels less than 0.03

mg/L. 75% of the individuals had CRP levels less than 0.3 mg/L. According to research aiming to determine the variation of CRP serum concentrations among different ethnic groups, Japanese and Chinese individuals had relatively lower CRP levels than other ethnicities. Body mass index (BMI) was determined as the main factor responsible for the ethnic variations [18].

1.2.1.4 Biologic role of CRP

CRP has various biological functions which can be categorized according to the ligands that bind to CRP, as summarized in Table 1-1. The most common function of CRP is the activation of complementary pathways. It has been reported that CRP can mediate the action of opsonin related to Streptococcus pneumoniae. Patients suffering serious diseases depleted more factors of complementary pathways. The increased depletion was also found to be related to higher concentrations of CRP in the patients [19].

Table 1-1: Biologic roles of CRP and the corresponding binding ligands

Functions	Binding ligands	Ref.
Initiate the nonimmune host to defend the microorganism	Phosphocholine moieties in the presence of Ca^{2+}	[20]
A target for polymorphonuclear leukocytes (PMN)	The Fc receptor of PMN	[21]
Modulate the process of inflammation	Ethylenediaminetetraacetate (EDTA) dependent binding of polycations	[22]
Activate the process of phagocytosis by macrophages	Stearylamine dependent binding of membranes of liposomes	[23]

CRP is known to be a nonspecific biomarker of inflammation or tissue damage. Compared with other clinical markers that reveal the acute phase response, CRP provides more

accurate sensitivity for the on-going tissue damage or inflammation. CRP is synthesized in response to various clinical situations such as inflammation, infectious diseases, trauma, malignant tumors, necroses, and even pregnancy [24]. CRP levels can be used in the following clinical circumstances: to test of the effectiveness of antibiotic therapy on patients with inflammatory or infectious diseases; to recognize the early signs of complications for patients post-operation; to observe the therapeutic effect of drugs for rheumatoid arthritis; to differentiate between some active diseases and infectious diseases; and to distinguish patients ill with graft versus host diseases from infections [25].

It has been reported that CRP levels can also be utilized to differentiate between diseases of viral origin and bacterial infections to avoid the misuse of antibiotics. Patients ill with acute bacterial infections tend to have relatively higher CRP levels than those with viral infections [26]. However, some patients acutely infected by viruses have shown to exhibit a similarly dramatic rise of CRP [27]. The amount of increased CRP presumably relies on the severity of tissue damage resulting from the attacking viruses or the defence ability of the host immune system against the viruses. Additionally, the concentration of CRP affected by acute bacterial infections does not increase significantly at the first day of infectious illness. Consequently, the tests of CRP levels should occur in concert with other medical diagnostics to improve the diagnostic accuracy [28].

1.2.1.5 The prognosis of CRP for some diseases

CRP levels play a great role in the prognosis of some diseases. Table 1-2 lists some applications of CRP measurements in clinical settings.

Table 1-2: Significance of CRP levels in various diseases

Type of diseases	Role of CRP	Ref.
Rheumatoid arthritis	Predict the risk of persistent joint deterioration; monitor the curative effect of drug treatment	[29]
Systemic lupus erythematosus (SLE)	Differentiate between intercurrent infection and mere deterioration of potential diseases	[30]
Chronic obstructive pulmonary disease (COPD)	May indicate malnutrition of patients with COPD	[31]
Acute myocardial infarction	Predict severe coronary events or test whether coronary lesions are vulnerable	[32]
Abdominal surgery	Help to exclude the occurrence of complications caused by postoperative infection	[33]
Malignancies	The ratio between CRP and albumin could be a biomarker	[34]
Acute pancreatitis (AP)	Predict the severity of AP	[35]
Sepsis	Diagnose sepsis and monitor the effect of treatment	[36]
Appendicitis	Evaluate the possibility of complicated appendicitis	[37]
Crohn's diseases (CD)	Predict mild CD or evaluate the severity of CD	[38]
Hypertension	Assist in the prognosis of hypertension	[39]
SARS-CoV-2	Predict the severity and outcome of the disease	[40]

Among all the reported diseases associated with CRP, cardiovascular disease (CVD) attracts the most attention of researchers. CVD is a group of diseases that are related to the blood vessels or the heart. CVD consists of diseases including ischemic heart disease,

stroke, rheumatic heart disease, and so on. As described by the Globe Burden of Diseases in 2016, CVD is responsible for 44% of the burden of diseases in human [41]. According to the World Health Organization (WHO) report in 2019, the leading cause of death is ischaemic heart disease which accounted for approximately 16% (8.9 million) of all recorded deaths (55.6 million) globally. However, nearly 90% of the CVD-related deaths were preventable [42].

Previous, or ongoing CVD, is the most efficient predictor of future CVD [43]. A great diversity of variables such as blood pressure, cholesterol level, diabetes, age, and smoking status can be used to screen for CVD [44]. Although these traditional predictors can be used to assess the risk of CVD, they cannot be used individually in the assessment of CVD. Massive efforts are being made to discover novel risk predictors to improve the accuracy of the CVD risk evaluation. In recent years, CRP has been constantly mentioned as a biomarker of CVD [45]. It is recommended by the American Heart Association for CRP levels to be used to evaluate the risk of CVD. CRP levels of < 1mg/L, 1 to 3 mg/L. and >3 mg/L are defined as low, medium, and high risk for CVD, respectively [46]. CRP is a promising biomarker and its predictive role of CVD can be effective when combined with other conventional CVD risk factors such as lipids in serum [47].

1.2.2 Methods for the determination of CRP levels

Since CRP levels can play a great role in medical diagnostics, various methods have been developed to precisely detect CRP. In this section, conventional methods and magnetic immunoassays based on microfluidic chips will be discussed.

1.2.2.1 Conventional methods for the determination of CRP

CRP detection methods have progressed from qualitative methods to quantitative methods since CRP was discovered in 1930. Traditional methods of CRP detection include the Quellung reaction, capillary tube precipitation method, immunodiffusion method, latex agglutination method, complement fixation test, radioimmunoassay, turbidimetry method, nephelometry method, and enzyme-linked immunosorbent assay (ELISA) [48].

Initial CRP detection methods required a significant amount of time to complete and most of them were qualitative tests. CRP was first measured by the Quellung reaction, also known as the Neufeld reaction. CRP in tested samples binds to capsules of bacteria and results in swollen capsules which can be observed by a microscope [49]. It is a qualitative method and was later replaced by agglutination-based methods. The capillary tube precipitation method is a semi-quantitative method and is based on the estimation of the presence and length of visual precipitation. First, one-third of the capillary tube is filled with CRP antiserum, and then the equal volume of a serum sample is inserted into the capillary tube by the capillary effect. The precipitation reaction will occur if the serum sample is CRP-positive and the appearance of white flocculation in the tube can be recognized by the naked eye. The semi-quantitative result can be obtained by measuring the length of the precipitate after a certain incubation time. The capillary tube is a convenient method but the assay time for the qualitative result is more than two hours and a longer time (six to eight hours) is required for the semi-quantitative result. Moreover, the sampling process needs to be precisely controlled so experienced operators are required

[50]. Radioimmunoassay is a competitive immunoassay that can be used to quantify CRP levels in a serum sample. CRP in the serum sample will partake in a competitive reaction and displace radiolabelled CRP from binding sites on antibodies. The released radiolabelled CRP will be separated from the complex. A gamma counter is used to count the radioactivity of unbound radiolabelled CRP in the supernatant. Greater amounts of CRP in a sample results in increased radioactivity due to unbound radiolabelled CRP. Although the radioimmunoassay is sensitive and can provide quantitative results with a relatively simple procedure, the radioactive material used in this assay limits its widespread application due to health concerns [51]. Immunodiffusion methods show higher sensitivity and accuracy than the rough capillary tube precipitation assay for the determination of CRP [52] [53]. Radial immunodiffusion (halo method) is a common immunodiffusion technique. To detect CRP by radial immunodiffusion, serum samples are applied to wells that are punched into the immunodiffusion plates. The plates are made of agarose which contains 1% anti-CRP antibodies. After two days incubation, precipitation rings will form due to the reaction between anti-CRP antibodies and the diffused CRP from the well. Serum CRP levels are positively associated with the diameter of the rings [53]. Although radial immunodiffusion is a relatively simple method, the time-consuming incubation and its inherent semi-quantitative characteristics limit its application. In 1986, latex agglutination was introduced as a new method to improve the efficiency of CRP detection. Latex particles are employed and modified with anti-CRP antibodies. The CRP in the tested samples cause aggregations of the coated latex particles. The degree of agglutination indicates the level of CRP in the samples. Compared with radial immunodiffusion, the incubation time of the latex

agglutination method is much shorter at less than one hour, but with inadequate sensitivity [54]. The limitations of conventional latex agglutination have been overcome by an improved latex agglutination method called the piezoelectric immunoassay. In this method, a crystal surface is covered with a thin latex film which is coated with anti-CRP antibodies. The binding of CRP to the coated antibodies causes a decrease in the oscillation frequency of the crystal due to the mass of the film [55]. The sensitivity of the latex piezoelectric assay is further improved by a modified latex piezoelectric method. A piezoelectric crystal is used to evaluate the density or viscosity difference of a solution before and after aggregates are formed by the latex particles [56]. With developments in technology, the turbidimetric immunoassay and laser nephelometry method have replaced the latex agglutination method and have become routine immunoassays for quantifying serum CRP. The turbidimetric immunoassay is a simple technique that measures the decrease in incident light resulting from scattered light produced by suspended particles in the reaction solution. Based on this assay, a linear relationship can be established between the target protein concentration and the turbidity, however, the protein must be mixed with a protein-related precipitant [57]. The principle of nephelometry is similar to turbidimetry expect that scattered light is detected instead of incident light [58]. Turbidimetry has been demonstrated to have higher precision and shorter turn-around cycles than laser nephelometry assays, and latex agglutination, therefore, is more suitable for clinical applications [59]. However, the performance of the turbidimetric assay still suffers from its inherent drawbacks, such as the matrix effect [60]. Some noise factors such as dust or large-sized agglomerates will affect the assay's the sensitivity as well. To improve the sensitivity

of CRP detection and circumvent the disadvantages above, enzyme-based immunoassays were developed. ELISA and the immunoenzymometric assay (IEMA) are two common enzyme-based immunoassays used for CRP detection. The commercial ELISA kit for CRP measurement is popular when the concentration of CRP in the sample is quite low. In this method, capturing antibodies are pre-coated on the walls of the wells in a microplate. The added CRP will bind to the immobilized antibodies. A sandwich structure of "capture antibody-CRP-detection antibody" is formed when the enzyme-coated detection antibodies are added. After the formation of the complex, a specific substrate solution is used to trigger a colorimetric reaction with the complex. The concentration of CRP is estimated by measuring the optical density of the reaction mixture, which is proportional to the level of CRP. ELISA is a competitive method for CRP detection in terms of its sensitivity, but its long detection time and complicated operations limit its on-site applications. The IEMA is another enzyme-based immunoassay for CRP detection. It is the first international standard method for human CRP measurements, approved by the WHO in 1986 [61]. The IEMA consists of two main steps. The first step is the formation of an immune complex between CRP, peroxidase-labelled antibodies, and other antibodies immobilized on the internal surface of a test tube. The second step is to cause a colorimetric reaction. The colorimetric response of a peroxidase substrate can be used to determine the concentration of the complex produced in step one [62]. The assay time of IEMA is about 30 min, which is shorter than ELISA, but limitations such as the shelf-life and degradation of the reagents diminish its use as a routine test. Table 1-3 summarizes various methods for CRP detection.

Table 1-3: Detection limit and assay range of different conventional methods for the quantification of serum CRP

Method	LOD (mg/L)	Assay range (mg/L)	Assay time	Features	Limitations	Ref.
Quellung reaction					Qualitative method	[49]
Capillary tube precipitation method			6 to 8 h for semi-quantitative detection	Visualized result	Semi-quantitative method	[50]
Radial immunodiffusion assay	1.25	1.25-150	About two days	Simple to operate	Long incubation time	[53]
Latex agglutination assay	0.01	0.01-3	Less than one day	Relative high sensitivity	Relative long assay time	[63]
Radioimmunoassay	0.05	0.05 – 10	More than 12 h	Sensitive and simple	Radiation hazard	[64]
Turbidimetric immunoassay	0.3	0.1-160	About 1 h	Requirement for clarity of the sample is not critical	Matrix effects	[65]
Laser nephelometry	0.17	0.175-1100	About 1 h	Simple and easy	Endpoint tests needed	[66]
Microplate ELISA	0.16	0.16 - 40	More than 1.5 h	Accurate and sensitive	Complicated procedure	[67]
IEMA	0.04	0.04-5	Less than 30 min	Accurate and sensitive	Degradation of the reagent	[62]

1.2.2.2 Magnetic microfluidic chip-based immunoassays for CRP measurement

To avoid the drawbacks of traditional methods for the detection of CRP, various techniques were developed to fulfill the demand of CRP measurement in different scenarios. The application of magnetic beads (MBs), microfluidic technology, and their integration has made the CRP measurement faster, more sensitive, and suitable for on-site detection [68].

The superparamagnetic feature of MBs can not only be used to couple or separate some ligands, but also used to quantify biomolecules by the application of a magnetic field or an electromagnetic effect [69].

As shown in Figure 1-2 (a), the integration of a microfluidic device and a magnetic field enables the detection of CRP. The magnetic particles are coated with anti-CRP antibodies in advance. With the application of an off-chip magnet, the introduced conjugated particles are attracted and deflected through different laminar streams consisting of the CRP sample, buffer solution, and fluorescent labelled anti-CRP antibodies. The sandwich-like immune complexes are formed during deflection, and the intensity of fluorescence derived from the complex is proportional to the concentration of CRP in the sample. The assay time for this method is less than 1 min, which greatly improved the detection efficiency. However, an external fluorescence microscope is needed for the detection, which makes this method complicated [70]. Another research team developed a magnetic particle-based on-chip immunoassay through the manipulation of MBs by using a magnetic actuation setup which is shown in Figure 1-2 (b). In this method, the introduced functionalized MBs in the microchannel are captured and accumulated on the sidewall of a microchannel. Then, the immobilized beads are perfused with the analyte to form aggregates. After the formation of the aggregates, the complexes are released by inactivating the magnetic field. The concentration of the analyte can be determined by measuring the area of the released plug in a photograph, which is associated with the extent of the agglutination. Although this method has high sensitivity, the assay time is relatively long due to the requirement of a

sufficient amount aggregates forming on the side wall. The time interval between each steps also needs to be controlled precisely to make confirm the repeatability of the result [71].

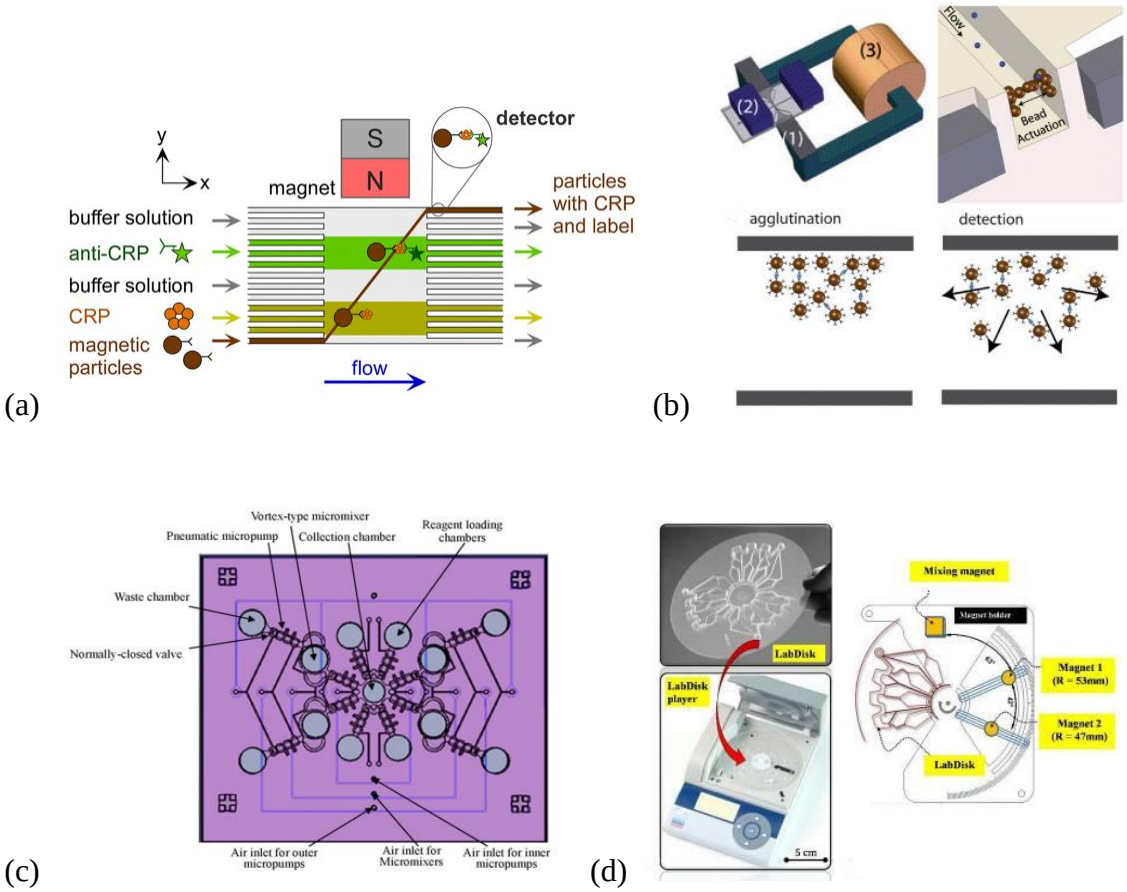

Figure 1-2: Principle of some magnetic microfluidic chip-based immunoassays. (a) trajectories of magnetic beads in continuous laminar flow by the application of an external magnet [70] (reproduce with permission); (b) schematic illustration of an on-chip immune agglutination assay with the dynamically actuated MBs [71] (reproduce with permission); (c) the design of the integrated microfluidic platform for CRP measurement [72] (reproduce with permission); (d) centrifugal microfluidic system with labdisk displayed [73] (reproduce with permission).

Figure 1-2 (c) presents a microfluidic system comprising sophisticated micromixers, micropumps and microvalves for the detection of CRP. The procedures, including coupling

deoxyribonucleic acid (DNA) aptamers of CRP to MBs, the reaction between CRP and aptamers, and the reaction between conjugated CRP and chemiluminescence-labelled anti-CRP antibodies, are all accomplished inside the chip. The CRP levels are determined by the measurement of chemiluminescence with a luminometer. Although the core component is highly compacted, the design and manufacture of the device is quite complicated [72]. Figure 1-2 (d) shows a fully automated setup with a disk-like microfluidic chip for CRP measurement. The immune reaction, including the mixing of reagents, antibody coupling to MBs, and the formation of sandwich-like complexes, is performed by employing a centrifugal and magnetic force with programmed protocols in separate chambers. Finally, chemiluminescence is detected in the detection chamber by an embedded detector to quantify CRP levels. This system is ideal for CRP measurement due to the high integrated components of the assay device [73].

Some other immunoassays for the detection of CRP are based on developed microfluidic chips or the character of MBs. One study employed a power-free microfluidic chip to realize an immunoassay for CRP measurement. The microfluidic chip is degassed in advance and reagents are introduced into the microchannel automatically because of the air pressure difference. The capillary force is used to retain solutions [74]. F.I. *et al* developed a method for the detection of CRP based on the measurement of magnetic permeability. The density of the immune complexes containing magnetic nanoparticles is measured in the form of magnetic permeability, which correlates linearly to the concentration of CRP in the sample [75].

Table 1-4: Summary of microfluidic platform-based immunoassays empolying MBs

Methods	Assay time (min)	Sample volume (μL)	LOD	Advantages	Disadvantages	Ref.
On-chip CRP assay	< 1	< 10	0.87 mg/L	Short assay time	External facilities needed	[70]
On-chip immune agglutination assay (BSA)	~ 30	< 10	0.2 μg/L	High sensitivity	Long incubation time to from detectable aggregates	[71]
CRP detection by an integrated microfluidic chip	~ 25	5	0.0125 mg/L	Integrated microfluidic platform	Relatively complicated device	[72]
Automated chemiluminescent immunoassay	~ 30	40	1.5 μg/L	Fully automated system	Long assay time	[73]
Power-free microfluidic chip-based immunoassay	~ 20	1	0.42 nM	Power-free injection system, low consumption of reagents	Pre-treatment of degassing needed	[74]
Magnetic permeability immunoassay	~ 5.5	4	3 mg/L	Whole blood test	Relatively low sensitivity	[75]
Giant magnetoimpedance-based CRP detection	Hours	5	0.001mg/L	High sensitivity	Complicated protocols	[76]
Micro-fluxgate-based CRP measurement	< 30	5	0.002 mg/L	High sensitivity, miniaturization	External equipment needed	[77]
Microflow cytometry-based immunoassay	~ 60	50	0.1 mg/L	Simple protocols	High deviations of the side-scattered (SSC) light	[78]
Sheathless microflow cytometry-based immunoassay (BSA)	~ 30	160	1.5 pM	No sheath fluid needed	Large volume of sample needed	[79]

Magnetoimpedance was also employed for the determination of CRP. The increased

amount of sandwich-shaped magnetic immune complexes enlarges the giant magnetoimpedance effect. A linear relationship between CRP concentration and giant magnetoimpedance was established [76]. An innovative fluxgate sensor-based method for CRP measurement was developed in 2018. CRP are determined by detecting the stray field of MBs from the CRP immune complexes with the designed fluxgate sensor [77]. Microfluidic platform-based immunoassays that utilize MBs for the determination of CRP are summarized in Table 1-4. Some immunoassays in Table 1-4 are used for bovine serum albumin (BSA) detection, however, the principle of the BSA detection is suitable for CRP as well.

The particle counting immunoassay is also a useful technique to measure CRP or antibodies. It is based on the theory that an agglutination decreases free particles in a reaction mixture. The extent of the immune reaction is evaluated by counting the unbound particles in the solution, therefore revealing the level of antigen or antibody in a sample [71]. The particle counting immunoassay is easily automated due to it being a homogeneous assay [80], [81]. Flow cytometry is a great method to use for the automation of the particle counting immunoassay. However, microflow cytometry provides more advantages than bulky, commercial flow cytometry. The low volume of reagents needed for each test, simple operations, short operation time, and compact size of the test apparatus make microflow cytometry a serious competitor to improve the detection of CRP [82]. The first microfluidic chip-based particle immunoassay for CRP detection was introduced in 2003, which is shown in Figure 1-3 (a). Aggregates produced by immune reaction between CRP and anti-

CRP antibody coated particles were counted by microfluidic device and SSC light of was collected. The SSC light produced by the aggregates had higher intensity than single beads, allowing monomers to be differentiated from aggregates. An approximate relationship between the intensity of side SSC light and CRP concentration was established. Although a lower bound of 0.1 mg/L CRP can be measured by this method, many of its aspects, such as bead size, experiment conditions, and the ratio between CRP and antibodies, need to be optimized. Moreover, the deviations of the intensity of SSC light need to be decreased to improve the detection accuracy [78].

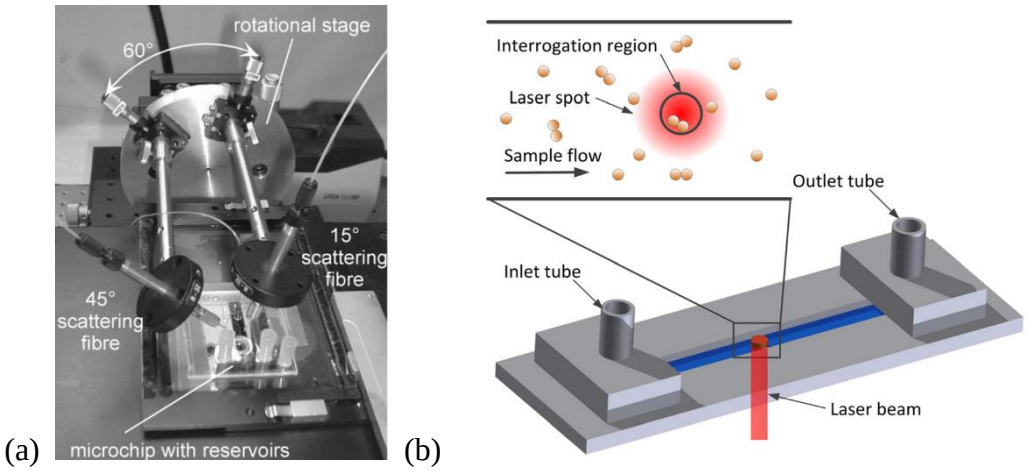

Figure 1-3: Microflow cytometry-based immunoassay for antigen measurements. (a) system setup of the microflow cytometry for aggregate counting, CRP was measured by this setup according to the principle of the particle counting immunoassay. A relationship was established between the average intensity of the 45° SSC signals and the concentration of CRP [78] (reproduce with permission); (b) a schematic of the microchip of a sheathless flow cytometry. FSC light was used to differentiate between monomers and aggregates [79] (reproduce with permission).

Another microfluidic chip-based particle counting immunoassay shown in Figure 1-3 (b) was developed in 2015. Forward scattered (FSC) light was used to distinguish immune

complexes from single beads. The concentration of analyte was determined by the proportion of single beads in the reaction mixture. The principle of this method was verified by the detection of BSA and a detection limit of 1.5 pM BSA was accomplished with the designed microfluidic device. No sheath fluid was needed in this method which made it quite simple and easy to operate [79].

1.3 On-site SARS-CoV-2 antibody detection

SARS-CoV-2 antibody detection is a useful tool for screening SARS-CoV-2 infections. The on-site SARS-CoV-2 antibody detection was used as a model to explain the on-site antibody detection by the MCAIA.

1.3.1 SARS-CoV-2 pandemic

The outbreak of coronavirus disease-19 (COVID-19) in late December 2019 has spread globally in a short time. In March 2020, the WHO declared that the outbreak of the SAR-CoV-2 virus met the epidemiological criteria for a global pandemic [83]. As of 8 March 2021, 117 million confirmed SARS-CoV-2 infections were reported, and the number of deaths caused by COVID 19 approached 2.59 million. The COVID 19 pandemic has not only affected the human health all over the world but has also left the world partially paralyzed.

Figure 1-4 shows the structure of the SAS-CoV-2 virus [84]. SARS-CoV-2 is about 100 nm in diameter, 10^6 nm^3 in volume, and 10^3 MDa in mass. The genome of SARS-CoV-2 is composed of a 29811 nucleotide-long ribonucleic acid (RNA) [85]. SARS-CoV-2 consists

of four main structural proteins which are the spike protein (S protein), matrix protein (M protein), envelope protein (E protein), and nucleocapsid protein (N protein) [86]. The 150 kDa transmembrane S protein, which is anchored in the viral surface, assists the virus in binding with the receptor of host cells, namely angiotensin-converting enzyme 2 (ACE2). The protease from the host cell cleaves the S protein into two fragments, which are the S1 and S2 domains. The receptor binding domain (RBD) from S1 participates in binding to ACE2. The function of S2 is to facilitate the transmission process between the virus and host cells [87]. The M protein is another key component of SARS-CoV-2, and it plays an important role in virus assembly and viral morphology. The M protein can combine with other structural glycoproteins and helps to keep N proteins stable [88]. The E protein is a relatively small structural protein, but it is of great importance to viral production and maturation [89]. The N protein is quite different from the other structural proteins because it is the only protein that binds to the viral RNA. The N protein participates in RNA replication and the diffusion of viral particles during viral infection [90].

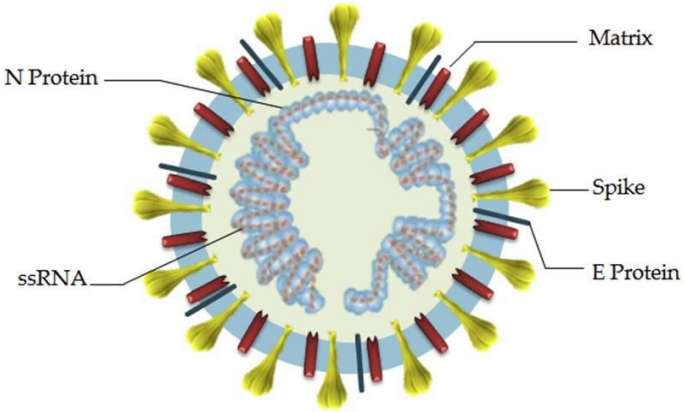

Figure 1-4: The structure of the SARS-CoV-2 virus [84] (reproduce with permission).

SARS-CoV-2 is a beta-coronavirus, which is one of four genera of large single-stranded RNA (ssRNA) viruses known as coronaviruses (the others are alpha-, gamma-, and delta-coronavirus). The main characteristic of this family of RNA virus is its high mutation rate [91]. The high-frequency of recombination and remarkable genetic variability of RNA viruses make them easier to be transmitted among animals and humans [92]. Alpha- and beta- coronaviruses are capable of infecting mammals. The animal-to-human and human-to-human transmission modes of coronaviruses have been verified by outbreaks of SARS-CoV and MERS-CoV. The infection of coronavirus can cause respiratory, hepatic, neurological, and gastrointestinal diseases to a wide variety of animals [93]. Compared to four other human coronaviruses which typically result in mild diseases such as the common cold, SARS-CoV and MERS-CoV can cause fatal respiratory diseases [94]. The WHO reports that the SARS-CoV caused 774 deaths, and 8098 reported cases among 29 countries during its 114 day epidemic starting in November 2002 [95]. MERS-CoV, which was first identified in 2012, has a very high infection fatality rate of approximately 35%. As of 31 May 2019, more than 2442 individuals have been infected by MERS-CoV and 842 deaths have been reported [91]. In late December 2019, the outbreak of SARS-CoV-2 attracted international attention and, at the time of writing, has affected nearly the entire global population. Although SARS-CoV-2 owns genetic and structural similarities to SARS-CoV, it has its own distinct characteristics. Compared with SARS-CoV, SARS-CoV-2 is more efficient at entering target cells. The RBD of SARS-CoV-2 has a stronger binding affinity to host cell receptor, ACE2, than SARS-CoV does. SARS-COV-2 is also less dependent on the protease of host cells for cell entry. Moreover, the RBD of SARS-CoV-2 has lower

exposure probability than SARS-CoV. Not only does this help SARS-CoV-2 remain potent when invading host cells but it also helps the virus 'hide' from the immune system of the host. This may explain why SARS-CoV-2 is transmitted so easily [96].

1.3.2 Methods for SARS-CoV-2 diagnosis

In response to the outbreak of SARS-CoV-2, various techniques based on either laboratory tests or rapid testing kits have been developed to quickly meet the large demand for testing. To date, RT-PCR and serological testing are two common formats for the diagnosis of SARS-CoV-2.

1.3.2.1 RT-PCR for the diagnosis of SARS-CoV-2

Polymerase chain reaction (PCR) was discovered by Kary Mullis in 1986. It is a technology that can be used to synthesize specific DNA with DNA polymerase when a template DNA molecule is provided [97]. RT-PCR is a technology that combines the conversion of sample RNA into complementary DNA and the synthesis of target DNA with PCR. The conversion process in RT-PCR is called reverse transcription. RT-PCR is a laboratory-based method that can be used for the quantification of message RNA (mRNA) [98]. Sample types including pharyngeal swab samples, nasal swab samples, sputum are usually collected for the diagnosis of SARS-CoV-2 by RT-PCR. However, some studies report that some individuals infected with SARS-CoV-2 show positive RT-PCR results with anal swab specimens but negative RT-PCR results with throat samples [99]. Anal swab specimens are required for diagnosis in some situations to improve the diagnostic accuracy. Furthermore, it is reported that some patients who are eventually confirmed to be infected by SARS-

COV-2 may show two or more consecutive negative RT-PCR results from throat swabs at the beginning of diagnosis [100]. In addition to increasing the test frequency of RT-PCR, computed tomography (CT) can be used to help improve the diagnostic sensitivity of RT-PCR. Patients infected by SARS-CoV-2 usually show pulmonary opacities in the bilateral lung field when diagnosed with CT. It is reported that the sensitivity of RT-PCR combined with chest CT is 91.86%, while RT-PCR alone has a sensitivity of 78.16%. As a genomic test, RT-PCR suffers from a relatively high false-negative rate which may be as high as 40 % for swab and sputum samples [101]. Moreover, it is difficult for genomic tests to diagnose individuals who are mildly infected with SARS-CoV-2 and analyze samples that are collected much later than the onset of the infections. Additionally, it is difficult for RT-PCR to provide the exposure history and immunity of individuals who have recovered from SARS-CoV-2 as viral RNA level are not typically be detectable after recovery.

1.3.2.2 Serological assays for the detection of SARS-CoV-2 antibodies

Serological testing is another potent tool for the screening of SARS-CoV-2 infections. The exposure history and immune status of individuals to SARS-CoV-2 can be assessed by this technique. In addition, it can be used as a complementary technique to RT-PCR. Different from genomic tests, such as RT-PCR which detects the existence of SARS-CoV-2 viral RNA, SARS-CoV-2 antibodies are detected by serological assays after seroconversion occurs. Normally, SARS-CoV-2 IgM and IgG are used as the indicators of infection when antibody tests are performed. SARS-CoV-2 IgM is typically produced by the host prior to the other antibody isotypes as it acts as a first line of host defense against the virus.

Compared with the short-lived IgM response, SARS-CoV-2 IgG response is relatively durable [102]. In general, the medium seroconversion time for SARS-CoV-2 IgM and IgG occurs four to six and five to ten days after the onset of symptoms, respectively [103]. Figure 1-5 shows the estimated dynamics of SARS-CoV-2 RNA, IgG, and IgM levels since the onset of infection. Viral RNA is detectable in the initial phase of the infection and will reach its peak value in less than seven days. IgM is initially produced around the fifth day, followed by a persistent IgG response one to two days later. However, it should be noted that there is a delayed antibody response against the SARS-CoV-2 virus compared the innate immune system. This delay is called the window period, during which antibodies are not detectable. False-negative results from serological assays are likely to occur during this time [104].

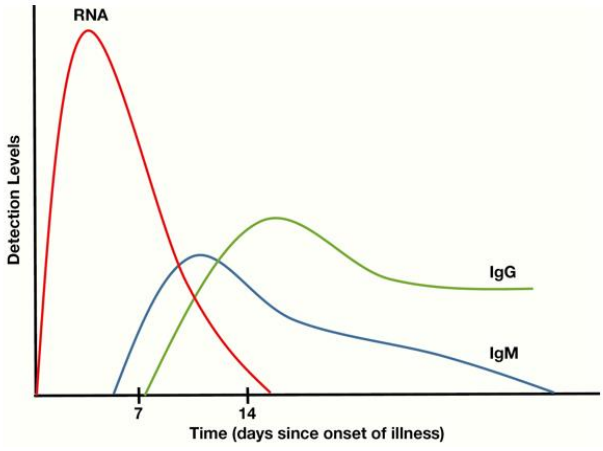

Figure 1-5: The dynamics of SARS-CoV-2 RNA, IgM, and IgG since the onset of infection [104] (reproduce with permission).

At present, the neutralization assay, ELISA, LFIA, and chemiluminescence immunoassay (CLIA) are four main formats of serological assays used for the detection of SARS-CoV-2

infections [105].

The neutralization assay for SARS-CoV-2 detection is a laboratory-based *in vitro* test that is used to detect the presence and level of SARS-CoV-2 antibodies that are capable of blocking virus replication or inhibiting viral infection. However, the neutralization assay must be conducted in a designated biosafety level laboratory because live SARS-CoV-2 virus is highly pathogenic and infectious. Additionally, the assay time is approximately three to five days, which limits its application [106].

ELISA is a highly sensitive method that can be used for the quantitative detection of SARS-CoV-2 antigens or antibodies. According to the formation of the immune complex, ELISA can be divided into four different types: direct, indirect, sandwich, and competitive. ELISA is a colorimetric method which is usually performed with a multi-well plate. The concentration of the analyte is proportional to the color change the results from an enzymatic reaction. The color change is detected by a spectrophotometric method. As shown in Figure 1-6, direct ELISA is designed for antigen detection. Targeted SARS-CoV-2 antigens are pre-coated on the surface of a well and are detected by the addition of enzyme-conjugated antibodies specific for the antigens. Indirect ELISA can be used for either antigen or antibody detection. Antigen detection by indirect ELISA is similar to direct ELISA, except that the conjugated primary antibodies are replaced by a two steps antibody conjugation process. The indirect ELISA can be altered for the detection of SARS-CoV-2 antibodies by replacing the primary antibodies with the sample containing the targeted antibodies. The following protocol will use SARS-CoV-2 spike IgM as an

example analyte to illustrate the indirect ELISA's basic principle. The first step is the spike antigen coating. The spike antigens are immobilized to the surface of a well during a certain incubation time. The next step is antibody binding. A sample containing the IgM is added into the well and the IgM is captured by the immobilized antigen. After the antibody incubation, detection antibodies, which are conjugated with an enzyme such as alkaline phosphatase (AP) or horseradish peroxidase (HRP), are then added into the well and are bound to the captured IgM to enable their detection. After incubating detection antibodies, a colorimetric substrate is added to the well and is catalyzed by the enzyme to change the color of the solution. The target IgM can be identified and quantified by the optical density of the colored solution when a stop solution is added. Compared with direct ELISA, with indirect ELISA more than one secondary antibody can be bound to the primary antibody, so the signal can be amplified. Sandwich ELISA is the most frequently used method for the detection of antigens or antibodies. Compared with direct or indirect ELISA, the introduction of matched antibodies that target different epitopes of the antigen can improve specificity. Competitive ELISA is designed for the detection of small antigens. In competitive ELISA, target antigens compete with the immobilized reference antigens for the enzyme-labeled antibodies. The concentration of the target antigen is negatively correlated with the signal intensity as the immune complexes consist of the reference antigen and the labeled antibody. Although ELISA is famous for its high sensitivity, it has disadvantages such as labour-intensive procedures, time-consuming incubations, the requirement for skilled operators, and potential cross-reactivity of the detection antibody. Moreover, it is a laboratory-based immunoassay which means it cannot satisfy the massive

need for an effective testing for SARS-CoV-2 infections [105].

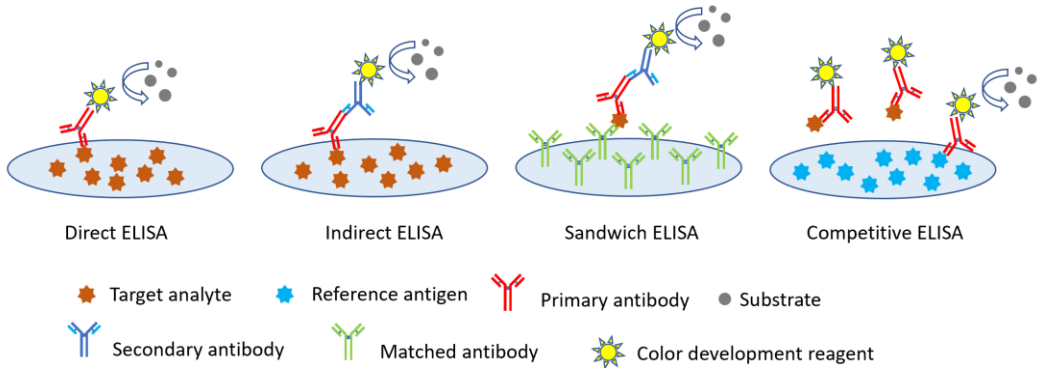

Figure 1-6: Four different types of ELISAs.

LFIA is another format of serological assay for the detection of SARS-CoV-2 antibodies. It is qualitative or semi-qualitative method. The LFIA is an immunoassay that is performed on a strip. Typically, the strip consists of four units: a sample pad, conjugate pad, nitrocellulose membrane, and absorbent pad (Figure 1-7). The conjugate pad is loaded with dehydrated coating antibodies which are tagged with colorimetric labels such as colloidal gold. Generally, there is a test line and control line within the nitrocellulose membrane. The test line is composed of capture antibodies and the control line is coated with secondary antibodies. The absorbent pad is responsible for causing the sample to flow through the strip. The principle of LFIA is quite simple. For example, when SARS-CoV-2 IgG is to be detected by a LFIA, a sample possibly containing human SARS-CoV-2 IgG is loaded to the sample pad and flows towards the absorbent pad due to capillary action. The conjugate pad is coated with lanthanide-doped nanoparticle-labeled anti-human IgG and lanthanide-doped nanoparticle-labeled rabbit IgG. The human SARS-CoV-2 IgG in the sample will interact with the labeled anti-human IgG and form immune complexes. The labeled rabbit

IgG, along with complexes, will migrate towards the absorbent pad. When the sample passes through the nitrocellulose membrane, the immune complexes will be captured by the human SARS-CoV-2 specific antigens within the test line. The accumulation of the immune complex in the test line will result in a color change of the line and thus provide a positive result. The anti-rabbit IgG immobilized on the control line will capture the labeled rabbit IgG antibodies released from the conjugate pad. A colored control line demonstrates that the LFIA strip adequately functioned [107]. The LFIA is a useful format for individuals who live in resource-limited environments or where RT-PCR is not readily accessible. It is simple, inexpensive, rapid, and suitable for point-of-care detection. However, the LFIA is limited by its relatively low sensitivity and its inability to provide quantitative results.

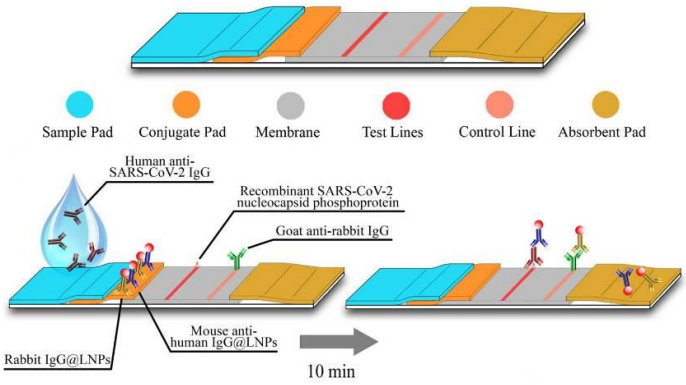

Figure 1-7: The principle of the LFIA for SARS-CoV-2 IgG detection [107] (open access).

CLIA is an assay format which combines chemiluminescence with immune reactions. The CLIA is similar in principle to ELISA, however, the antibody in a CLIA is labeled with chemical probes which can emit light upon a chemical reaction. Compared with absorbance-based techniques, such as ELISA, luminescence-based CLIA detection is more

competitive as it measures absolute value instead of relative value of the light signal [108]. Table 1-5 presents a summary of serological assays for SARS-CoV-2 detection.

Table 1-5: Summary of independent evaluations of some leading SARS-CoV-2 serological assays

Manufacturer	Target antibody	Principle	Sensitivity (%)	Specificity (%)	Antigen	Infective stage	Ref.
Epitope Diagnostics	IgG	ELISA	73	99.6	Spike protein	Entire	[109]
Wantai	Total Antibody	ELISA	90	100	Spike protein	Entire	[110]
Euroimmun	IgG	ELISA	87.8	68.3	Spike protein	11 to 13 days	[111]
MGH/Ragon	IgG	ELISA	89	100	Spike protein	7 days	[112]
	IgM		89	92			
Acro Biotech	IgG	LFIA	56.1	74.4	N/A	11 to 13 days	[111]
	IgM		46.3	69.5			
Xiamen Biotime Biotechnology	IgG	LFIA	71.9	97.5	Spike protein	11 to 13 days	[111]
	IgM		81.3	88.8			
Biolidics Ltd.	IgG	LFIA	88	100	N/A	7 days	[112]
	IgM		54	92			
Abbott Laboratories	IgG	CLIA	100	99.9	Nucleocapsid protein	> 17 days	[113]
Shenzhen YHLO Biotech	IgG	CLIA	76.7	100	Nucleocapsid protein and spike protein	8 to 17 days	[114]
	IgM		73.3	100			
DiaSorin	IgG	CLIA	97	99	Spike protein	> 14 days	[115]
Ortho-Clinical Diagnostics	IgG	CLIA	97.3	99.6	Spike protein	Entire	[109]

The two major proteins used as antigens in the serological assay for SARS-CoV-2

antibodies are the spike and nucleocapsid protein [116]. L.W. *et al* evaluated the diagnostic feasibility of these two proteins. The spike protein-based ELISA for the SARS-CoV-2 antibody (IgG and/or IgM) detection has a positive rate of 82.2%, which is 1.8% higher than that of nucleocapsid protein. Furthermore, the spike protein-based ELISA has much higher sensitivity than that of the nucleocapsid protein regarding IgM detection [106].

1.3.3 The importance of on-site SARS-CoV-2 antibody detection

Globally, SARS-CoV-2 has caused severe mortality. Methods with high sensitivity and specificity for the diagnosis of SARS-CoV-2 are urgently needed. Although various molecular testing formats are available and RT-PCR remains the most common method for the diagnosis of SARS-CoV-2 infections, the significance of on-site serological assays for the detection of SARS-CoV-2 antibodies cannot be ignored. Compared with RT-PCR which requires different kinds of swabs, the sampling procedure for on-site SARS-CoV-2 antibody testing is quite simple. On-site SARS-CoV-2 antibody detection can also promptly provide valuable information regarding the exposure history and immunity of individuals, and can be a potent and supplementary technique for the diagnosis of SARS-CoV-2 infections [117].

1.4 Proposed method

A MCAIA for the on-site determination of antigen or antibody was proposed. It is based on the principle that the immune reaction will decrease the number of free particles in the assay mixture, which can be used to evaluate the extent of the reaction and thus determine the concentration of the analyte. The microflow cytometry was used to count the aggregates

in the assay mixture. The transit time was used to differentiate between monomers and aggregates. The proposed MCAIA provides a rapid, sensitive, and accurate technique for the on-site detection of antigen or antibody. The compacted system and the simple protocols make the MCAIA become a strong competitive tool for the detection of antigen or antibody, which will maximize clinical significance and diagnostic value of its on-site medical diagnosis.

Chapter 2 The MCAIA

In this section, the principle of the MCAIA for the detection of antigens and antibodies will be described separately. The system setup of the MCAIA will be introduced as well.

2.1 The principle of the MCAIA

2.1.1 Particle counting immunoassay

Microflow cytometry is a potent tool for particle counting. The MCAIA is the combination of microflow cytometry and the particle counting immunoassay. It is based on the particle counting immunoassay that the concentration of the targeted analyte can be quantified by the extent of the reaction. The decrease of monomers caused by agglutination is indicative of the extent of the reaction. A correlation can be found between the concentration of the analyte and the number of monomers in the assay. Monomers refer to unconjugated free particles in the assay [118].

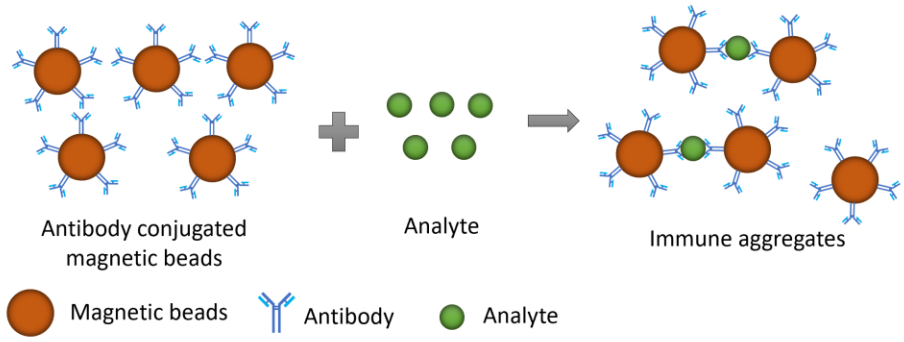

Figure 2-1: Schematic illustration of the particle counting immunoassay. The anti-analyte antibody conjugated MBs can form aggregates in the presence of the analyte.

Figure 2-1 shows the principle of the particle counting immunoassay. The addition of target analyte will cause agglutination and thus decrease the number of monomers in the assay. The conjugated antibody is specific for the targeted analyte.

2.1.2 System setup of the MCAIA

Figure 2-2 shows the system setup of the MCAIA. The setup consists of a syringe pump system, a microfluidic chip, a light source, an external optical system, and a data collection and process system. After the preparation of the assay mixture, the mixture was introduced to the microfluidic chip by the sample syringe (Model 22, Harvard Apparatus, Holliston, MA, USA). The sample flow was confined into the center of the microchannel by two sheath flows with two-dimensional hydrodynamic focusing. The flow rate of the sample and sheath flows could be set separately. The MBs in the sample flow were forced to flow through the interrogation region and detected by a 532 nm green laser. The light emitted from the laser was coupled into the chip with the embedded input waveguide. The guided light was then focused to the interrogation area by the integrated lens system in the chip. The intersection between the light beam and the sample flow is defined as the interrogation area. The interrogated aggregates in the sample stream interacted with the coupled laser beam, producing the SSC light. An objective (25 × magnification) mounted perpendicular to both the laser beam and the channel was used to collect the SSC. The SSC was further deflected by a mirror and then amplified by a photomultiplier tube (PMT) (Newport Corp, Irvine, CA, USA). An optical bandpass filter (522 nm - 542 nm) was used to filter the SSC. The amplified current signals from the PMT were further converted to amplified voltage

signals by a current-to-voltage amplifier (428, Keithley, Cleveland, OH, USA). A data acquisition board (DAQ) (USB-6211, National Instruments, Austin, TX, USA) was used to digitize the amplified voltage signals. Finally, the data was processed by a custom LabVIEW (National Instruments, Austin, TX, USA) program.

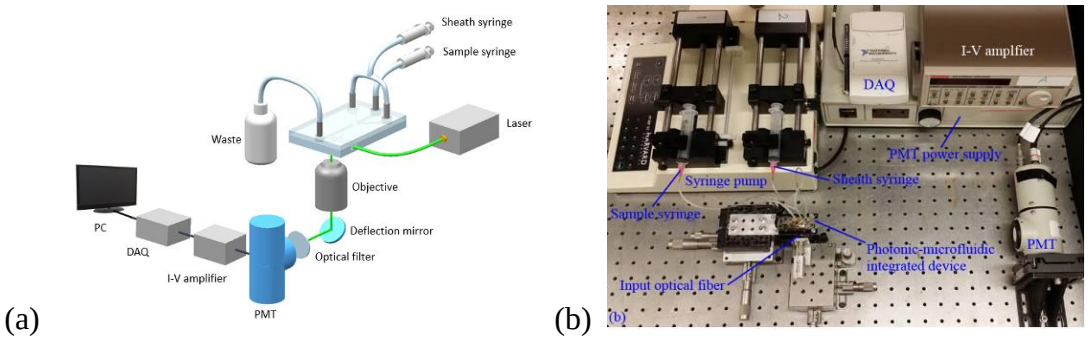

Figure 2-2: (a) a schematic diagram of the MCAIA setup [119] (open access); (b) a picture showing the MCAIA setup with the essential devices (open access).

2.1.3 The microfluidic chip

Figure 2-3 (a) shows a photo of the microfluidic chip, which is the core device of the MCAIA. The chip was made with photolithography technology. The chip is comprised of five layers; from bottom to top which are Pyrex glass, SU-8 3035 photoresist, SU-8 2035 functional photoresist, polydimethylsiloxane (PDMS), and glass. The Pyrex glass was used as the substrate for the chip. The approximately 600 nm thick SU-8 3035 layer was responsible for facilitating the adhesion between the SU-8 2035 layer and the Pyrex glass. The 50 μm thick SU-8 2035 layer was patterned with the structure of the microchannel by negative photolithography. PDMS was used to seal the SU-8 2035 layer to form the microchannel structures. The holes in the PDMS, which are reserved for the inlets and

outlet, were fabricated by pouring the liquid PDMS into a mold containing the negative of the inlets and outlet. The glass on the top of the chip, which was drilled with holes aligned to the inlets and outlet, was used to facilitate the fixing of the metal pins. The metal pins inserted into the PDMS were used as the inlets and outlet of the chip. The dimension of the chip is approximately 2.5 cm × 2 cm × 0.4 cm (length × width × height). The microchannel has a cross-sectional area of 50 µm × 100 µm (height × width). Details of the fabrication of the device were presented in a previous publication [120]. To visualize the hydrodynamic focusing of the chip, a sample containing blue ink was introduced into the microfluidic chip and confined into the centre of the channel. The flow rate of sample and sheath flows were set as 200 µL/h and 800 µL/h, respectively.

(a) 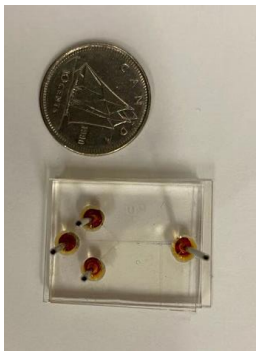 (b) 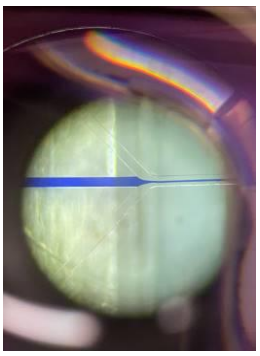 (c) 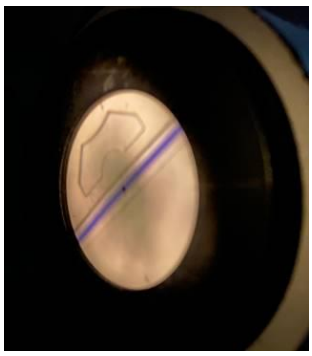

Figure 2-3: (a) a picture of the microfluidic chip; (b) a picture of the two-dimensional hydrodynamic focusing of the Y-shaped junction in the channel. The sample was saturated with blue ink to visualize the focusing; (c) a picture taken in front of the PMT when the blue colored sample passed through the interrogation region.

As shown in Figure 2-3 (b), the blue sample flow in the centre of the channel was confined by the sheath flows. Figure 2-3 (c) shows the projection of the blue sample flow in the microchannel and the embedded lens system of the microfluidic chip. The SSC light signals

will pass through the pinhole and then be amplified by the PMT.

2.2 The antibody coupling procedure

The first step for both antigen and antibody detection by the MCAIA is antibody coupling. Dynabeads M-270 Epoxy MBs (14302D, Thermo Fisher Scientific, Burlington, ON, Canada) with a diameter of 2.8 μm were used as the solid support for the antibody coupling. The surface of the uniform and superparamagnetic particles is modified with epoxy groups, which can enable the immobilization of antibodies to the surface of MBs through covalent binding. The coupling procedure is performed according to the user manual provided by the MBs manufacturer, which is shown in Figure 2-4. The following procedure was used to prepare 5 mg of conjugated MBs. First, 5 mg of MBs were weighed and transferred to a 1.5 mL centrifuge vial. Afterwards, 1 mL of 0.1 M sodium phosphate buffer (PB) (P5244, Millipore Sigma, Oakville, ON, Canada) was added into the vial to resuspend and wash the MBs. After a 30 s vortex and 10 min incubation for the MBs, a magnet was applied to the outside wall of the vial for 1 min and consequently, the MBs were attracted to the wall of the vial. Then, the supernatant was removed by a pipette. The 5 mg of MBs were used to couple 100 μg of antibody. The volume of antibody needed was calculated based on the concentration of the antibody. The MBs were then resuspended in PB to a volume equal to that of the antibody to be added. Based on the calculation, a certain volume of antibody was added into the vial with complete mixing, followed by the addition of an equal volume of 1 M ammonium sulfate buffer (A4418, Sigma-Aldrich, Oakville, ON, Canada). The solution was mixed and then incubated at 37 ℃ for 24 h. After the incubation, the

supernatant was removed by magnetic separation. The conjugated MBs were then washed by 1 mL of buffer 3 four times. Finally, the washed conjugated MBs were resuspended in a desired volume of phosphate buffered saline (PBS) (PBS405.1, Bioshop, Burlington, ON, Canada) with 0.1% BSA (15561020, Invitrogen, Thermo Fisher Scientific, Ottawa, ON, Canada) and 2 mM sodium citrate solution (W302600, Sigma-Aldrich, Oakville, ON Canada). The concentration of the lyophilized MBs was approximately 6.7×10^7 beads/mg. 330 µL of the conjugated MBs solution provided a concentration of approximately 1×10^7 beads/mL. The conjugated MBs were then ready for the MCAIA. The conjugated MBs need to be stored between 2 to 8 ℃. An addition of 0.02% (*w/v*) sodium azide (S2002, Sigma-Aldrich, Oakville, ON, Canada) will lengthen the shelf-life of the conjugated MBs, but the MBs will need to be washed with PBS before being used in the MCAIA.

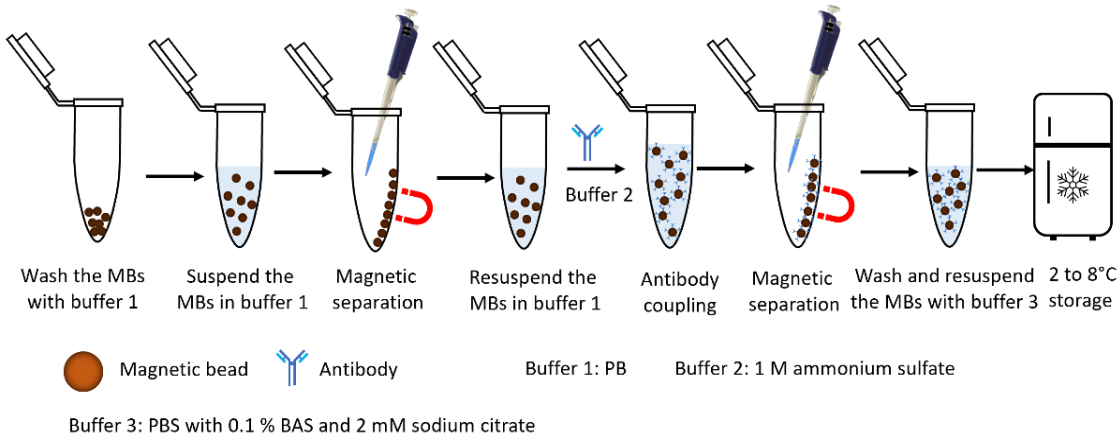

Figure 2-4: Schematic illustration of the antibody coupling procedure for 2.8 µm MBs.

2.3 The procedure for antigen detection by the MCAIA

Figure 2-5 shows the procedure for antigen detection by the MCAIA. After coupling to

antibodies specific to the targeted antigen, a certain volume of the conjugated MBs was transferred to a microcentrifuge vial. The following step involves the MB washing and dilution process. Because the MBs were stored in a buffer containing sodium azide, the washing of the conjugated MBs with PBS was conducted to reduce the effect of sodium azide in the subsequent agglutination process. After washing, the MBs were diluted with PBS to an optimal concentration. The concentration may vary for different kinds of targeted antigens. The diluted MBs were then vortexed for 10 s and sonicated for 10 s to suspend the MBs more uniformly in the PBS. A sample containing the targeted antigen was added into the vial with thorough vortex mixing for 10 s and then the vial was left to incubate for a certain amount of time. During the incubation, aggregates were formed among the MBs. After the incubation, the assay mixture in the vial was transferred to a pipeline which was connected to the sample syringe of the MCAIA. PBS was used as the sheath flow for the

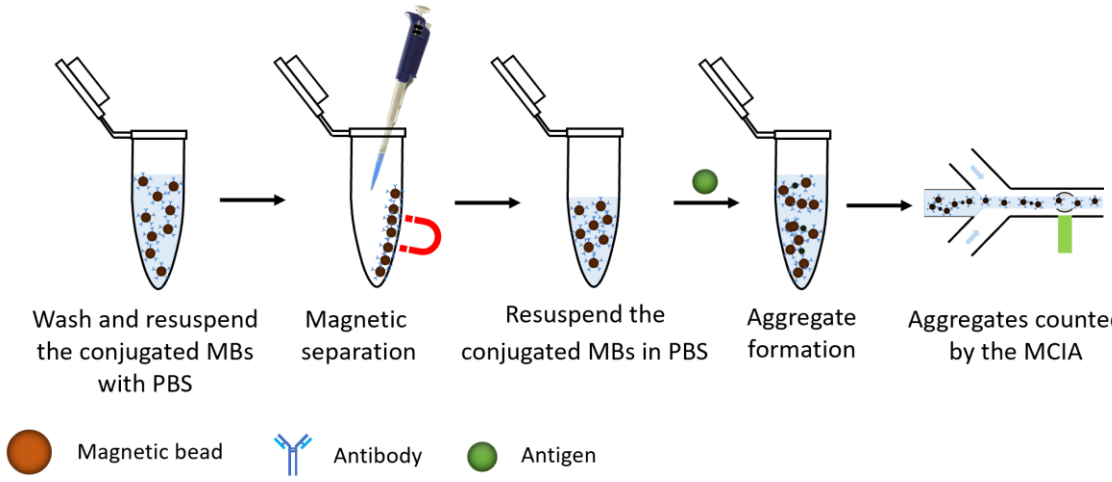

Figure 2-5: Schematic illustration of the MCAIA for antigen detection

MCAIA. The flow rate of sample and sheath flows were set to 200 µL/h and 800 µL/h,

respectively. Data was collected by the DAQ over a two-minute period and analyzed by the custom LabVIEW program. The procedure described above is adaptable to the detection of other antigens only by changing the type of the antibody to be conjugated.

2.4 The procedure for antibody detection by the MCAIA

Figure 2-6 shows the procedure of antibody detection by the MCAIA.

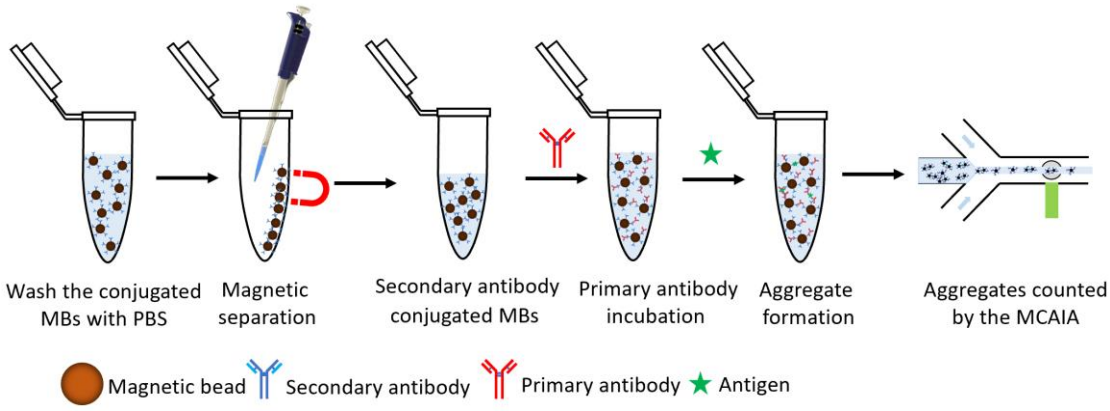

Figure 2-6: Schematic illustration of the MCAIA for antibody detection

The first step is the secondary antibody coupling, which is a procedure that was described in section 2.2. After the secondary antibody coupling, the conjugated MBs were washed by PBS once and then diluted by PBS to an optimal concentration. There may be some nonspecific agglutination or self-coagulation due to long-term storage. Then, 10 s of vortex mixing, and 10 s of sonication were applied to the diluted MBs solution, which generated a more uniform MB suspension in the PBS. After the preparation of the conjugated MBs, a sample containing targeted antibodies was added into the same vial, which was then subject to vortex mixing for 10 s. The mixture was then incubated for a certain amount of

time. The target antibodies were captured by the specific conjugated secondary antibodies which were immobilized on the surface of the MBs. After the antibody incubation, a certain volume of antigen specific to the target antibody was added into the vial and incubated for a certain amount of time. MBs aggregates were formed during this step. After the antigen incubation, the assay mixture was transferred to the pipeline which was connected to the sample syringe. The PBS sheath flow was used to confine the sample flow into a narrow stream in the microchannel using two dimensional hydrodynamic focusing. The flow rate of sample and sheath flows were set to 200 µL/h and 800 µL/h, respectively. The assay mixture was counted by microflow cytometry. Data was collected by the DAQ over a two-minute period and then analyzed by the custom LabVIEW program.

Chapter 3 The MCAIA for CRP Detection

CRP is a significant biomarker of tissue damages and infections. It plays an important role in diagnosis of some diseases. In this chapter, CRP detection is used as a model to verify the proposed MCAIA for antigen detection.

3.1 Microscopic agglutination immunoassay (MAIA)

The MCAIA for CRP detection was verified by the particle counting immunoassay first. Immune aggregates were formed by the immune reaction between CRP and the anti-CRP antibody conjugated MBs. The aggregates formed during the immune reaction were observed by the microscope (Eclipse E200, Nikon, Mississauga, ON, Canada) and counted by a hemocytometer (Z359629, Millipore Sigma, Oakville, ON, Canada).

3.1.1 Anti-CRP antibodies coupling

The first step of the agglutination immunoassay is the antibody coupling. Section 2.2 describes the antibody coupling procedure of 2.8 μm MBs for the MCAIA. In fact, three different sizes of MBs including 1 μm, 2.8 μm, and 4.5 μm have been tested to find the optimal size of the MBs. For the particle counting immunoassay, 4.5 μm MBs were tested first as it can provide a better visualization of the aggregates. The procedure of antibody coupling to 4.5 μm MBs is different from the lyophilized 2.8 μm MBs as the purchased 4.5 μm MBs were provided in a liquid solution. Therefore, it is necessary to describe the coupling procedure of 4.5 μm MBs. Figure 3-1 shows the anti-CRP antibody coupling procedure of 4.5 μm MBs. Dynabeads M-450 Epoxy beads (14011, Thermo Fisher

Scientific, Burlington, ON, Canada) were used as the physical support for the coupling of anti-CRP antibodies (PA1-29087, Thermo Fisher Scientific, Burlington, ON, Canada). The surface of the MB was modified with epoxy groups so some biomolecules can be immobilized to the surface. According to the protocol, 200 µL of the 4.5 µm MBs was transferred from the storage vial to a 1.5 mL microcentrifuge tube, and 30 s vortex was applied to suspend beads uniformly in the solution. Then the MBs were separated from the storage solution by the magnet separation. After applying the magnet to the side of the tube to for 1 min, the supernatant was discarded from the tube. 1 mL of PB was added into the tube to wash the beads. After the washing step, the MBs were suspended in 200 µL PB and ready for the antibody coupling. The ratio between the antibody and 4.5 µm MBs was set to 50 µg antibody for 200 µL MBs solution according to the recommendation of the user manual. The concentration of the purchased anti-CRP antibody is 11.3 mg/mL, so the volume of the antibody needed for 200 µL of MBs is approximately 5 µL. The prepared 200 µL MBs was washed by PB again and suspended in 195 µL PB (200 µL minus 5 µL antibody). Then 5 µL antibody was added into the tube and incubated for 15 min with a sample mixer (15920D, HulaMixer, Invitrogen, Thermo Fisher Scientific, Burlington, ON, Canada) at room temperature. After the incubation, 4 µL BSA (50 mg/mL) was added into the tube to reach a concentration of 0.1% *w/v* BSA in the tube. The role of the BSA is to block the unbound sites on the surface of the MBs. After the addition of BSA, the mixture was incubated for 24 hours with the mixer. After the incubation, the MBs were washed by 200 µL PBS with 0.1% BSA and 2 mM sodium citrate solution twice and incubated for 5 min for each washing step. The MBs were then resuspended in 200 µL PBS with 0.1%

BSA and 2 mM sodium citrate solution and ready for the immunoprecipitation test. The conjugated MBs were stored between 2 to 8°C with the addition of 0.02% preservative sodium azide to extend the storage time. The concentration of the conjugated MBs was approximately 4×10^8 beads/mL.

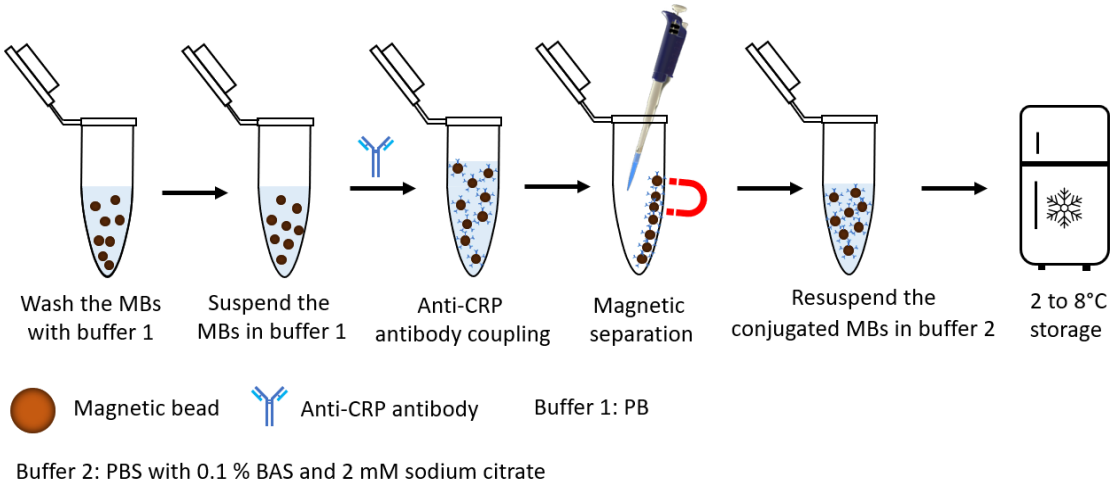

Figure 3-1: Anti-CRP antibody coupling procedure of the 4.5 μm MBs

3.1.2 Aggregates formation

Before the conduction of the immune reaction, the stored antibody conjugated MBs were washed with PBS once. Then the MBs were diluted by PBS to a certain concentration. To deagglomerate the MBs clusters caused by the storage, 10 s sonication was applied to suspend the MBs uniformly in the PBS. Different concentrations of CRP samples were prepared by the dilution of CRP (082, Sekisui Diagnostic, Burlington, MA, USA) with PBS. 10 μL of desired concentration of MBs and 10 μL CRP samples were added into a 0.6 mL microcentrifuge tube with 10 s vortex mixing. Then, the mixed samples were incubated for 5 min with a mixer at room temperature to form aggregates. After the short

time incubation, 10 μL of incubated mixture was used for each counting by the hemocytometer. The number of different sizes of aggregates including dimers, trimers, larger aggregates, and monomers were recorded. As shown in Figure 3-2 (b), a sample containing 30 mg/L CRP presented obvious agglutination compared to the negative sample in Figure 3-2 (a).

(a) 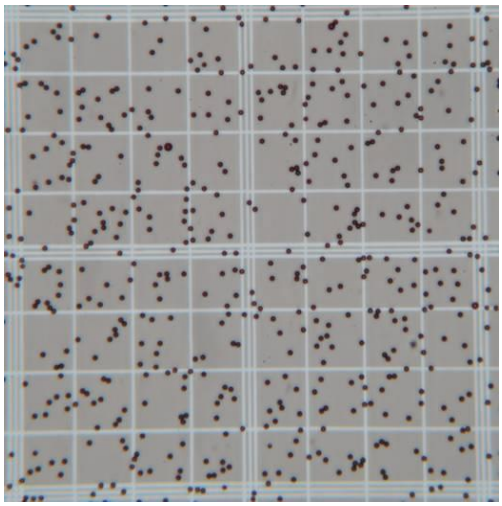 (b) 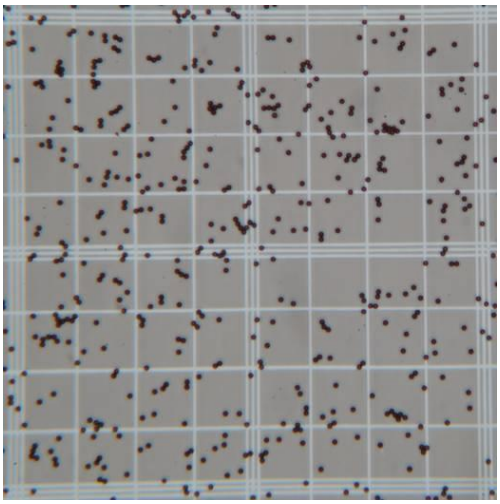

Figure 3-2: Microscopic pictures of 4.5 μm MBs assay mixture counted by the hemocytometer (10 × 40). (a) A negative sample (PBS); (b) 30 mg/L CRP sample.

3.1.3 Image J counting

To improve the counting efficiency, an image processing program named Image J (Wayne Rasband) was used to distinguish monomers from aggregates. The parameter of circularity ranging from 0.00 to 1.00 in Image J is used to filter particles based on their roundness. 0.00 denotes a straight line and 1.00 denotes a perfect circle. An example of a microscopic picture of 4.5 μm MBs was processed with Image J by adjusting the circularity to realize the counting of aggregates and monomers. As shown in Figure 3-3 (a), by setting the

circularity ranging from 0.8 to 1.00, the number of the monomers was counted, larger MBs aggregates (manually marked with red circle) were excluded. In contrast, the total number of monomers and aggregates were counted when the circularity is set from 0 to 1.00, which was shown in Figure 3-3 (b). The results turned out the Image J can be used to count monomers and aggregates in the assay mixture.

(a) 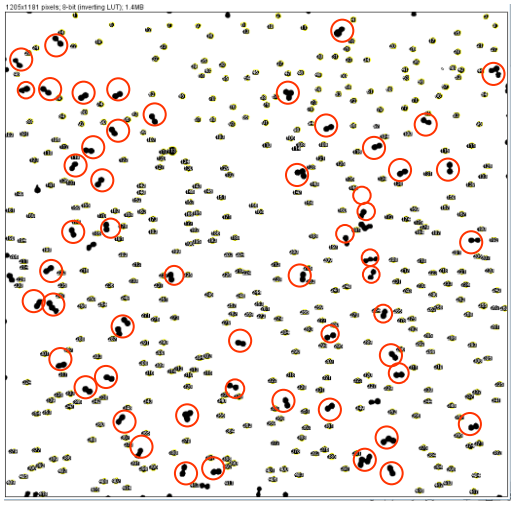 (b) 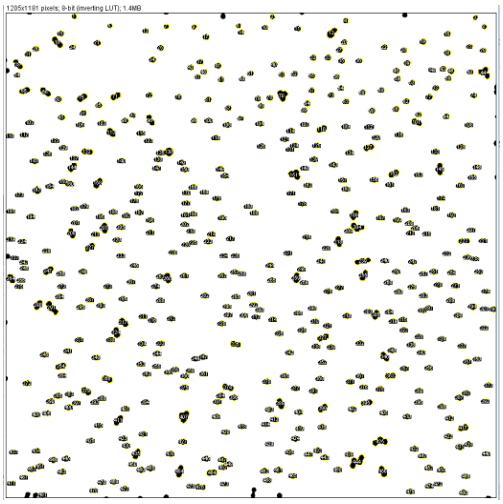

Figure 3-3: The screenshots of counting results by Image J with different range of circularity. Particles are marked with counted number. (a) 4.5 μm MBs microscopic picture was processed by Image J with a circularity ranging from 0.80 to 1.00 and aggregates are marked with red circle manually for a better comparison; (b) The same 4.5 μm MBs microscopic picture was processed by Image J with a circularity ranging from 0.00 to 1.00.

3.1.4 The optimization of the MBs size

To optimize the size of MBs for the agglutination immunoassay, 1 μm Dynabeads MyOne Tosylactivated (65502, Invitrogen, Thermo Fisher Scientific, Burlington, ON, Canada) and 2.8 μm Dynabeads M-270 Epoxy were also used for the agglutination immunoassay. The assay protocols for 1 μm and 2.8 μm MBs were identical to the procedures of 4.5 μm MBs

described above. The antibody coupling procedure for 1 µm MBs was performed according to the user manual provided by the manufacturer.

3.1.4.1 CRP detection by MAIA with 4.5 µm MBs

A series of different concentration of CRP samples ranging from 0 to 70 mg/L were prepared for the CRP detection by the microscopic agglutination immunoassay to find the detection range of this method. Figure 3-4 shows the preliminary result of this detection. The y-axis is the proportion of monomers in the assay mixture and the x-axis is the concentration of CRP. The proportion of monomers decreased due to the agglutination caused by the immune reaction. However, the number of monomers will not decrease endlessly. At the switch point of 30 mg/L in Figure 3-4, the proportion of monomers increased even though the CRP concentration was high. This phenomenon can be explained by the Hook effect. It is a common immunological phenomenon. The excessive CRP will impede the formation of aggregates.

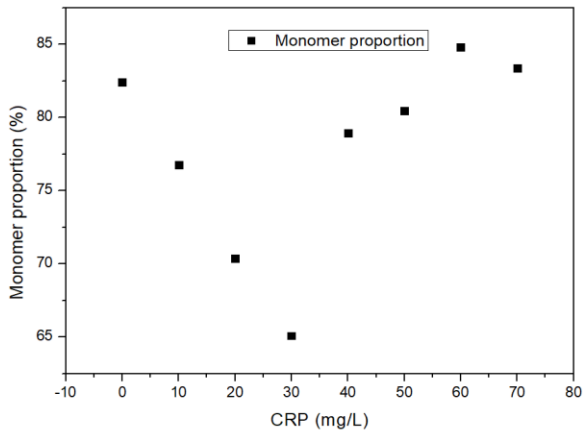

Figure 3-4: The measured relationship between the proportion of monomers and the concentration of CRP (4.5 µm MBs).

As shown in Figure 3-5, the excessive antigens will result in no immunoprecipitation in the solution, and this phenomenon is known as the postzone effect. If the absence of immunoprecipitation is caused by the excess of antibody, it is called the prozone effect. The appearance of immunoprecipitation occurs in the solution containing optimal ratio between antibody and antigen. Hence, the agglutination test should locate in the equivalence zone to avoid false-negative results.

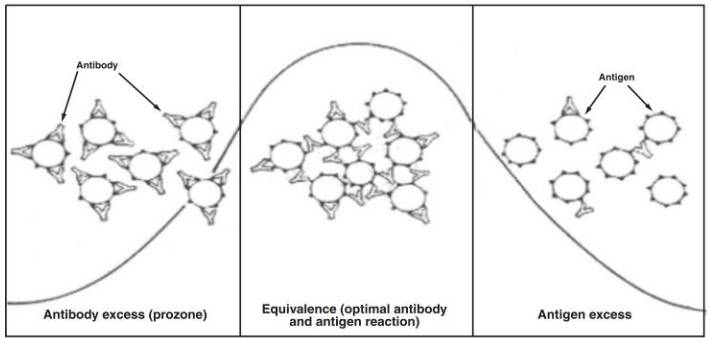

Figure 3-5: Precipitation curve of the immunoreaction. A series of different levels of antigen ranging from low concentration to high concentration were added into a fixed antibody solution respectively [121] (reproduce with permission).

Figure 3-6 shows the CRP detection result by the microscopic agglutination immunoassay with 4.5 μm MBs. The y-axis is the proportion of monomers in the assay mixture. The x-axis is the concentration of CRP. The proportion of monomers decreased with the increase of CRP concentration in the sample. A linear correlation was found for CRP detection by the microscopic agglutination immunoassay with 4.5 μm MBs. The detection range was up to 30 mg/L.

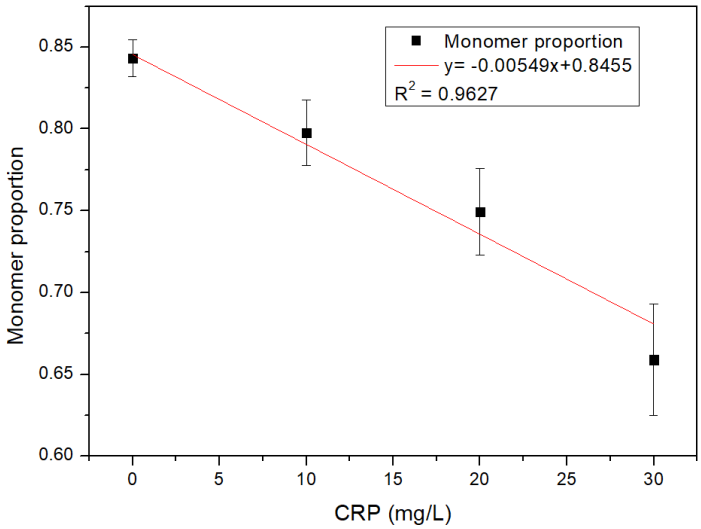

Figure 3-6: The measured relationship between the proportion of monomers and the CRP concentration (4.5 µm MBs). Each symbol is the mean value obtained from four duplicated samples. Error bars are the standard deviation (SD) of the four duplicated measurements.

3.1.4.2 CRP detection by the MAIA with 2.8 µm MBs

(a) 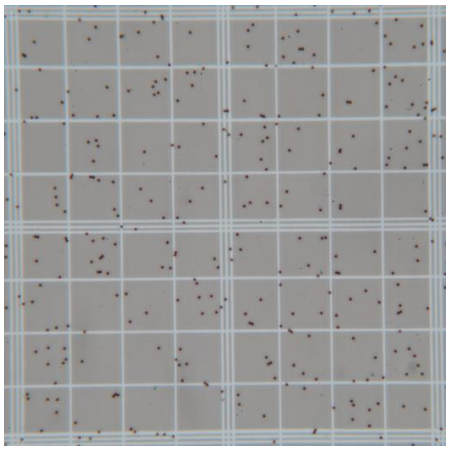 (b) 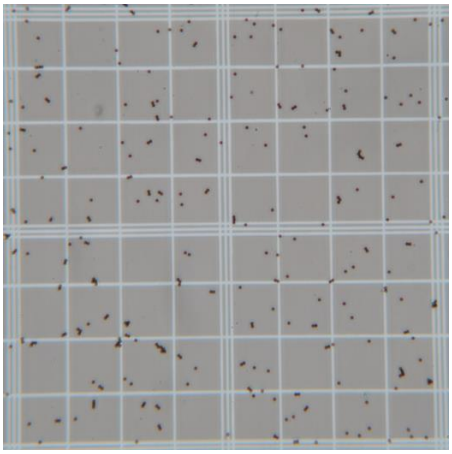

Figure 3-7: Microscopic pictures of 2.8 µm MBs assay mixture counted by the hemocytometer (10 × 40) , (a) A negative sample (PBS), (b) 15 mg/L CRP sample.

A series of different concentration of CRP samples were prepared for the agglutination immunoassay. The procedure for the immunoassay is identical to the 4.5 µm MBs which

has been described in section 3.1.2 except the dilution index for the conjugated MBs. As shown in Figure 3-7 (b), an obvious agglutination phenomenon appeared when a 15 mg/L CRP sample was added to the conjugated MBs. However, the number of aggregates in the negative sample of PBS in Figure 3-7 (a) was quite small.

Figure 3-8 shows the detection results of CRP by the microscopic agglutination immunoassay with 2.8 μm MBs.

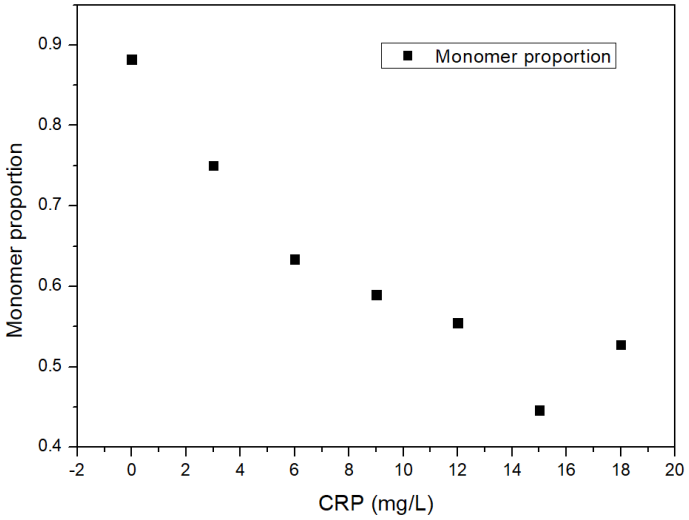

Figure 3-8: The measured relationship between the proportion of monomers and the concentration of CRP (2.8 μm MBs).

The y-axis is the proportion of monomers in the assay mixture. The x-axis is the concentration of CRP. The proportion of monomers decreased as the concentration of CRP went up. The switch point for CRP detection by 2.8 μm MBs appeared around 15 mg/L. Compared with switch point of CRP detection by 4.5 μm MBs which was 30 mg/L in Figure 3-4, the switch point for 2.8 μm MBs was smaller. Although the 2.8 μm MBs have relatively larger specific surface area, the 4.5 μm MBs have higher possibility of aggregate

formation. By increasing the concentration of the conjugated MBs, the switch point will shift to higher CRP levels. However, the CRP levels in most health people are less than 10 mg/L, the assay range for CRP detected by the MAIA meets the requirement of routine CRP detection. Furthermore, increasing the concentration of conjugated MBs will increase testing cost.

Figure 3-9 shows the detection results of CRP by the MAIA with 2.8 µm MBs. Like the results of 4.5 µm MBs in Figure 3-6, the higher concentration of CRP resulted in lower proportion of monomers in the assay mixture.

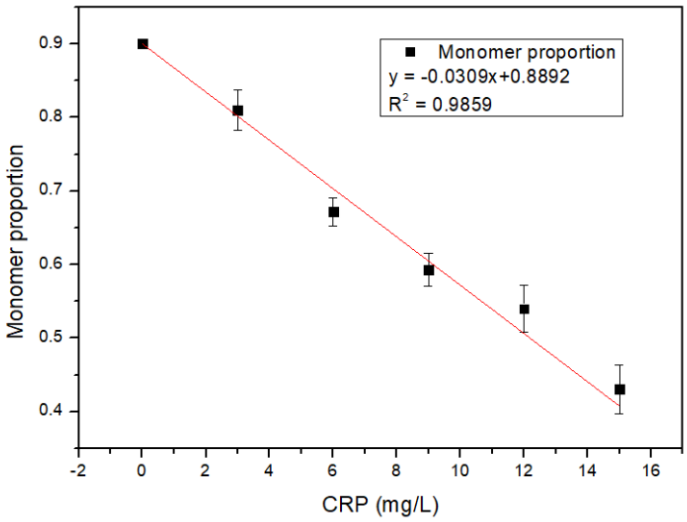

Figure 3-9: The measured relationship between the proportion of monomers and the CRP concentration (2.8 µm MBs). Each symbol is the mean value obtained from four duplicated samples. Error bars are the SD of the three duplicated measurements.

3.1.4.3 CRP detection by the MAIA with 1 µm MBs

1 µm Dynabeads MyOne Tosylactivated MBs were also used to verify the CRP detection. However, the self-agglutination of the MBs after the antibody coupling procedure was

obvious (Figure 3-10). In addition, the size of 1 μm MBs may not be big enough for the microflow cytometry to differentiate between monomers and aggregates. In conclusion, the 1 μm MBs were not suitable for this study.

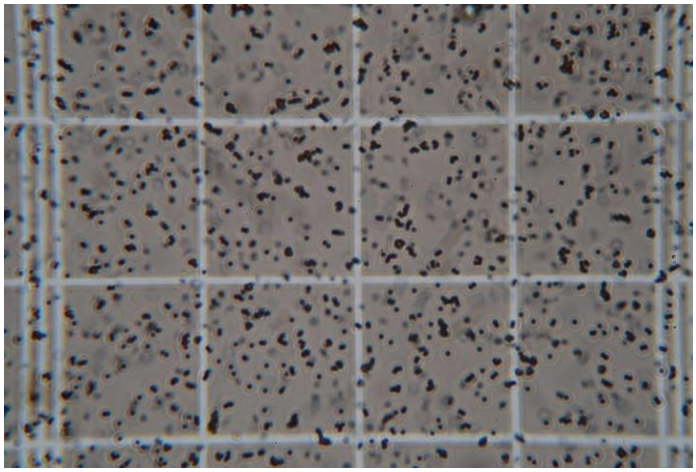

Figure 3-10: Microscopic picture of 1 μm conjugated MBs (10 × 40).

3.1.5 The optimization of the ratio between anti-CRP antibodies and MBs

To optimize the ratio between anti-CRP antibodies and the MBs, three different volume of anti-CRP antibodies, 5 μL, 10 μL and 15 μL were added to 200 μL 4.5 μm MBs. Other incubation conditions remained unchanged.

Figure 3-11 shows microscopic pictures of negative samples of PBS counted by the hemocytometer with different volume of anti-CRP antibodies added to 4.5 μm MBs. When 15 μL anti-CRP antibodies was added, the effect of nonspecific agglutination caused by the conjugated MBs themselves was obvious (Figure 3-11 (c)), which will decrease the sensitivity for CRP detection by reducing the possibility of aggregate formation caused by

CRP. The addition of 10 µL anti-CRP antibodies shows the comparable no-specific agglutination to the result of the addition of 5 µL anti-CRP antibodies (Figure 3-11 (a) and (b)). Therefore, 10 µL anti-CRP antibodies was used for antibody coupling to 200 µL of 4.5 µm MBs. Similar experiments were performed to find the optimal ratio between the anti-CRP antibodies and 2.8 µm MBs. The result turned out that 10 µL anti-CRP antibodies was suitable for antibody coupling to 5 mg 2.8 µm MBs.

(a) 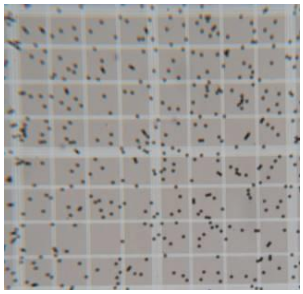 (b) 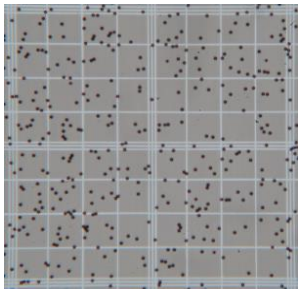 (c) 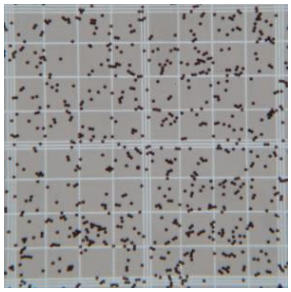

Figure 3-11: Microscopic photos of negative samples (PBS) with different volume of anti-CRP antibodies used for antibody coupling to 200 µL 4.5 µm MBs (10 × 40), (a) the addition of 5 µL anti-CRP antibodies; (b) solution the addition of 10 µL anti-CRP antibodies; (c) the addition of 15 µL anti-CRP antibodies.

3.2 Flow cytometry-based agglutination immunoassay (FCAIA)

The commercial flow cytometry (BD LSRFortessa, Bergen County, NJ, USA) was used to verify the FCAIA format. 2.8 µm and 4.5 µm anti-CRP antibody conjugated MBs were used for the immunoassay. The protocols for the immune reaction were the same to the assay described in the section of 3.1.2. After the preparation of the assay mixture, the mixture was diluted 25-fold by adding 230 µL PBS before the measurement by flow cytometry. The sample flow rate for the flow cytometry was set to 10 µL/min for all

measurements. 10000 events were collected for each detection.

3.2.1 CRP detection by the FCAIA with 4.5 µm MBs

Figure 3-12 shows the aggregates distribution of a negative sample of PBS and a sample containing 2 mg/L CRP measured by the flow cytometry.

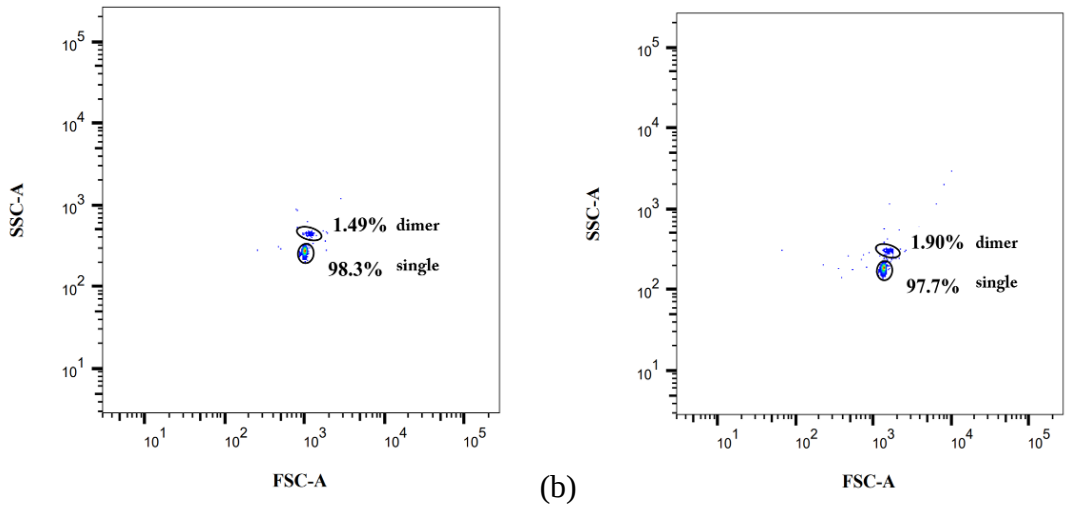

Figure 3-12: Aggregates distribution of the 4.5 µm MBs assay mixture. (a) A negative sample; (b) 2 mg/L CRP sample.

The y-axis is the side-scattered area (SSC-A), and the x-axis is the forward scattered area (FSC-A). The population with relatively lower intensity of SSC-A and FSC-A was considered as the distribution of monomers. The other population with relatively higher intensity of SSC-A and FSC-A was considered as the distribution of dimers. The proportion of monomers in assay mixture for other samples containing 4 mg/L, 6 mg/L, 8 mg/L CRP were 97.2%, 97.8%, and 98.2%, respectively. The proportion of monomers in CRP samples was close to that of the negative sample. Almost no immune aggregates were detected by the flow cytometry. One possible reason for this phenomenon was that the aggregates were

separated by the flow in the channel of the flow cytometry due to relatively higher mass of 4.5 µm MB. The binding between the MBs caused by the immune reaction was not strong enough to keep the state of agglutination even though the sample flow rate was set to the minimum value, which was 10 µL/min.

3.2.2 CRP detection by the FCAIA with 2.8 µm MBs

Since no correlation between the proportion of monomers and the concentration of CRP was found for CRP detected by FCAIA with 4.5 µm MBs, smaller MBs with a diameter of 2.8 µm were used to test the feasibility of the FCAIA for CRP detection. The procedure for the 2.8 µm MBs was identical to the procedure of 4.5µm MBs. Figure 3-13 shows the aggregates distribution of a negative sample of PBS and a sample containing 2 mg/L CRP.

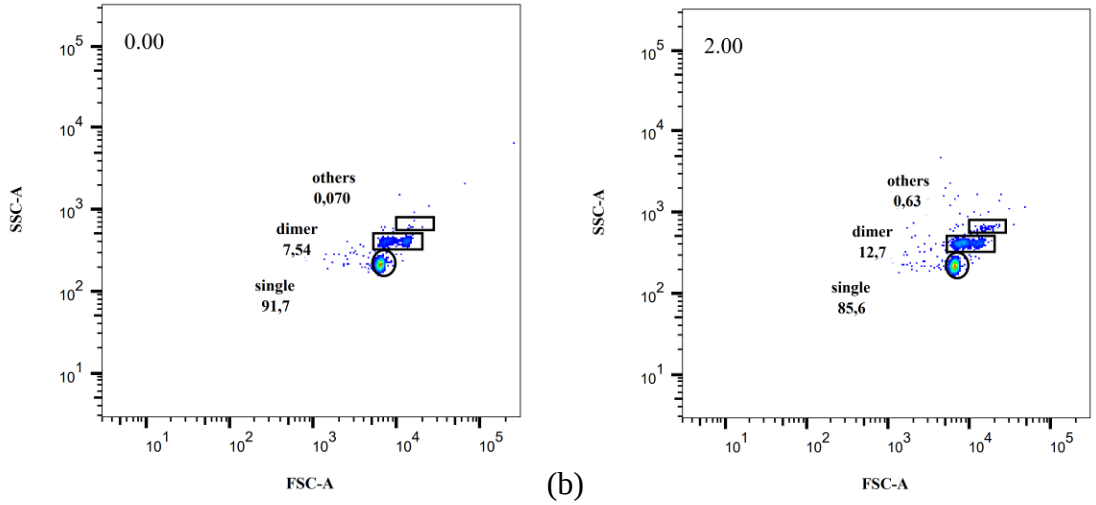

(a) (b)

Figure 3-13: Aggregates distribution of the 2.8 µm MBs assay mixture. (a) a negative sample; (b) a sample containing 2 mg/L CRP

Figure 3-13 (a) shows the aggregates distribution of a negative sample and more than 90% of aggregates are monomers. Figure 3-13 (b) shows the aggregates distribution of a sample

containing 2 mg/L CRP. The proportion of monomers in Figure 3-13 (b) was 85.6%. It turned out that more aggregates were produced in the presence of CRP and the flow cytometry can differentiate between monomers and aggregates.

A relationship between the proportion of monomers and the concentration of CRP was found for 2.8 µm MBs. The y-axis is the proportion of monomers and the x-axis is the concentration of CRP in the sample. A linear curve with a correlation coefficient of 0.9954 was established. It turned out that the proposed format was feasible for CRP detected by flow cytometry and an on-site CRP detection by the MCAIA could be possible.

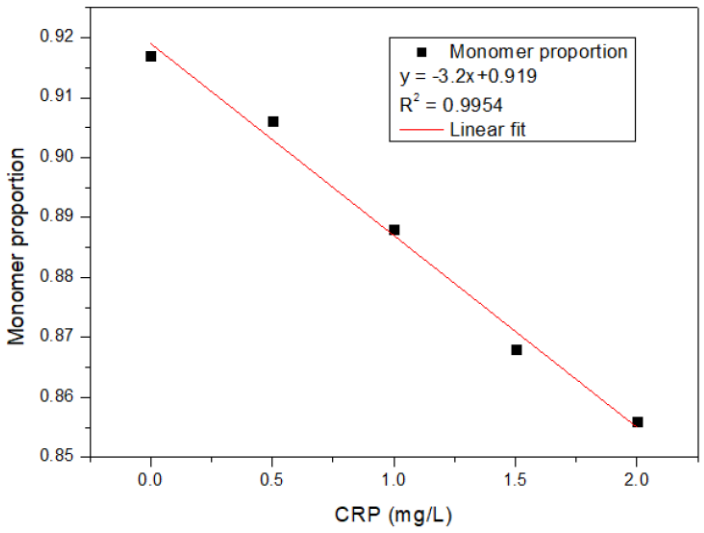

Figure 3-14: The correlation between the proportion of monomers and the concentration of CRP, samples were measured by the FCAIA with 2.8 µm MBs.

3.3 The verification of the MCAIA

After the format verification by the FCAIA, the designed microflow cytometry was used to test the MCAIA format. The preparation of assay mixture for CRP detection by the

MCAIA was the same as the MAIA. After the incubation of CRP, the assay mixture was introduced to the pipeline which was connected to the sample syringe. The sample and sheath flow rate of the MCAIA were set to 200 µL/h and 800 µL/h, respectively. The PMT voltage was tuned to -500 V and the gain of the I-V amplifier was set to 1×10^4. The sampling rate of the DAQ was set to 250 kHz. 2 min data was logged by the custom program for further analysis. Figure 3-15 presents a summary of the protocols for the MAIA, the FCAIA, and the MCAIA. The protocols for the preparation of the assay mixture for these three assays are the same except that the assay mixture for the flow cytometry immunoassay need to be diluted 25-fold by PBS to provide enough volume for one analytic run.

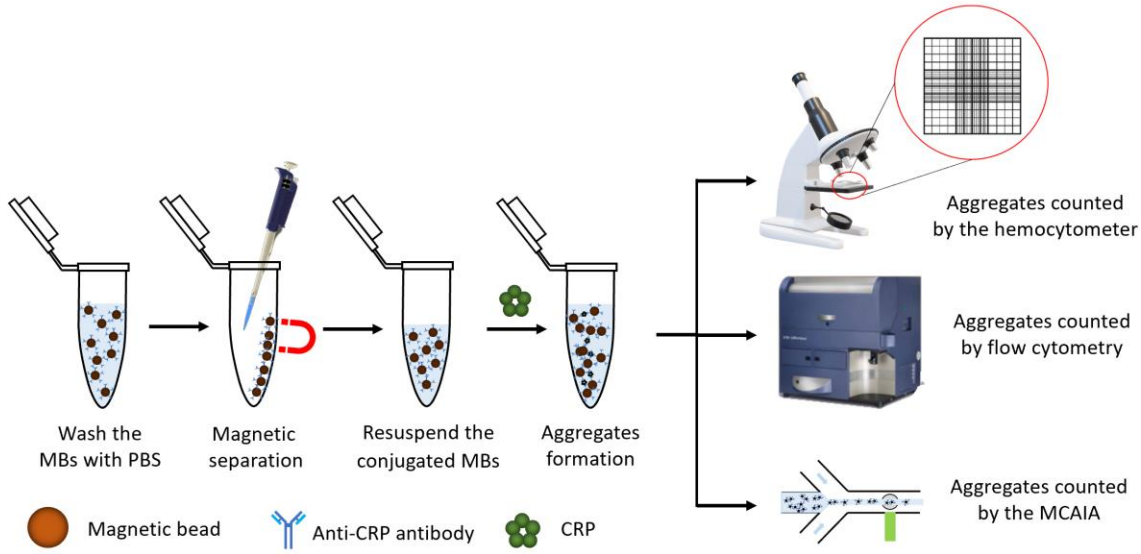

Figure 3-15: Protocols for the MAIA, the FCAIA, and the MCAIA.

3.3.1 Data analysis by LabVIEW

Figure 3-16 shows the plot of one second SSC signals obtained from a negative sample of

PBS detected by the MCAIA using 2.8 μm MBs. The y-axis is the amplitude of the signal in the unit of mV, and the x-axis is a segment of one second out of two min recorded data. SSC light was produced when the particle passed through interrogation region. The SSC light was detected and amplified by the PMT. The current signal from the PMT was further transferred and amplified by the I-V amplifier, which was finally shown in Figure 3-16.

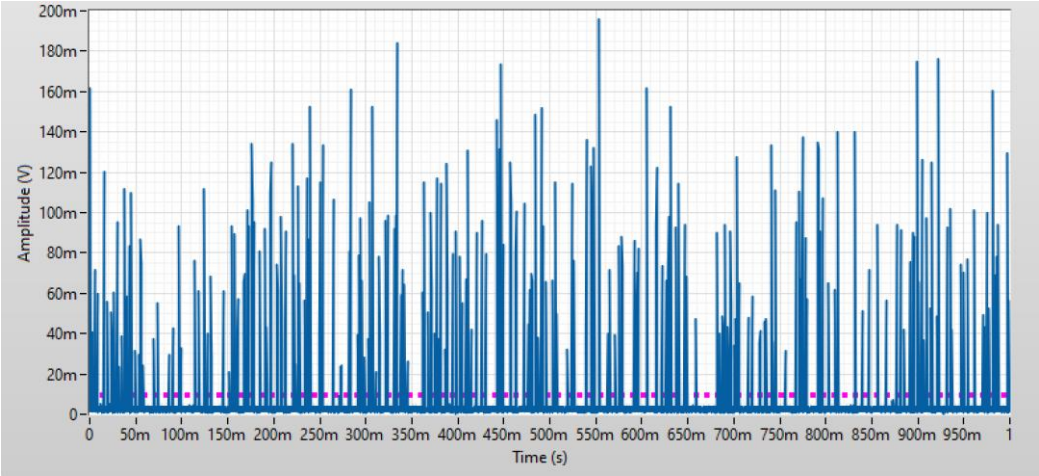

Figure 3-16: One second SSC signals obtained from a negative sample of 2.8 μm MBs.

The red dashed line was the value of four times SD of the background noise, which was used to distinguish SSC signals from the background noise. However, the intensities of the SSC signals from the negative sample varied a lot even though nearly 90% of particles in the negative sample were monomers. One possible reason for the high SD of the signal intensities could be the uneven distribution of the incident laser beam. The aggregates passing through the center of the beam tended to have relatively stronger SSC light than those passing through near the edge of the beam. Internal reflections coming from adjacent particles and the liquid/PDMS interface could also contribute to the high SD of the signal

intensities. Moreover, the uneven surface and the irregular shape of the MBs may also affect the intensities of the SSC light.

3.3.2 Data analyzed using the amplitude

Figure 3-17 shows the histogram of the amplitude distribution of 1×10^4 SSC signals obtained from measurements of a negative sample of PBS and a sample contain 1 mg/L CRP. The y-axis is the number of signals and the x-axis is the intensity of the signal. The black curve describes the amplitude distribution of the recorded signals and the red curve is the Gaussian fit to the black curve. The green curve is the difference between the black curve and the red curve. The number of signals in Figure 3-17 (a) equals to the number of signals in Figure 3-17 (b), so the areas under the black curves of these two samples are the same. In Figure 3-17 (a), which is the distribution of signals obtained from a negative sample, the red curve fitted well to the black curve of the real signals. The coefficient of determination (R^2) of the Gaussian fit was 0.9507. The signal intensities of monomers were lower, so the narrow and sharp curve of the Gaussian fit was assumed to be the distributions of monomers. As shown in Figure 3-17 (a), there is a small portion of signals distributed at higher value of amplitude. The portion could be the distribution of nonspecific aggregates in the negative sample. This phenomenon is a common issue for the particle counting immunoassay, where electrostatic repulsion is not strong enough to separate the aggregates even though a short time sonication had been applied. The area under the red curve is approximately 92.47% of the area under the black curve, implying that nearly 92.47% of particles in the assay mixture of the negative sample were monomers. This result agreed

with the proportion of monomers of the negative sample counted by the commercial flow cytometry, which had 91.7% monomers. The y-coordinate value of the vertex for the negative sample was 920, and the x-coordinate value of the vertex is 12.16 mV. Figure 3-17 (b) shows the distribution of SSC signals obtaining from a sample containing 1 mg/L CRP. The coefficient of determination (R^2) of the Gaussian fit was 0.9507.

(a) 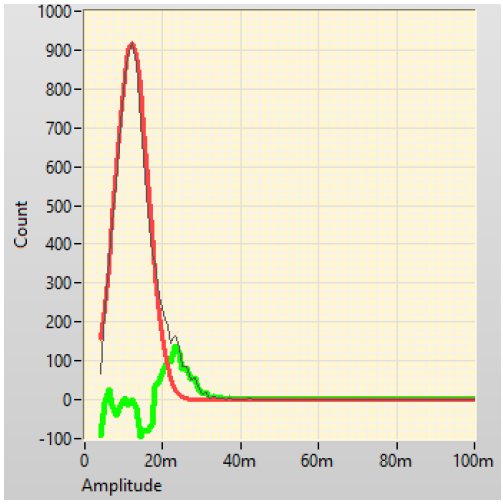

(b) 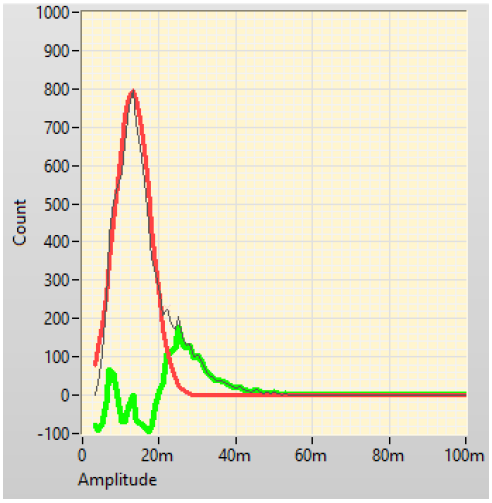

Figure 3-17: Histogram of the amplitude distribution of recorded 1×10^4 SSC signals with Gaussian fit. (a) a negative sample; (b) a sample containing 1 mg/L CRP.

Compared to the intensity distribution of the negative sample, the peak value of the black curve in Figure 3-17 (b) decreased to 787, and the number of the signals with higher intensities increased. The green curve had a peak value around 200, which was much higher than that in Figure 3-17 (a) (around 150). The width of the green curve above the x-axis in Figure 3-17 (b) was wider than that in Figure 3-17 (a), which was the result of the negative sample. This is due to the formation of MBs aggregates caused by the addition of CRP. The area under the red curve was about 83.74% of the area under the black curve, suggesting

that 83.74% of particles were monomers in the assay mixture. The assay mixture resulting from 1 mg/L CRP sample counted by the commercial flow cytometry shows 88.6% of monomers, suggesting that the MCAIA has a higher sensitivity for CRP detection than the FCAIA.

A series of CRP samples including negative sample, 0.5 mg/L, 1 mg/L, 1.5 mg/L, 2 mg/L, and 2.5 mg/L were tested by the MCAIA and data were analyzed using the amplitude with Gaussian fit. Figure 3-18 shows the preliminary result of the testing.

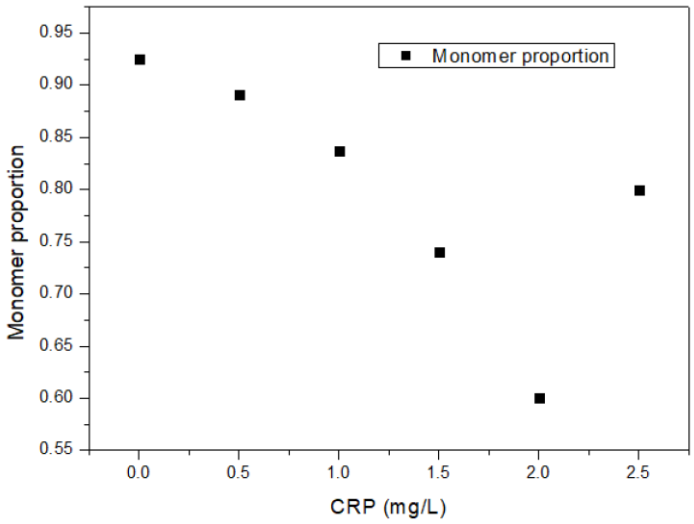

Figure 3-18: The relationship between the proportion of monomers and the concentration of CRP measured by the MCAIA with 2.8 μm MBs.

The y-axis is the percentage of the area under the red curve to the area under the black curve, which can be regard as the proportion of the monomers in the assay mixtures. The x-axis is the concentration of CRP. The switch off point caused by Hook effect appeared around 2 mg/L, which was close to the value in the FCAIA. The proportion of monomers decreased by the concentration of CRP until the concentration of CRP reached its switch

off value.

3.3.3 Data analyzed using the transit time

Although the data for the MCAIA can be analyzed using amplitude, the stability of the profile of the incident laser beam in the microchannel is a challenge for obtaining repeatable results. For example, if the optical axis of the laser beam was slightly off the centre of the microchannel due to the installation of the sample syringe, the amplitude distribution of the recorded SSC light signals were different when duplicated samples were measured. Compared to the intensities of the signals from monomers, no obvious regular increase was observed for aggregates. The transit time information was extracted from the recorded signals to solve this issue.

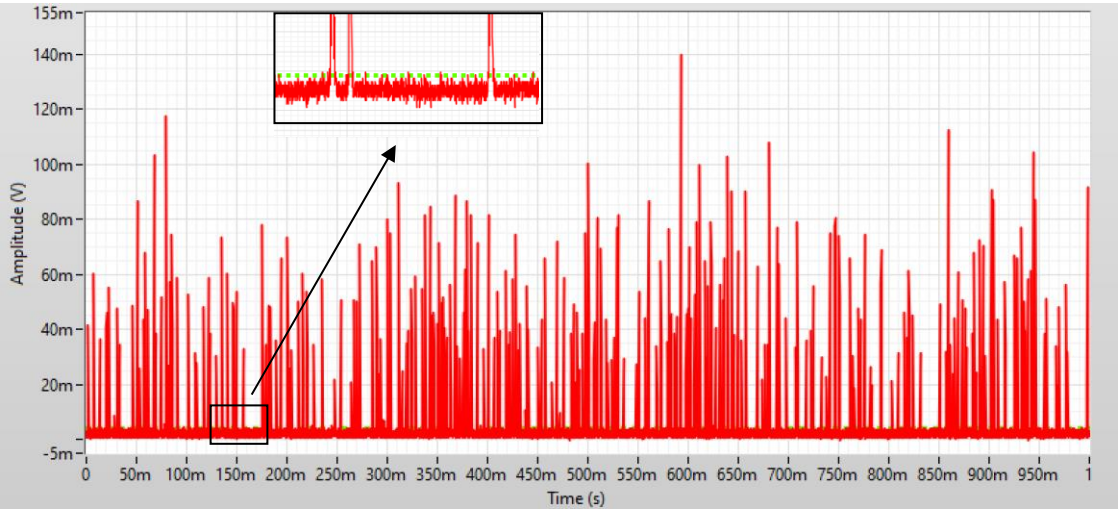

Figure 3-19: One second data of SSC signals obtained from a 0.75 mg/L CRP sample with 2.8 μm MBs.

Figure 3-19 shows one second raw data obtained from a 0.75 mg/L CRP sample. The y-axis is the amplitude of signals, and the x-axis is the time. The pulses colored with red line

are the recorded SSC signals when the assay mixture passed through the interrogation region. The green dashed line is the SD of the background noise which is used to differentiate SSC light signals from background noise.

Figure 3-20 shows the definition of the transit time. The y-axis is the amplitude of the signal, and x-axis is the time in milliseconds. The red line is a SSC light signal which was produced when a particle passed through the interrogation region. The green dashed line is the SD of the background noise, which is used to differentiate signals from the background noise. The interval between the intercepts of the signal and the green dashed line is defined as the transit time. It is the time that a particles takes to flow through the interrogation region [122]. Theoretically, the larger aggregates tend to have longer transit time. Therefore, the transit time could be used to differentiate between monomers and aggregates.

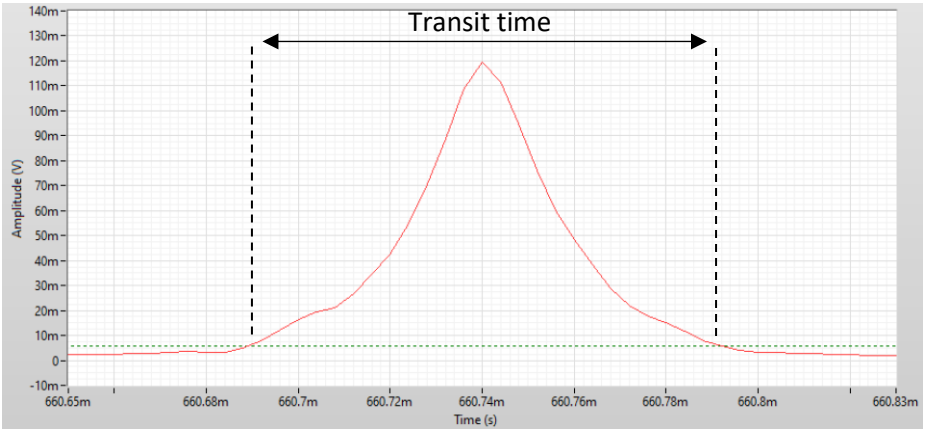

Figure 3-20: Detail view of the a SSC light signal with the definition of the transit time [122].

3.3.3.1 Calculation of the transit time

The time it takes for a particle to flow through the interrogation region is defined as the

transit time. The transit time of a monomer could be calculated by the Eq.3.1. In the Eq.3.1, τ is the transit time, L is the length of the interrogation region, d is the diameter of the MB, v is the velocity of particles in the sample stream, n is the number of the MBs comprising one aggregate, Q is the total flow rate of the stream in the microchannel, and S is the cross sectional area of the microchannel.

$$\tau = \frac{L + nd}{v} = \frac{L + nd}{Q/S} \tag{3.1}$$

For the MCAIA, sample flow rate and sheath flow rate are 200 µL/h and 800 µL/h, respectively, so the total flow rate is 1000 µL/h. The cross-sectional area S is 50 µm ×100 µm (height × width). The length of the interrogation region L is 10 µm. The stream in the microchannel is laminar flow. Particles in the centre of the microchannel have highest velocity of 111.1 mm/s, which is about double of the average flow velocity. For the monomer, the τ_{min}, which is the minimum time for it passing through the centre of the interrogation, is calculated to be 115.20 µs. For the dimer, n is 2, so the τ_{min} is calculated to be 140.40 µs. Based on the calculation, the dimers have about 25.2 µs longer transit time than the monomers.

3.3.3.2 Gaussian fit to the distribution of the transit time

Figure 3-21 shows transit time distribution of a negative sample of PBS and a sample containing 0.5 mg/L CRP. Equal number of 5 ×10^4 SSC light signals were collected from these two samples. The y-axis is the number of the signals located to the corresponding range of the transit time. The x-axis is the transit time in microsecond. In Figure 3-21 (a),

which is the transit time distribution of the negative sample, most recorded SSC light signals have the transit time about 100 μs. The distribution was a narrow and sharp peak. Figure 3-21 (b) shows the transit time distribution of a 0.5 mg/L CRP sample. Compared with the transit time distribution of the negative sample in Figure 3-21 (a), the count peak of the 0.5 mg/L CRP decreased from 1219 to 1005, and an obvious increase of signals with longer transit time appeared. This is attributed to the agglutination caused by the immune reaction between CRP and the conjugated MBs. The increase of the aggregates in the measured assay mixture will decrease the number of monomers and thus the peak of the distribution is shorter.

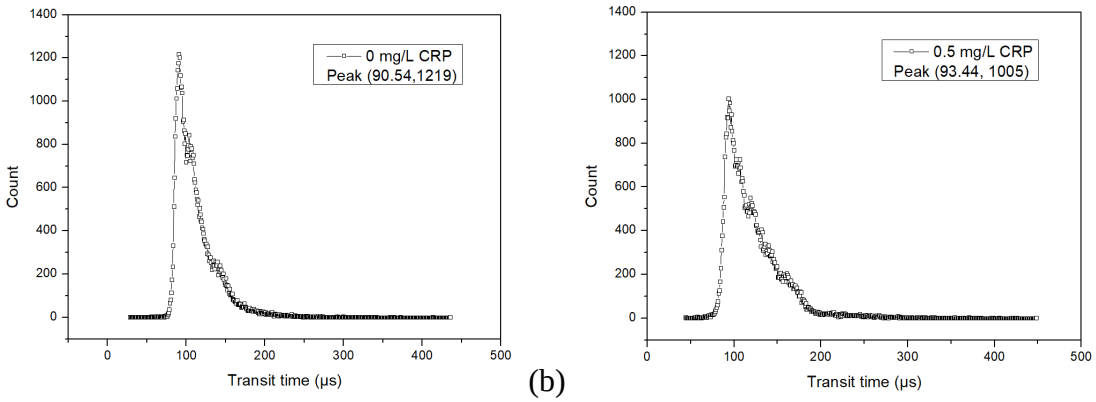

(a) (b)

Figure 3-21: The distribution of transit time. (a) a negative sample; (b) a sample containing 0.5 mg/L CRP. Each square symbol is the count of the corresponding transit time.

Figure 3-22 shows the transit time distribution of a 0.5 mg/L CRP sample with two-order Gaussian fit. The y-axis is the number of the SSC light signals, and x-axis is the transit time. Two-order Gaussian fit was used because according to the microscopic observation of the assay mixture obtained from the 0.5 mg/L CRP, the particles were mainly monomers and dimers. The peak 1 colored with green line is assumed as the distribution of monomers.

The peak value of the monomers is 95.77 μs. The peak 2 colored with blue line is considered as the distribution of dimers, which has a peak value of 122.30 μs. The difference between these two peaks value is 26.53 μs. Three duplicated 0.5 mg/L CRP samples were measured and analyzed by the two-order Gaussian fit. The difference between peak 1 and peak 2 is 25.00 ± 0.11 μs (mean ± SD).

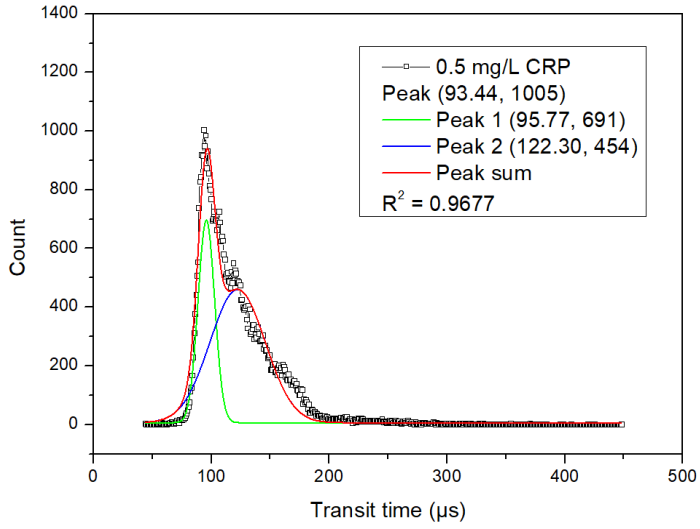

Figure 3-22: The transit time distribution of a 0.5 mg/L CRP with two-order Gaussian fit.

The theoretical calculation difference of the transit time between monomers and dimers is 25.02 μs, which is close to the mean value of the experimental results. It can be concluded that the MCAIA can discriminate monomers from aggregates. However, the theoretical transit time of the monomers and dimers are 115.20 μs and 140.40 μs, respectively. The transit time of the monomers and dimers calculated by the experiments are 95.77 μs and 122.30 μs, respectively. The experimental transit time is smaller than the theoretical one. Two possible reasons may contribute to the smaller experimental transit time. First, if the

cross-section area of the microchannel is smaller than the designed one (50 μm × 100 μm), the total flow rate will be higher than the calculated flow rate. Thus, the particles will travel faster with a shorter transit time. Second, if the length of the interrogation region is less than 10 μm, the transit time will be shorter too. For example, if the length of the interrogation region is 9 μm, the calculated transit time for the monomers which flow in the centre of the microchannel will be 106.20 μs. A deviation of one μm of the length of the interrogation region will cause 9 μs decrease of the transit time.

The microflow cytometry used in the MCAIA is based on a two-dimensional hydrodynamic focusing. The sample flow is confined by two sheath flows from its both sides and forced to flow in the centre of the microchannel. However, there are still some MBs in the sample stream that travel close to the edge of the microchannel. The transit time of those aggregates are relatively longer due to their lower velocity. It is hard to find a transit time to differentiate between the monomers and the aggregates because the monomers which flow through the interrogation region near the edge tend to have longer transit time. The monomer transit time distribution will extend towards the aggregates transit time distribution, making the Gaussian fit less accurate. To solve this issue, the average transit time is used to analyze the data. The average transit time is calculated by dividing the sum of all transit time signals with the number of the signals. Figure 3-23 shows the relationship between the average transit time and the concentration of CRP. The y-axis is the average transit time, and the x-axis is the concentration of CRP. The red line is a linear fit to the mean of three duplicated samples measured by the MCAIA. The average transit time

correlates well with the concentration of CRP and the R^2 is close to 1.

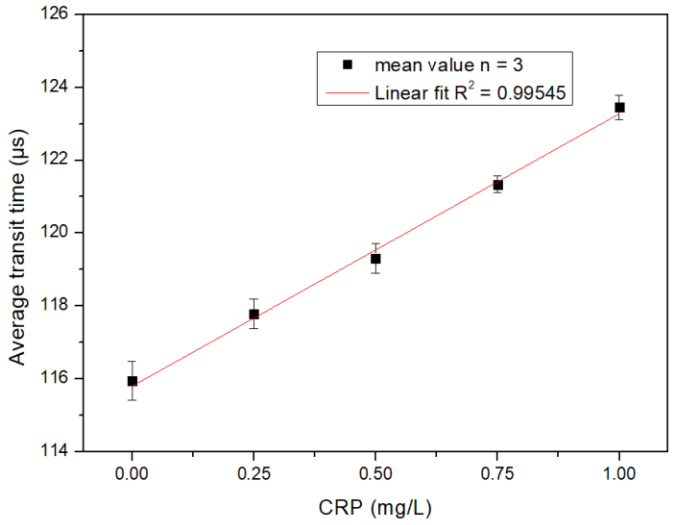

Figure 3-23: The correlation between the average transit time and the concentration of CRP. Error bar is the SD of three duplicated measurements. The square is the mean of the measurements.

The clinical requirement for detectable CRP is 0.5 mg/L. The LOD of CRP detection by the MCAIA is calculated by the following equation. *S* is the slope of the regression curve. σ is the residual SD of the regression curve.

$$LOD = \frac{3.3 \times \sigma}{S} \qquad 3.2$$

The calculated LOD for CRP detection by the MCAIA is 0.09 mg/L, which has met the requirement of the clinical CRP detection. The assay range of the MCAIA for CRP detection ranges is up to 1 mg/L. The concentration of CRP in health individuals is less than 10 mg/L. For the routine CRP detection by the MCAIA, a 10-fold dilution of the serum sample is needed to make sure the CRP concentration of the detected sample is within the detection range.

3.3.4 The Accuracy of the MCAIA

To evaluate the accuracy of CRP detection by the MCAIA. Two series of identical CRP samples were measured by both the turbidimetric immunoassay and the MCAIA, respectively. The procedure for the turbidimetric immunoassay was shown in Figure 3-24.

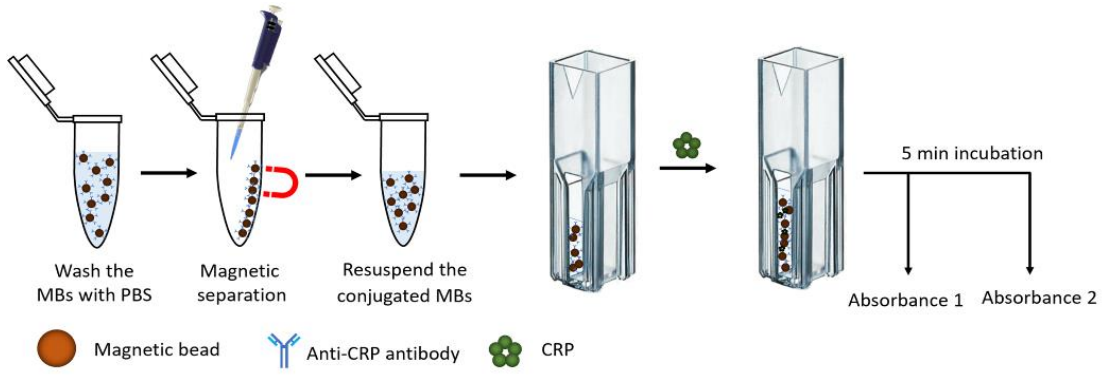

Figure 3-24: Procedure for the turbidimetric immunoassay for CRP detection. The difference of absorbance caused by 5 min incubation was measured.

After washing and dilution of the conjugated MBs, 10 µL MBs solution was transferred into the cuvette, and then 10 µL CRP sample was pipetted into the cuvette. Absorbance 1 was measured immediately after mixing the CRP sample with the conjugated MBs. After 5 min incubation, absorbance 2 was measured. A spectrophotometer (Beckman DU 800 Ultraviolet/Visible Spectrophotometer, Beckman Coulter Inc., Fullerton, CA, USA) was used to measure the absorbance. The working wavelength was determined by selecting the wavelength corresponding to the maximum absorption when the negative sample was measured with the spectrophotometer. 570 nm was determined as the working wavelength for CRP detection. The difference between absorbance 2 and absorbance 1 shows the extent of the agglutination.

Figure 3-25 shows the comparative performance testing of CRP detection using the turbidimetric assay and the MCAIA. 13 CRP samples with concentration ranging from 0.2 mg/L to 1 mg/L were measured by these two assays. The concentration of CRP correlates linearly to the absorbance difference. There was a significant correlation between the MCAIA and the turbidimetric assay and the correlation coefficient was 0.9792, implying that the MCAIA is accurate enough for the CRP measurement.

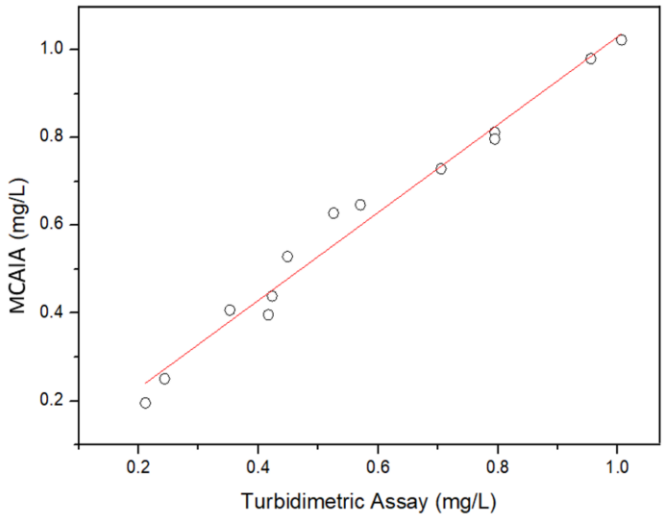

Figure 3-25: Scatter plot showing the correlation between the MCAIA and turbidimetric assay for CRP detection. Each circle represents a sample of CRP with certain concentration (n=13).

Compared to the traditional turbidimetric assay, the CRP detected by the MCAIA provided more information about the aggregates in the assay mixture. The amplitude and the transit time of signals obtaining from the aggregates were extracted by the MCAIA. The inherent drawback of turbidimetric assay is the matrix effect. By counting the aggregates one by one with the MCAIA, the matrix effect will not affect the performance of the MCAIA.

3.3.5 The interference of hemoglobin to CRP measurement by the MCAIA

The hemolyzed samples are the most common source of the interference for the clinical testing. Inaccurate measurements result from hemolytic samples are the main issues for the clinical analysis. The released hemoglobin from the hemolysis in the sample can produce unreliable results [123]. Figure 3-26 shows the interference of hemoglobin to the CRP detection using the MCAIA. Different concentration of CRP samples without and with 20 mg/L hemoglobin (H7379, Millipore-Sigma, Oakville, ON, Canada) were measured. As shown in Figure 3-26, the y-axis is average transit time, and the x-axis is the concentration of CRP.

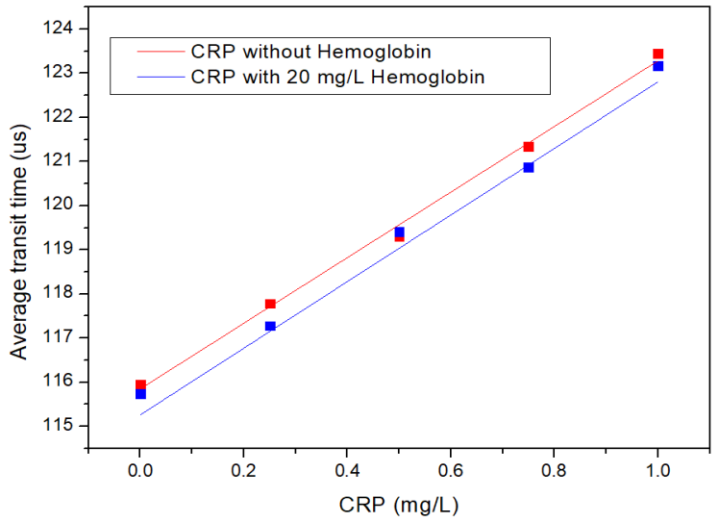

Figure 3-26: Scatter plot showing the relationship between average transit time and the concentration of CRP obtained from measurements of CRP samples with and without hemoglobin.

Each colored symbol is the mean value of the detection results obtained from three parallel measurements. Blue line and red line are the linear fit curves of the measurements from

pure CRP samples and CRP samples with 20 mg/L hemoglobin, respectively. To compare the slope and intercept of these two curves, SPSS software (IBM, Armonk, NY, USA) was used to analyze the data. The p-value for the intercepts and the slopes were 0.07 and 0.908, respectively, both of which are larger than 0.05. It is concluded that there is no remarkable difference between these two linear curves. Hemoglobin has little impact on the CRP detection when using the MCAIA.

Chapter 4 The MCAIA for SARS-CoV-2 Antibody Detection

The outbreak of SARS-CoV-2 has created a huge demand for the screen testing of the infections. Various serological assays for SARS-CoV-2 antibody detection have emerged to meet the urgent need. In this chapter, SARS-CoV-2 IgM and IgG detection will be used as models to illustrate the principle of the MCAIA for antibody detection.

4.1 The procedure for the SARS-CoV-2 antibody detection

The first step for the SARS-CoV-2 antibody detection by the MCAIA is the secondary antibody coupling. The secondary antibody conjugated MBs were prepared in a similar way to the anti-CRP antibody conjugated MBs. 2.8 μm MBs were used as the solid support for the secondary antibody. Figure 4-1 shows the procedure for secondary antibody coupling procedure for SARS-CoV-2 antibody detection. For SARS-CoV-2 IgM detection, goat anti-human IgM secondary antibodies (31136, Life Technologies, Thermo Fisher Scientific, Burlington, ON, Canada) were used for the coupling procedure. The concentration of the goat anti-human IgM secondary antibodies used in this research was 2.32 mg/L. According to the user manual provided by the manufacturer, 100 μg secondary antibodies are needed for 5 mg lyophilized MBs, so the volume of IgM secondary antibody needed for the antibody coupling procedure is 43 μL. The volume of PB needed to resuspend the MBs and the volume of 1 M ammonium sulfate equal to the volume of IgM secondary antibody. Except the volume and antibody used are different from the anti-CRP coupling procedure, other steps for the procedure are the same. For SARS-CoV-2 IgG detection, the secondary antibody used for the coupling were goat anti-rabbit IgG (H+L)

antibodies (31210, Life Technologies, Thermo Fisher Scientific, Burlington, ON, Canada), which had a concentration of 2.38 mg/L. Hence, the volume of the secondary IgG needed for the coupling procedure is 42 µL. The volume needed to resuspend the MBs using PB and the 1M ammonium sulfate are 42 µL. The secondary antibody conjugated MBs are stored between 4 to 8 ℃ and ready for future use. Sodium azide with a concentration of 0.02% (*w/v*) can be added to lengthen the shelf-life of the conjugated MBs.

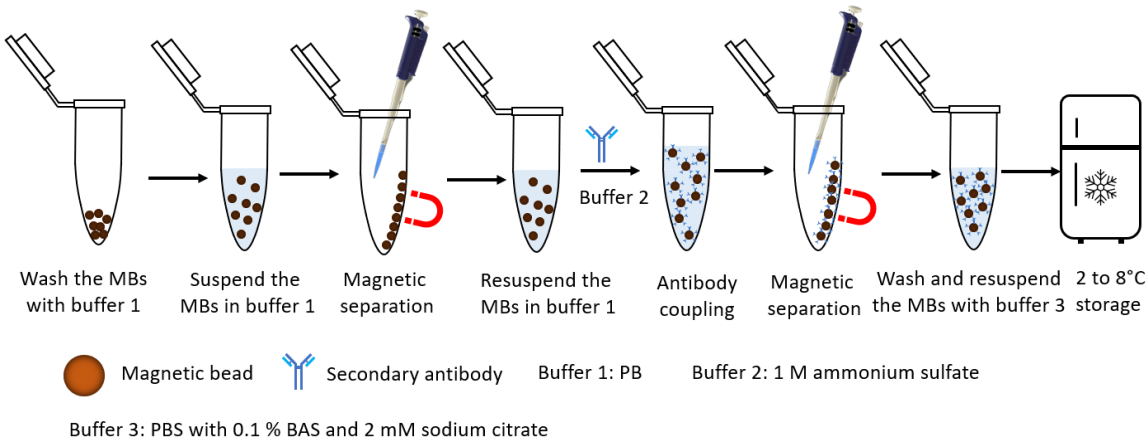

Figure 4-1: Schematic illustration of the procedure for secondary antibody detection.

Figure 4-2 shows the schematic illustration of the procedure for SARS-CoV-2 IgM and IgG detection by the MCAIA. The procedure for SARS-CoV-2 IgM and IgG detections are the same except that the secondary antibody used is different. The following procedure will describe how the SARS-CoV-2 IgM is measured by the MCAIA. The first step is washing the secondary IgM conjugated MBs. A certain volume of conjugated MBs was pipetted into a proper microcentrifuge tube and washed once with PBS and then diluted to a desired concentration. 10 µL of diluted conjugated MBs was transferred to a 0.6 mL

microcentrifuge tube and resuspended with thoroughly mixing. 10 µL of a sample containing SARS-CoV-2 RBD IgM humanized coronavirus monoclonal antibodies (MBS355900, MyBioSource, Inc., San Diego, CA, USA) was pipetted into the same vial and mixed with the MBs for 30 s. Then the vial was left to set for 25 min incubation. During this process, the immobilized secondary IgM will capture the IgM in the solution. After the primary antibody incubation, the solution was sonicated for 10 s to reduce the nonspecific agglutination and then 10 µL of 25 mg/L SARS-CoV-2 spike S1-His recombinant protein (40591-V08B1, Sino Biological, Beijing, China) was added into the vial with 30 s thoroughly mixing. The vial was left for 3 min incubation and the MBs were agglutinated through the immune reaction to form aggregates. The assay mixture was then introduced into the pipeline which was connected to the sample syringe. The flow rate of the sample and sheath for the MCAIA were set to 200 µL/h and 800 µL/h, respectively. The MBs aggregates were counted by the microflow cytometry and 2 min of raw data was recorded for analysis.

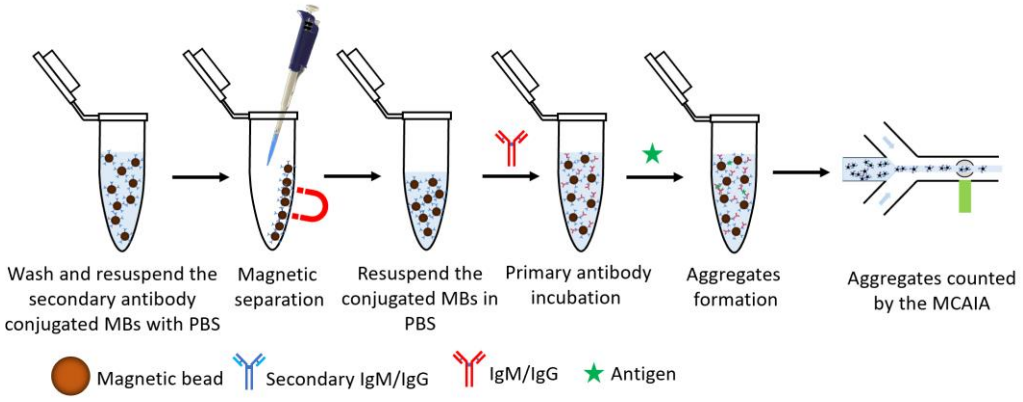

Figure 4-2: Schematic illustration of the SARS-CoV-2 IgM and IgG detection using the MCAIA

For SARS-CoV-2 IgG detection, goat anti-rabbit IgG (H+L) antibody and SARS-CoV-2 spike S1 antibody (40150-R007, Sino Biological, Inc., Beijing, China) were used as the secondary antibody and primary antibody, respectively. Other parameters were kept the same to SARS-CoV-2 IgM detection.

4.2 Data analysis by LabVIEW for SARS-CoV-2 IgM

Figure 4-3 shows one second data obtained from a sample containing 0.6 mg/L SARS-CoV-2 IgM. The y-axis is the amplitude of the signal, and x-axis is the time. Each pulse is related to one SSC light signal produced when a particle passed through the interrogation region. The green dashed line near the background noise is the threshold of the transit time, which is the SD of the background noise. The threshold is used to distinguish signals from background noise. The definition of the transit time has been described in section 3.3.3.

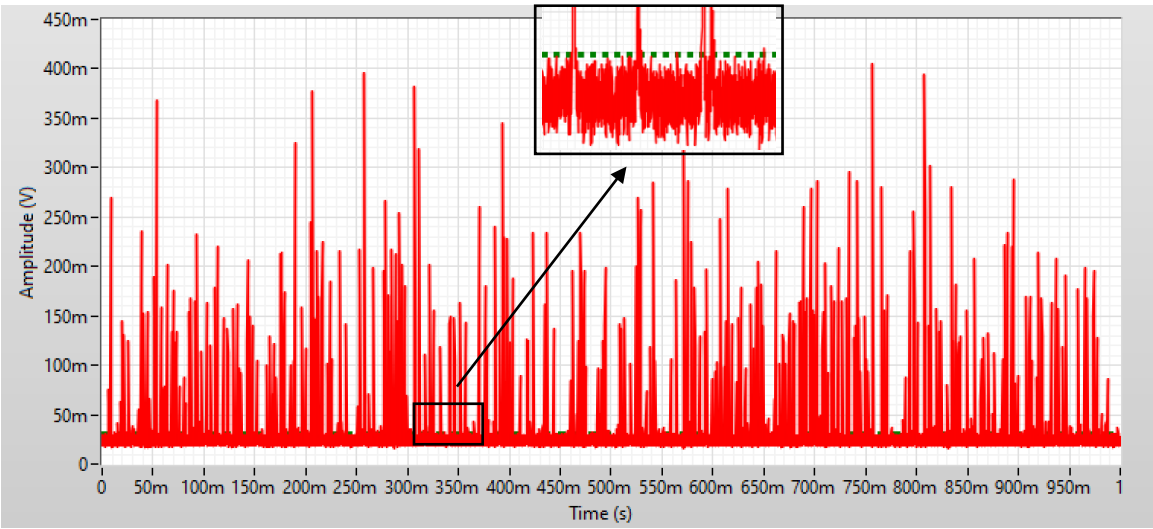

Figure 4-3: One second data recorded by the LabVIEW obtained from the detecion of a sample containing 0.6 mg/L SARS-CoV-2 IgM.

Figure 4-4 shows the transit time distribution of a negative sample of PBS and a sample containing 0.6 mg/L SARS-CoV-2 IgM. 2×10^4 signals were recorded for each measurement. The y-axis is the count of signals with the corresponding transit time, and the x-axis is the transit time. The transit time distribution of the negative sample shown in Figure 4-4 (a) has a peak count of 500, and the distribution is sharp and symmetrical. In Figure 4-4 (b), which is the transit time distribution of a 0.6 mg/L SARS-CoV-2 IgM, the distribution has a peak count of 340, and an obvious increase of the data points at longer transit time make the distribution shift towards higher transit time. This is attributed to the increase of aggregates in the presence of SARS-CoV-2 IgM in the sample.

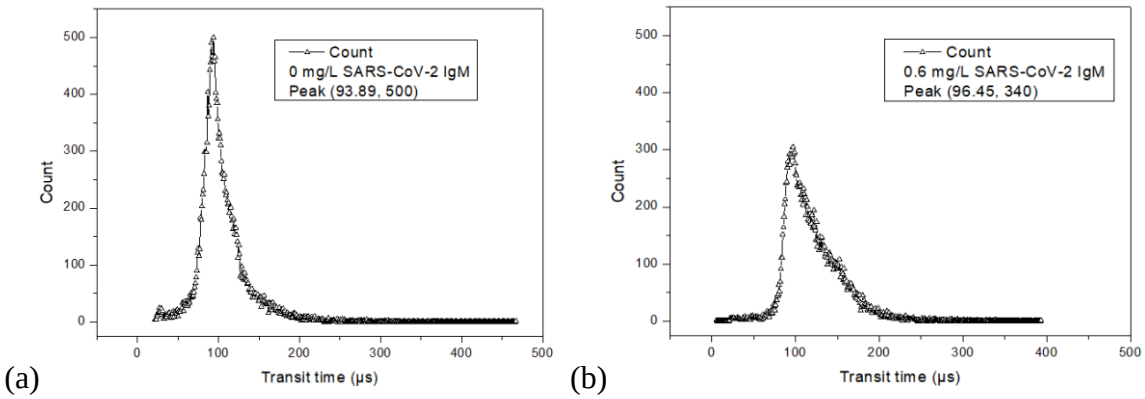

Figure 4-4: Transit time distribution. (a) a negative sample; (b) a sample containing 0.6 mg/L SARS-CoV-2 IgM.

Figure 4-5 shows the relationship between the average transit time and the concentration of SARS-CoV-2 IgM. The y-axis is the average transit time, and x-axis is the concentration of SARS-CoV-2 IgM. A series of different concentration of SARS-CoV IgM samples were detected by the MCAIA and the average transit time were calculated for each measurement. Black squares, red triangles, and blue circles in the Figure 4-5 represent the mean value of

the detection results obtained by using one day stored, eight days stored, and fifteen days stored goat anti-human secondary antibody conjugated MBs, respectively. The error bar is the SD of triplicate sample measurements. The solid line is the liner fit curve to the mean value of the detection results. As shown in Figure 4-5, there is a strong correlation between the average transit time of all SSC light signals and the concentration of SARS-CoV-2 IgM, and the correlation coefficient for day one detection, day eight detection, and day fifteen detection were all close to 0.99. The linear curve of day one detection was the steepest, and the slope decreased by the storage time of the conjugated MBs. This phenomenon suggested that the capturing capacity of the anti-human secondary conjugated MBs decreased as the storage time increased.

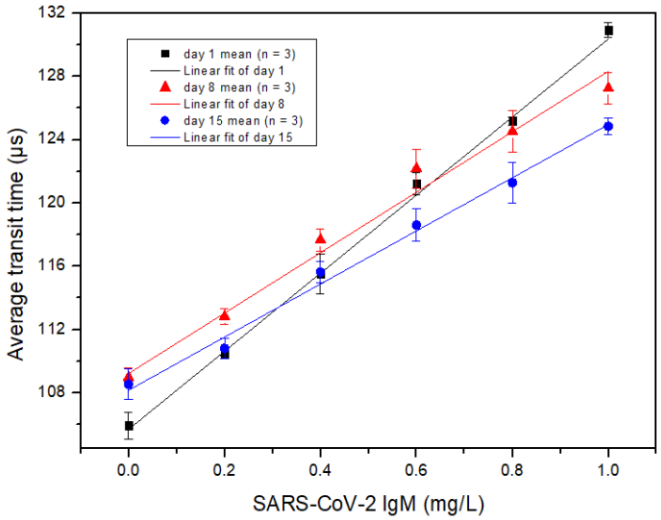

Figure 4-5: Scatter plot showing the correlation between the average transit time and the concentration of SARS-CoV-2 IgM.

The LOD of SARC-CoV-2 IgM measured by the MCAIA was calculated according the Eq.3.2 and it was 0.06 mg/L. A study using the in-house ELISA technique for quantitative

detection of SARS-CoV-2 IgM claimed a LOD of 0.28 mg/L [124], which is higher than that of the MCAIA for SARS-CoV-2 IgM detection. However, the assay range of the SARS-CoV-2 IgM detection using the MCAIA is still restricted by the Hook effect and is no higher than 1 mg/L. To avoid the false-negative, the samples to be detected should be kept in solution with concentration of SARS-CoV-2 IgM lower than 1 mg/L. This may be solved by dilution.

4.3 Data analysis by LabVIEW for SARS-CoV-2 IgG

Figure 4-6 shows one second raw data obtained from a measurement of 0.6 mg/L SARS-CoV-2 IgG using the MCAIA. The y-axis is the amplitude of the signal, and the x-axis is the concentration of SARS-CoV-2 IgG.

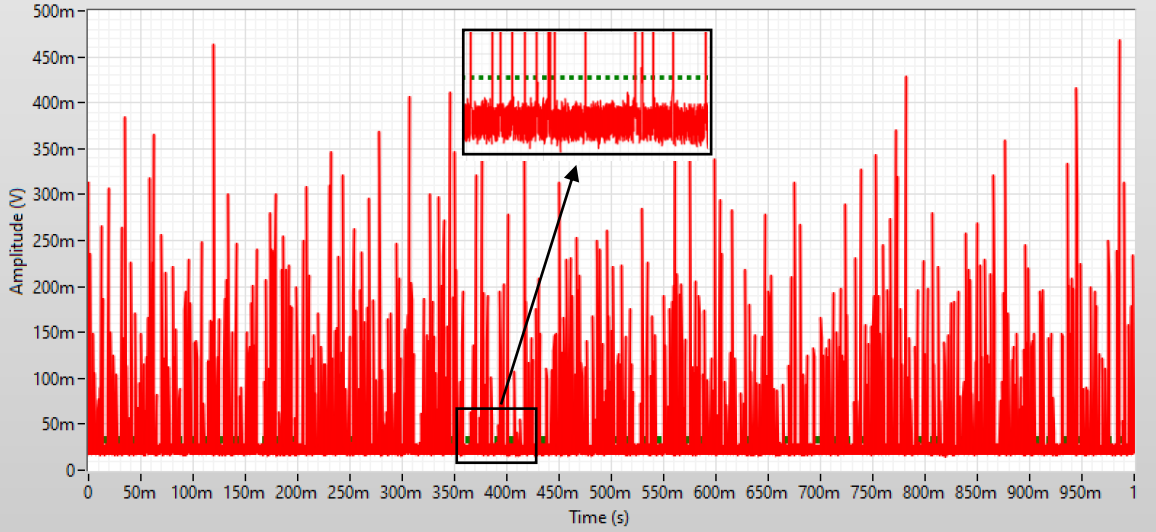

Figure 4-6: One second data recorded by the LabVIEW obtained from the detection of a sample containing 0.6 mg/L SARS-CoV-2 IgG.

Each peak colored with red represents one SSC light signal which was produced when a

particle passed through the interrogation region. The green dashed line near the background noise is the threshold of the transit time which is used to differentiate signals from background noise. The threshold is determined to be the SD of the background noise.

Figure 4-7 shows the distribution of transit time obtained from a negative sample of PBS and a sample containing 0.6 mg/L SARS-CoV-2 IgG. The y-axis is the count of signals with the corresponding transit time, and the x-axis is the transit time. Each circle represents the number of SSC light signals with corresponding transit time interval. 2×10^4 SSC light signals were recorded for each sample. Figure 4-7 (a) shows the distribution of transit time of the negative sample. The peak count of the distribution was 540 and the distribution had sharp peak and tended to be symmetrical. The distribution of transit time of 0.6 mg/L SARS-CoV-2 IgG sample was shown in Figure 4-7 (b). The peak count of the distribution was 441, which was about 100 less than the negative sample. The could be explained by the decrease of the monomers which was caused by the formation of MBs aggregates in the presence of SARS-CoV-2 IgG.

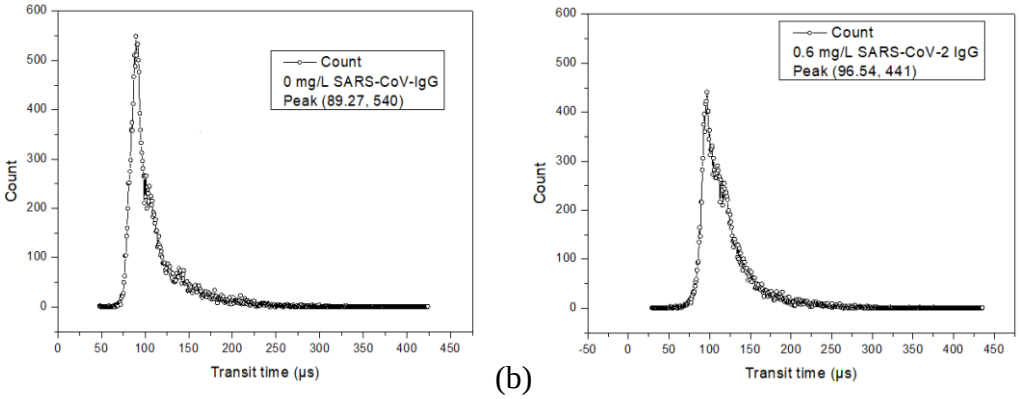

(a) (b)

Figure 4-7: The distribution of transit time. (a) a negative sample of SARS-CoV-2 IgG; (b) A SARS-CoV-2 IgG sample containing 0.6 mg/L.

Compared with the transit time distribution of the negative sample, the transit time distribution of 0.6 mg/L SARS-CoV-2 IgG tended to locate at a higher transit time range.

Figure 4-8 shows the correlation between the average transit time and the concentration of SARS-CoV-2 IgG. The y-axis is the average transit time, and x-axis is the concentration of SARS-CoV-2 IgG, Each black square, red triangle, and the blue circle represents the average results of triplicated measurements obtained from the anti-SARS-CoV-2 IgG conjugated MBs with storage time of one day, eight days, and fifteen days, respectively. Different colored lines are the linear fit of the average of the testing. Although the performance of the anti-SARS-CoV-2 IgG conjugated MBs decreased by the storage time which was shown in the decrease of the slope as the increase of the storage time, the correlation between the average transit time and the concentration of SARS-CoV-2 IgG remained strong. The correlation coefficient for all curves were larger than 0.99.

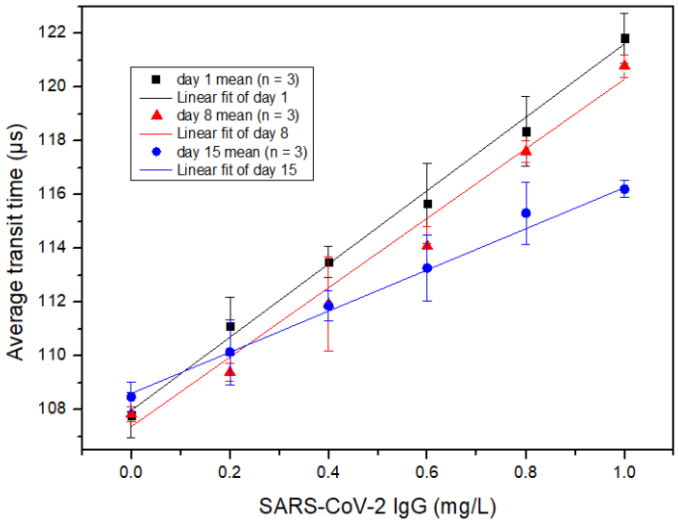

Figure 4-8: Scatter plot showing the correlation between the average transit time and the concentration of SARS-CoV-2 IgG.

The LOD of the MCAIA for SARS-CoV-2 IgG detection was calculated according to the Eq.3.2 and it was 0.1 mg/L. A study reported a in-house ELSIA method for SARS-CoV-2 IgG detection with a LOD of 0.04 mg/L, which was comparable to that of the MCAIA [124]. However, the assay range was restricted by the Hook effect and the upper limit was 1 mg/L. Therefore, proper dilution of the samples is needed to avoid false-negative results.

Compared the detection results of SARS-CoV-2 IgM in Figure 4-5 and the SARS-CoV-2 IgG in Figure 4-8, the linear fit curves of SARS-CoV-2 IgM is steeper than the SARS-CoV-2 IgG, implying that the MCAIA for the detection of SARS-CoV-2 IgM is more sensitive than the detection of SARS-CoV-2 IgG. This is attributed to the pentameric structure of IgM, which enlarges the possibility of the aggregates formation.

4.4 The spike-and-recovery experiments

All the SARS-CoV-2 antibody samples were prepared with the diluent of PBS. To determine whether the difference between the PBS diluent and the real biological samples will affect the performance of SARS-CoV-2 antibody detection using the MCAIA, spike-and-recovery experiments were performed to evaluate the impact of the sample matrix.

For SARS-CoV-2 IgM detection, the spike-and-recovery experiments were performed as followed. Two identical 8 µL SARS-CoV-2 IgM samples were prepared using the diluent of PBS. 2 µL of concentrated standard of SARS-CoV-2 IgM which was prepared by human serum (H4522, Human serum, Sigma-Aldrich, Oakville, ON Canada) was spiked into one sample. 2 µL of deionized water was added into the other sample. Both samples were

detected by the MCAIA in the same way and the concentration of SARS-CoV-2 IgM was determined by the calibration curve of day 1 detection results of SARS-CoV-2 in Figure 4-5. Each detection was repeated once, and the average of the detection results was used to calculate the recovery index. The recovery index was calculated using the following Eq.4.1. In this equation, $C_{spiked\ sample}$ is the concentration of sample which was added with concentrated standard of SARS-CoV-2 IgM. $C_{unspiked\ sample}$ represents the concentration of sample which was added with 2 µL of deionized water. C_{added} is the concentration of the concentrated standard diluted to 10 µL. $C_{unspiked\ sample}$ was prepared at a concentration of 0.4 mg/L and C_{added} was prepared at a concentration of 0.4 mg/L. If the recovery index was 100%, the measured $C_{spiked\ sample}$ should be 0.8 mg/L. The spike-and-recovery experiments for SARS-CoV-2 IgG were performed in a similar way to SARS-CoV-2 IgM.

$$\%\ Recovery\ index = \frac{C_{spiked\ sample} - C_{unspiked\ sample}}{C_{added}} \times 100\% \qquad 4.1$$

4.5 The recovery index

The calibration curve for SARS-CoV-2 IgM day 1 detection shown in Figure 4-5 was $y = 24.964 \times x + 105.73$, and the calibration curve for SARS-CoV-2 IgG day 1 detection shown in Figure 4-8 was $y = 13.442 \times x + 107.99$. The recovery index for SARS-CoV-2 IgM and SARS-CoV-2 IgG were 96.85% and 98.98%, respectively. Both recovery indexes were acceptable in the viewpoint of practical application.

4.6 The conjugation efficiency of secondary antibodies to MBs

To evaluate the conjugation efficiency of secondary antibodies to MBs, the goat anti-human

IgM secondary antibody modified with horseradish peroxidase (HRP) (31415, Thermo Fisher Scientific, Rockford, IL, USA) was used for antibody coupling to MBs. Amplex ultrared reagent (AUR) (A36006, Life Technologies, Burlington, ON, Canada) was used as a fluorogenic substrate for HRP that can catalyze the oxidation of the substrate with hydrogen peroxide (H_2O_2). Amplex red/ultrared stop reagent was used to terminate the fluorescence generation reaction. A signal of color change was detected by the microplate reader (BioTek NEO2 Malphab, BioTek Instruments Inc., Winooski, VT, USA). The experiments were performed according to the user manual provided by the AUR. Figure 4-9 (a) shows the principle of the fluorescence generation reaction using AUR. The substrate was oxidized by H_2O_2 with the catalyst of HRP and a colored product of resorufin was generated. Figure 4-9 (b) shows the pictures microplate containing colored product of fluorescence generation reaction using the AUR.

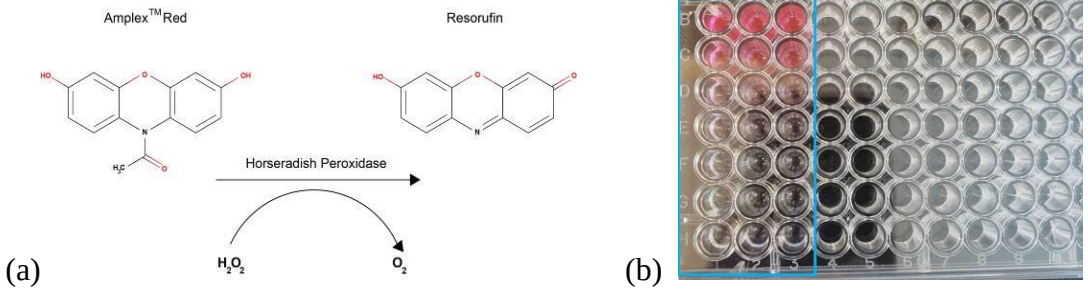

Figure 4-9: The fluorescence generation reaction with AUR. (a) The principle of the fluorescence generation reaction; (b) the picture of multi-well micropleate shown the colored product of the reaction.

The wells from row H to B were added with 7 point 1:5 dilution series of HRP-labelled goat anti-human IgM secondary antibody conjugated MBs. Each sample was prepared in

triplicate from column 1 to 3. The color became darker as the concentration of the conjugated MBs increased.

Figure 4-10 (a) shows the relationship between the measured fluorescent intensity and the normalized concentration of MBs. The y-axis is the intensity of the fluorescence in relative fluorescence unites (RFU) at 585 nm, and the x-axis is the normalized concentration of MBs, which were coated with HRP-labelled goat anti-human IgM secondary antibodies. The concentration of MBs was linearly correlation with the concentration of HRP. Figure 4-10 (b) shows the relationship between the normalized enhancement of the signal and the concentration of HRP obtained from the user manual using different substrate including AUR in solid line and tetramethylbenzidine (TMB) in dashed line. The y-axis is the normalized enhance fluorescence signals, and the x-axis is the concentration of HRP.

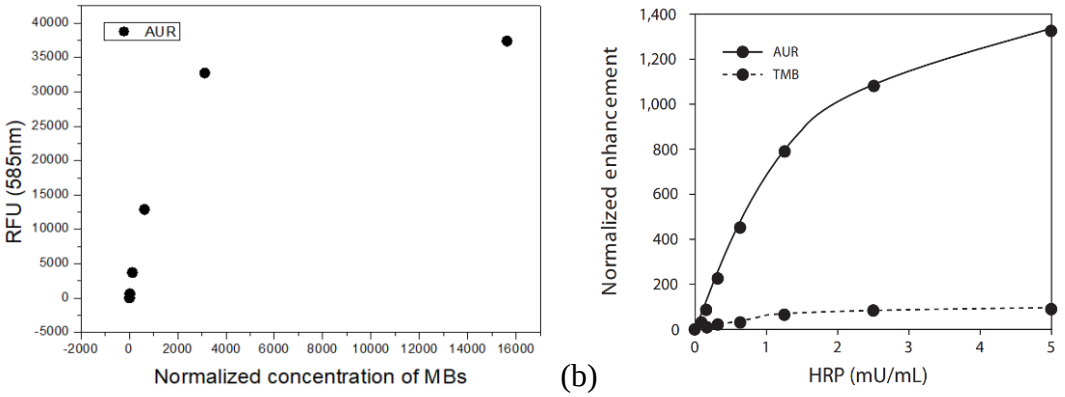

Figure 4-10: (a) The relationship between the RFU and the concentration of HRP-labelled goat anti-human IgM secondary antibody conjugated MBs; (b) The relationship between the normalized enhancement of fluoresence signals and the concentration of HRP with AUR and TMB substrate used (provdied by the user manual).

Compared the relationship between the fluorescence intensity and the concentration of HRP

in Figure 4-10 (a) and (b), the trend of the increase was similar to each other. Both the increase rates decreased by the concentration of HRP. It can be concluded that HRP-labelled goat anti-human IgM secondary antibody has been coupled to the surface of MBs successfully.

4.7 The cross-reaction between the SARS-CoV-2 and SARS-CoV

To evaluate the accuracy of the MCAIA for SARS-CoV-2 antibody detection, SARS-CoV IgG was used to test the cross-reaction between SARS-CoV-2 and SARS-CoV. The procedure for SARS-CoV IgG detection using the MCAIA was identical to SARS-CoV-2 antibody detection. The SARS-CoV-2 IgG and SARS-CoV IgG were measured in parallel. Figure 4-11 shows the detection results of the cross-reaction between SARS-CoV-2 IgG and SARS-CoV IgG (PA1-41141, Life Technologies, Burlington, ON, Canada). The y-axis is the average transit time, and the x-axis is the concentration of antibodies. There is a linear relationship between the concentration of SARS-CoV-2 IgG and the average transit time, which was shown in red square with red linear fit. However, a certain concentration of SARS-CoV IgG can cause the increase of the average transition time, which was shown in blue circle. This phenomenon could be explained by the high similarity (75%) between the genomes of SARS-CoV-2 and SARS-CoV [125]. Furthermore, it was mentioned by the product information of SARS-CoV IgG that the immunogen of SARS-CoV IgG is 69% homologous to SARS-CoV-2 spike antibody. From the viewpoint of practical application, the cross-reaction result from the SARS-CoV will not affect the SARS-CoV-2 screening dramatically due to the number of confirmed cases of SARS-CoV being 8098, which is

quite small compared to the over a hundred million cases of SARS-CoV-2.

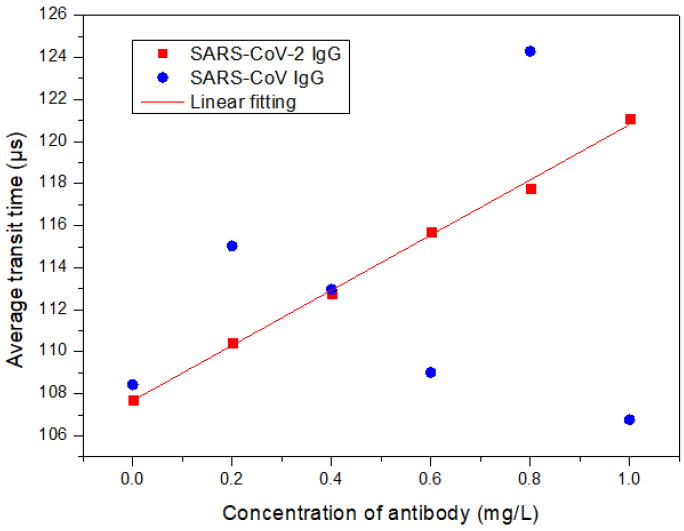

Figure 4-11: The cross-reaction between SARS-CoV-2 and SARS-CoV.

4.8 The nonspecific background noise

For practical application of SARS-CoV-2 antibody detection by the MCAIA, the background IgM and IgG in healthy individuals need to be considered as a possible nonspecific background noise. Normally, the concentration of IgM and IgG in healthy individuals are 400-3450 mg/L and 6000-16000 mg/L, respectively. The IgM secondary antibodies and IgG secondary antibodies on the surface of the MBs will capture the background IgM and IgG if they exist in the sample. SARS-CoV-2 IgG was chosen to evaluate the effect of the background antibody in the sample. Rabbit IgG isotype control was used as a negative control to evaluate the nonspecific background noise from healthy individuals. Figure 4-12 shows the comparative detection results between SARS-CoV-2 IgG and IgG isotype control. The y-axis is the average transit time, and the x-axis is the

concentration of antibody. The bule circle and red square represent the detection results of IgG isotype control and SARS-CoV-2 IgG, respectively. The linear relationship between the average transit time and the concentration of SARS-CoV-2 IgG was obvious. However, the average transit time did not show significant change as the concentration of IgG isotype control increased. It can conclude that the existence of IgG in healthy individuals will not affect the detection of SARS-CoV-2 IgG.

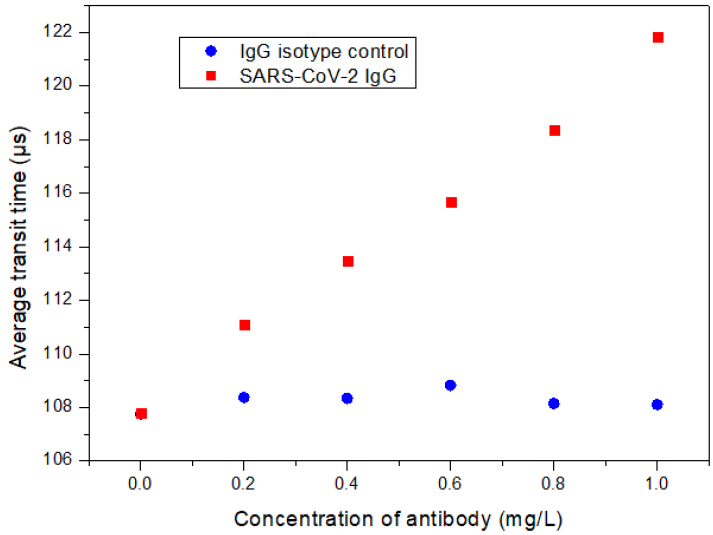

Figure 4-12: Comparative results between the SARS-CoV-2 IgG and IgG isotype control.

Chapter 5 Conclusion and Recommendations

5.1 Conclusion

This study has proposed a MCAIA for on-site antigen and antibody medical diagnosis. The MCAIA is based on the principles of the particle counting immunoassay, where the concentration of the analyte is correlated to the decrease in free particles caused by the immune reaction in the assay mixture. Superparamagnetic beads with modified surfaces were used as the solid support for the immunoassay. Microflow cytometry was employed to count the assay mixture and SSC light signals were collected. The data was analyzed by the custom LabVIEW program. The concentration of the antigen or antibody was determined by analyzing the data in terms of amplitude or transit time of the signals. The decrease of monomers is proportional to the increase in the number of aggregates in the assay mixture, which will cause the distribution of the amplitude or average transit time to shift towards a higher range. For data analyzed using the amplitude, a Gaussian fit was used to distinguish monomers from aggregates and the correlation between the proportion of monomers in the assay mixture and the concentration of analyte was established. For data analyzed using the transit time, the increase in aggregates lengthened the average transit time. A relationship between the average transit time and the concentration of analyte was established. The combination of microflow cytometry and the particle counting immunoassay make the MCAIA a competitive tool for on-site detection of antigen and antibody.

For antigen detection, CRP was chosen to illustrate the principle and procedure of the

MCAIA. CRP is a well-known biomarker of tissue damage and inflammation. As described in the introduction, an elevated concentration of CRP in the blood is associated with various diseases. Routine detection of CRP by the MCAIA can help individuals monitor fluctuations in the concentration of CRP and treatments can be quickly provided if the concentration of CRP is outside the normal range. The principle of the MCAIA for CRP detection was first verified by the microscopic agglutination immunoassay and then the formulation was verified by commercial flow cytometry. The MCAIA was proven to be a sensitive and accurate technology for CRP detection. A linear relationship was established between the proportion of monomers and the concentration of CRP by analysing the data using amplitude. However, the amplitude was easily affected by the shaping and alignment of the laser beam, so the average transit time was employed to analyze the data as well. A linear relationship was established between the average transit time and the concentration of CRP. A LOD of 0.09 mg/L and assay range up to 1 mg/L CRP were achieved. The normal range of CRP in healthy individuals is lower than 10 mg/L, so a 10-fold dilution of the serum sample is needed when CRP is detected by the MCAIA. The assay time was approximately 10 min and only 10 μL of serum sample was needed for each testing. To test the accuracy of CRP detection by the MCAIA, traditional turbidimetric immunoassays were performed in parallel. A correlation coefficient of 0.9792 was found between the MCAIA and the turbidimetric immunoassay, implying that the MCAIA is accurate enough for CRP measurement. The interference of hemoglobin in CRP detection using the MCAIA was evaluated, and no remarkable impact was found.

For antibody detection, SARS-CoV-2 antibodies were chosen as models to demonstrate the principle of the MCAIA. Since the outbreak of the SARS-CoV-2 pandemic, human health and the economy has been globally compromised. Serological assays can play an important role in the mass screening of SARS-CoV-2 infections and, thus, can be utilized to help control the spread of the virus. The procedures for SARS-CoV-2 IgM and IgG detection by the MCAIA were described. A linear relationship between the average transit time and the concentration of SARS-CoV-2 IgM was established. A LOD of 0.06 mg/L and an assay range up to 1 mg/L SARS-CoV-2 IgM was found. Similar results for SARS-CoV-2 IgG was obtained, and a LOD of 0.1 mg/L and an assay range up to 1 mg/L SARS-CoV-2 IgG was found. The assay time was approximately 30 min and only 10 µL of serum sample was needed for each testing. A decreased performance of the conjugated MBs with increased storge time was found when the assays were performed with conjugated MBs stored for different durations of time. To mimic real serum samples containing SARS-CoV-2 antibodies, a known amount of SARS-CoV-2 IgM and IgG were spiked into human serum to calculate the recovery index. The recovery index for SARS-CoV-2 IgM and SARS-CoV-2 IgG were 96.85% and 98.98%, respectively, indicating that the MCAIA is competent for SARS-CoV-2 antibody detection in a practical application. The conjugation efficiency of the secondary antibodies to the MBs was estimated by using the HRP labelled secondary antibodies and it turned out that the secondary antibodies were successfully immobilized by the functional groups on the surface of the MBs. A cross-reaction between the SARS-CoV-2 virus and SARS-CoV antibodies in the MCAIA was found. However, due to the relatively low amount of reported 8098 cases of the SARS-CoV over approximately 140

million of SARS-CoV-2 (as of April 21, 2021), the false positives caused by SARS-CoV antibodies were negligible. Furthermore, an IgG isotype control was used as negative control to test the possible background noise resulting from the inherent concentration of IgG in healthy individuals. The existence of IgG in healthy individuals will not affect the detection of SARS-CoV-2 IgG by the MCAIA as the IgG isotype control did not produce a positive result in the MCAIA.

In brief, the proposed MCAIA is a sensitive and accurate technology for CRP and SARS-CoV-2 antibody quantitative detection. By replacing the corresponding antibodies or secondary antibodies specific for the targeted analyte, the MCAIA can be used for on-site detection of other kinds of antigens or antibodies.

The preliminary results of CRP detection by the MCAIA were presented on Photonics North 2020. The details of the MCAIA for CRP detection has been published on Micromachines in January 2021. The results of the MCAIA for SARS-CoV-2 antibody detection has been published on Micromachines in April 2021.

5.2 Recommendations

Although some satisfying preliminary results were obtained from the CRP and SARS-CoV-2 antibody detection using the MCAIA, due to the time constrains, there are still some aspects of this work that need to be improved in the future.

First, the assay mixture for the current MCAIA needs to be prepared manually. The assay mixture should also be introduced to the syringe system manually. These manual steps will

introduce uncertainties and affect the consistency of the testing results. Hence, the whole system needs be designed to be fully automatic to improve the practical performance of the MCAIA.

Second, the MBs used as the solid support for antibodies can be altered to improve the performance of the MCAIA. Although the issue of MB sedimentation was solved by storing the assay mixture perpendicularly close to the inlet of the microfluidic chip and thus the aggregates in the assay mixture were interrogated by the laser beam in a shorter time, other solid spheres, such as gel-made spheres, may not from sediments and thus can be used to improve the detection sensitivity of the MCAIA.

Third, the antigen used for the detection of SARS-CoV-2 antibodies in this work was the spike S1-His recombinant protein; the nucleocapsid protein should also be used to improve the performance of the MCAIA. Furthermore, more experiments of the cross-reaction between SARS-CoV and SARS-CoV-2 are needed to support the impact of SARS-CoV antibody to the screening of SARS-CoV-2 infections.

Fourth, the assay range of the MCAIA is limited by the Hook effect, which is a normal immunological phenomenon. Although a proper dilution process can be used to avoid false-negative results, efforts should be made to mitigate the Hook effect in future work.

Reference

[1] N. W. Schaad, D. Opgenorth, and P. Gaush, "Real-time polymerase chain reaction for one-hour on-site diagnosis of Pierce's disease of grape in early season asymptomatic vines," *Phytopathology*, vol. 92, no. 7, pp. 721–728, 2002.

[2] A. T. Mobashsher and A. M. Abbosh, "On-site rapid diagnosis of intracranial hematoma using portable multi-slice microwave imaging system," *Sci. Rep.*, vol. 6, no. November, pp. 1–17, 2016.

[3] M. Packer, "What causes sudden death in patients with chronic heart failure and a reduced ejection fraction?," *Eur. Heart J.*, vol. 41, no. 18, pp. 1757–1763, 2020.

[4] S. Wangsiricharoen, S. Lekawanvijit, and S. Rangdaeng, "Agreement between rapid on-site evaluation and the final cytological diagnosis of salivary gland specimens," *Cytopathology*, vol. 28, no. 4, pp. 321–328, 2017.

[5] Aimo Harmoinen, "Rapid quantitative determination of C-reactive protein using laser-nephelometer," *Scand. J. clin. Lab. Invest*, vol. 40, no. 3, pp. 293–295, 1980.

[6] H. et al. Chen Y, Chan KH, "A highly specific rapid antigen detection assay for on-site diagnosis of MERS," *J Infect.*, vol. 73, no. January, pp. 82–97, 2016.

[7] H. Xiong, X. Ye, Y. Li, J. Qi, X. Fang, and J. Kong, "Efficient microfluidic-Based air sampling/monitoring platform for detection of aerosol SARS-CoV-2 On-site," *Anal. Chem.*, vol. 93, no. 9, pp. 4270–4276, 2021.

[8] R. Raman *et al.*, "Evaluating diagnostic point-of-care tests in resource-limited settings," *Lancet Infec Dis*, vol. 23, no. 4, pp. 333–336, 2010.

[9] W. S. Tillett and T. Francis, "Serological reactions in pneumonia with a nonprotein somatic fraction of pneumococcus," *J. Exp. Med.*, vol. 52, no. 4, pp. 561–571, 1930.

[10] B. Y. W. S. Tillett, W. F. Goebel, and O. T. Avery, "Chemical and immunological properties of a species-specific carbohydrate of pneumococci," *J. Exp. Med.*, vol. 52, no. 6, pp. 895–900, 1930.

[11] M. D. Cem Gabay, M.D., Irving Kushner, "Acute-phase proteins and other systemic responses to inflammation," *N Engl J Med*, vol. 340, pp. 448–454, 1999.

[12] M. Mecarty, "The occurrence during acute infections of a protein not normally present in the blood iv crystallization of the c-reactive protein," *J. Exp. Med.*, vol. 85, no. 5, pp. 491–498, 1947.

[13] D. Thompson, M. B. Pepys, and S. P. Wood, "The physiological structure of human C-reactive protein and its complex with phosphocholine," *Structure*, vol. 7, no. 2, pp. 169–177, 1999.

[14] M. Mecarty, "The occurrence during acute infections of a protein not normally present in

the blood," *J. Exp. Med.*, vol. 85, no. 5, pp. 491–498, 1947.

[15] U. Ganter, R. Arcone, C. Toniatti, G. Morrone, and G. Ciliberto, "Dual control of C-reactive protein gene expression by interleukin-1 and interleukin-6," *EMBO J.*, vol. 8, no. 12, pp. 3773–3779, 1989.

[16] B. Shine, F. C. De Beer, and M. B. Pepys, "Solid phase radioimmunoassays C-reactive protein for human," *Clin. Chim. Acta*, vol. 117, pp. 13–23, 1981.

[17] S. Woloshin and L. M. Schwartz, "Distribution of C-reactive protein values in the United States [7]," *N. Engl. J. Med.*, vol. 352, no. 15, pp. 1611–1613, 2005.

[18] S. Yamada *et al.*, "Distribution of serum C-reactive protein and its association with atherosclerotic risk factors in a Japanese population," *Am. J. Epidemiol.*, vol. 153, no. 12, pp. 1183–1190, 2001.

[19] R. A. Rabinovitch, S. M. Koethe, J. H. Kalbfleisch, L. C. Preheim, and M. W. Rytel, "Relationships between alternative complement pathway activation, C-reactive protein, and pneumococcal infection," *J. Clin. Microbiol.*, vol. 23, no. 1, pp. 56–61, 1986.

[20] T. F. Lint and C. Mold, "A role for C-reactive protein in the complement-mediated stimulation of human neutrophils by type 27 Streptococcus pneumoniae," *J Immunol*, vol. 128, no. 6, pp. 2493–2496, 1982.

[21] H. Müller and J. Fehr, "Binding of C-reactive protein to human polymorphonuclear leukocytes: evidence for association of binding sites with Fc receptors.," *J. Immunol.*, vol. 136, no. 6, pp. 2202–7, 1986.

[22] H. G. Joan Siegel, Rosemarie Rent, "Interactions of C-reactive protein with the complement system," *J Exp Med*, vol. 140, no. 3, pp. 631–647, 1974.

[23] C. R. A. and H. G. J. C Mold, C P Rodgers, R L Richards, "Interaction of C-reactive protein with liposomes. III. Membrane requirements for binding," *J Immunol*, vol. 126, no. 3, pp. 856–860, 1981.

[24] T. W. Du Clos, "Function of C-reactive protein," *Ann. Med.*, vol. 32, no. 4, pp. 274–278, 2000.

[25] B. Y. et Al, "C-reactive protein: a critical review," *Pathology*, vol. 23, no. 2, pp. 118–124, 1991.

[26] P. L. McCarthy, A. L. Frank, R. C. Ablow, S. J. Masters, and T. F. Dolan, "Value of the C-reactive protein test in the differentiation of bacterial and viral pneumonia," *J. Pediatr.*, vol. 92, no. 3, pp. 454–456, 1978.

[27] E. -M Salonen and A. Vaheri, "C-reactive protein in acute viral infections," *J. Med. Virol.*, vol. 8, no. 3, pp. 161–167, 1981.

[28] H. C. Ablij and A. E. Meinders, "C-reactive protein: History and revival," *Eur. J. Intern. Med.*, vol. 13, no. 7, pp. 412–422, 2002.

[29] I. G. Otterness, "The value of C-reactive protein measurement in rheumatoid arthritis," *Semin. Arthritis Rheum.*, vol. 24, no. 2, pp. 91–104, 1994.

[30] G. J. Becker, M. Waldburger, G. R. V. Hughes, and M. B. Pepys, "Value of serum C-reactive protein measurement in the investigation of fever in systemic lupus erythematosus," *Ann. Rheum. Dis.*, vol. 39, no. 1, pp. 50–52, 1980.

[31] F. Karadag, S. Kirdar, A. B. Karul, and E. Ceylan, "The value of C-reactive protein as a marker of systemic inflammation in stable chronic obstructive pulmonary disease," vol. 19, no. 2, pp. 104–108, 2008.

[32] H. Tomoda and N. Aoki, "Prognostic value of C-reactive protein levels within six hours after the onset of acute myocardial infarction," *Am. Heart J.*, vol. 140, no. 2, pp. 324–328, 2000.

[33] M. Adamina, T. Steffen, I. Tarantino, U. Beutner, B. M. Schmied, and R. Warschkow, "Meta-analysis of the predictive value of C-reactive protein for infectious complications in abdominal surgery," *Br. J. Surg.*, vol. 102, no. 6, pp. 590–598, 2015.

[34] X. Sun and H. Wang, "The prognostic value of C-reactive protein / albumin ratio in human malignancies : an updated meta- analysis," *Onco Targets Ther.*, vol. 10, pp. 3059–3070, 2017.

[35] A. D. Stirling, N. R. Moran, M. E. Kelly, P. F. Ridgway, and K. C. Conlon, "The predictive value of C-reactive protein (CRP) in acute pancreatitis – is interval change in CRP an additional indicator of severity ?," *Int. Hepato-Pancreato-Biliary Assoc.*, vol. 19, no. 10, pp. 874–880, 2017.

[36] Pedro Póvoa, "C-reactive protein : a valuable marker of sepsis," *Intensive Care Med.*, vol. 28, pp. 235–243, 2002.

[37] H. Moon, B. Park, and D. Moon, "Coloproctology diagnostic calue of C-reactive protein in complicated appendicitis Coloproctology," *J. Korean Soc. Coloproctol.*, vol. 27, no. 3, pp. 122–126, 2011.

[38] P. Chamouard, Z. O. E. Richert, N. Meyer, G. Rahmi, and R. Baumann, "Level of Crohn ' s disease," *Clin. Gastroenterol. hepatplogy*, vol. 4, no. 7, pp. 882–887, 2006.

[39] G. Schillaci and M. Pirro, "C-reactive protein in hypertension : clinical significance and predictive value," *Nutr. Metab. Cardiovasc. Dis.*, vol. 16, no. 7, pp. 500–508, 2006.

[40] X. Luo *et al.*, "Prognostic value of C-reactive protein in patients with Coronavirus 2019," *Clin. Infect. Dis.*, vol. 71, no. 16, pp. 2174–2179, 2020.

[41] H. Thomas *et al.*, "Global atlas of cardiovascular disease 2000-2016: the path to prevention and control," *Glob. Heart*, vol. 13, no. 3, pp. 143–163, 2018.

[42] H. C. M. Jr, C. A. Mcmahan, and S. S. Gidding, "Preventing heart disease in the 21st century implications of the pathobiological determinants of atherosclerosis in youth (PDAY) study," *Circulation*, vol. 117, no. 9, pp. 1216–1227, 2008.

[43] H. Tunstall-pedoe, "Cardiovascular risk and risk scores : ASSIGN , Framingham , QRISK and others : how to choose," *Heart*, vol. 97, no. 6, pp. 442–444, 2011.

[44] R. Poplin *et al.*, "Prediction of cardiovascular risk factors from retinal fundus photographs

via deep learning," *Nat. Biomed. Eng.*, vol. 2, no. March, 2018.

[45] Irene M. van der Meer. et al, "The value of C-reactive protein in cardiovascular risk prediction," *Arch intern med*, vol. 163, no. 11, pp. 1323–1328, 2003.

[46] T. A. Pearson *et al.*, "Markers of inflammation and cardiovascular disease," *Circulation*, vol. 107, no. 3, pp. 499–511, 2003.

[47] P. M. Ridker, R. J. Glynn, and C. H. Hennekens, "C-reactive protein adds to the predictive value of total and HDL cholesterol in determining risk of first myocardial infarction," *Circulation*, vol. 97, no. 20, pp. 2007–2011, 1998.

[48] R. Ria, A. Reale, A. Vacca, and S. Internal, "Prospects and advancements in C-reactive protein detection," *World J. methodology*, vol. 4, no. 2, pp. 73–91, 2014.

[49] R. A. Donald L. Bornstein , Gerald Schiffman , Harriet P. Bernheimer, "Capsulation of pneumococcus with soluble c-like (Cs) polysaccharide: I. Biological and genetic properties of Cs pneumococcal strains," *J. Exp. Med.*, vol. 128, no. 6, pp. 1385–1400, 1968.

[50] D. Selman, "Pitfalls in the determination of C-reactive protein, an acute-phase reactant," *Angiology*, vol. 7, no. 3, pp. 292–304, 1956.

[51] D. R. Claus, A. P. Osmand, and H. Gewurz, "Radioimmunoassay of human C-reactive protein and levels in normal sera," *J. Lab. Clin. Med.*, vol. 87, no. 1, pp. 120–128, 1976.

[52] M. Fukuda, C. L. Heiskell, and C. M. Carpenter, "A method for quantitative determination of C-reactive protein using gel-diffusion," *Am. J. Clin. Pathol.*, vol. 32, no. 6, pp. 507–512, Dec. 1959.

[53] L.-Å. Nilsson, "Comparative testing of precipitation methods for quantitation of C-reactive protein in blood serum," *Acta Pathol. Microbiol. Scand.*, vol. 73, no. 1, pp. 129–144, 1968.

[54] M. Sarikaputi, M. Morimatsu, S. Yamamoto, B. Syuto, M. Saito, and M. Naiki, "Latex agglutination test: a simple, rapid and practical method for bovine serum CRP determination.," *Jpn. J. Vet. Res.*, vol. 40, no. 1–2, pp. 1–12, 1992.

[55] J. E. Roederer and G. J. Bastiaans, "Microgravimetric immunoassay with piezoelectric crystals," *Anal. Chem.*, vol. 55, no. 14, pp. 2333–2336, 1983.

[56] K. Shigeru, "Latex piezoelectric immunoassay: detection of agglutination of antibody-bearing latex using a piezoelectric quartz crystal," *Chem. Pharm. Bull.*, vol. 57, no. 534, pp. 364–370, 2002.

[57] E. Layne, "Spectrophotometric and turbidimetric methods for measuring proteins," *Methods Enzymol.*, vol. 3, no. 73, pp. 447–454, 1957.

[58] I. P. A. Morais, I. V. Tóth, and A. O. S. S. Rangel, "Turbidimetric and nephelometric flow analysis: Concepts and applications," *Spectrosc. Lett.*, vol. 39, no. 6, pp. 547–579, 2006.

[59] S. Otsuji, H. Shibata, and M. Umeda, "Turbidimetric immunoassay of serum C-reactive protein," *Clin. Chem.*, vol. 28, no. 10, pp. 2121–2124, 1982.

[60] T. B. Ledue and N. Rifai, "High sensitivity immunoassays for C-reactive protein: promises

and pitfalls," vol. 39, no. 11, pp. 1171–1176, 2005.

[61] T. E. Strandberg and R. S. Tilvis, "Mortality in a prospective study in the elderly," *Arter. Thromb Vasc Biol*, no. 20, pp. 1057–1060, 2000.

[62] K. Kåpyaho, P. Tanner, T. Kårkkåinen, and T. Weber, "Rapid determination of C-reactive protein by enzyme immunoassay using two monoclonal antibodies," *Scand. J. Clin. Lab. Invest.*, vol. 49, no. 4, pp. 389–393, 1989.

[63] O. Senju *et al.*, "A new immuno quantitative method by latex agglutination-application for the determination of serum C-reactive protein (CRP) and its clinical significance.," *J. Clin. Lab. Immunol.*, vol. 19, no. 2, pp. 99–103, Feb. 1986.

[64] W. L. Hutchinson, W. Koenig, M. Fröhlich, M. Sund, G. D. O. Lowe, and M. B. Pepys, "Immunoradiometric assay of circulating C-reactive protein: Age-related values in the adult general population," *Clin. Chem.*, vol. 46, no. 7, pp. 934–938, 2000.

[65] S. Eda, J. Kaufmann, W. Roos, and S. Pohl, "Development of a new microparticle-enhanced turbidimetric assay for C- reactive protein with superior features in analytical sensitivity and dynamic range," *J. Clin. Lab. Anal.*, vol. 12, no. 3, pp. 137–144, 1998.

[66] H. Y. Wang *et al.*, "Circulating endothelial progenitor cells, c-reactive protein and severity of coronary stenosis in Chinese patients with coronary artery disease," *Hypertens. Res.*, vol. 30, no. 2, pp. 133–141, 2007.

[67] T. L. Wu, K. C. Tsao, C. P. Y. Chang, C. N. Li, C. F. Sun, and J. T. Wu, "Development of ELISA on microplate for serum C-reactive protein and establishment of age-dependent normal reference range," *Clin. Chim. Acta*, vol. 322, no. 1–2, pp. 163–168, 2002.

[68] N. Pamme, "Magnetism and microfluidics," *Lab Chip*, vol. 6, no. 1, pp. 24–38, 2006.

[69] M. A. M. Gijs, F. Lacharme, and U. Lehmann, "Microfluidic applications of magnetic particles for biological analysis and catalysis," *Chem. Rev.*, vol. 110, no. 3, pp. 1518–1563, 2010.

[70] C. Phurimsak, M. D. Tarn, S. A. Peyman, J. Greenman, and N. Pamme, "On-chip determination of c-reactive protein using magnetic particles in continuous flow," *Anal. Chem.*, vol. 86, no. 21, pp. 10552–10559, 2014.

[71] Y. Moser, T. Lehnert, and M. A. M. Gijs, "On-chip immuno-agglutination assay with analyte capture by dynamic manipulation of superparamagnetic beads," *Lab Chip*, vol. 9, no. 22, pp. 3261–3267, 2009.

[72] Y. N. Yang, H. I. Lin, J. H. Wang, S. C. Shiesh, and G. Bin Lee, "An integrated microfluidic system for C-reactive protein measurement," *Biosens. Bioelectron.*, vol. 24, no. 10, pp. 3091–3096, 2009.

[73] Czilwik G, "Magnetic chemiluminescent immunoassay for human C-reactive protein on the centrifugal microfluidics platform," *R. Soc. Chem.*, vol. 5, no. 24, pp. 61906–61912, 2015.

[74] K. Hosokawa, M. Omata, K. Sato, and M. Maeda, "Power-free sequential injection for microchip immunoassay toward point-of-care testing," *Lab Chip*, vol. 6, no. 2, pp. 236–241,

2006.

[75] K. Kriz, F. Ibraimi, D. Kriz, M. Lu, and L. O. Hansson, "Rapid one-step whole blood C-reactive protein magnetic permeability immunoassay with monoclonal antibody conjugated nanoparticles as superparamagnetic labels and enhanced sedimentation," *Anal. Bioanal. Chem.*, vol. 384, no. 3, pp. 651–657, 2006.

[76] Z. Yang, Y. Liu, C. Lei, X. cheng Sun, and Y. Zhou, "A flexible giant magnetoimpedance-based biosensor for the determination of the biomarker C-reactive protein," *Microchim. Acta*, vol. 182, no. 15–16, pp. 2411–2417, 2015.

[77] L. Guo, Z. Yang, S. Zhi, Z. Feng, C. Lei, and Y. Zhou, "A sensitive and innovative detection method for rapid C-reactive proteins analysis based on a micro-fluxgate sensor system," *PLoS One*, vol. 13, no. 3, pp. 1–17, 2018.

[78] N. Pamme, R. Koyama, and A. Manz, "Counting and sizing of particles and particle agglomerates in a microfluidic device using laser light scattering: Application to a particle-enhanced immunoassay," *Lab Chip*, vol. 3, no. 3, pp. 187–192, 2003.

[79] Z. Ma, P. Zhang, Y. Cheng, S. Xie, S. Zhang, and X. Ye, "Homogeneous agglutination assay based on micro-chip sheathless flow cytometry," *Biomicrofluidics*, vol. 9, no. 6, pp. 1–11, 2015.

[80] C. J. M. Sindic, "The use of particle counting immunoassay for the diagnosis of neurological disease," *J. Pharm. Biomed. Anal.*, vol. 5, no. 2, pp. 105–111, 1987.

[81] P. L. Masson, "Particle counting immunoassay (PACIA)," *Methods Enzymol.*, vol. 74, no. 6, pp. 106–140, 1981.

[82] Y. Zhang, B. R. Watts, T. Guo, Z. Zhang, C. Xu, and Q. Fang, "Optofluidic device based microflow cytometers for particle/cell detection: A review," *Micromachines*, vol. 7, no. 4, pp. 1–21, 2016.

[83] E. Petersen *et al.*, "Comparing SARS-CoV-2 with SARS-CoV and influenza pandemics," *Lancet Infect. Dis.*, vol. 20, no. 9, pp. e238–e244, 2020.

[84] I. Astuti and Ysrafil, "Severe acute respiratory syndrome Coronavirus 2 (SARS-CoV-2): An overview of viral structure and host response," *Diabetes Metab. Syndr. Clin. Res. Rev.*, vol. 14, no. 4, pp. 407–412, 2020.

[85] Y. M. Bar-On, A. Flamholz, R. Phillips, and R. Milo, "SARS-CoV-2 (Covid-19) by the numbers," *arXiv*, vol. 2, pp. 1–15, 2020.

[86] W. Zeng *et al.*, "Biochemical characterization of SARS-CoV-2 nucleocapsid protein," *Biochem. Biophys. Res. Commun.*, vol. 527, no. 3, pp. 618–623, 2020.

[87] A. C. Walls, Y. J. Park, M. A. Tortorici, A. Wall, A. T. McGuire, and D. Veesler, "Structure, function, and antigenicity of the SARS-CoV-2 spike glycoprotein," *Cell*, vol. 181, no. 2, pp. 281-292.e6, 2020.

[88] L. Kuo, K. R. Hurst-hess, C. A. Koetzner, and P. S. Masters, "Analyses of coronavirus assembly interactions with interspecies membrane and nucleocapsid protein chimeras," *J.*

Virol., vol. 90, no. 9, pp. 4357–4368, 2016.

[89] E. A. J Alsaadi and I. M. Jones, "Membrane binding proteins of coronaviruses," *Future* Virol., vol. 14, no. 4, pp. 275–286, 2019.

[90] B. Tilocca *et al.*, "Comparative computational analysis of SARS-CoV-2 nucleocapsid protein epitopes in taxonomically related coronaviruses," *Microbes Infect.*, vol. 22, no. 4–5, pp. 188–194, 2020.

[91] C. A. Donnelly, M. R. Malik, A. Elkholy, S. Cauchemez, and M. D. Van Kerkhove, "Worldwide reduction in MERS cases and deaths since 2016," *Emerg. Infect. Dis.*, vol. 25, no. 9, pp. 1758–1760, 2019.

[92] Tu Yung-Fnag, "A Review of SARS-CoV-2 and the Ongoing Clinical Trials," *Int. J. Mol. Sci.*, vol. 21, no. 7, pp. 2657–2674, 2020.

[93] D. Yang and J. L. Leibowitz, "The structure and functions of coronavirus genomic 3' and 5' ends," *Virus Res.*, vol. 206, pp. 120–133, 2015.

[94] R. Lu *et al.*, "Genomic characterisation and epidemiology of 2019 novel coronavirus: implications for virus origins and receptor binding," *Lancet*, vol. 395, no. 10224, pp. 565–574, 2020.

[95] J. D. Cherry, "The chronology of the 2002-2003 SARS mini pandemic," *Paediatr. Respir. Rev.*, vol. 5, no. 4, pp. 262–269, 2004.

[96] J. Shang *et al.*, "Cell entry mechanisms of SARS-CoV-2," *Proc. Natl. Acad. Sci. U. S. A.*, vol. 117, no. 21, 2020.

[97] K. Mullis, F. Faloona, S. Scharf, R. Saiki, G. Horn, and H. Erlich, "Specific enzymatic amplification of DNA in vitro: the polymerase chain reaction. 1986.," *Biotechnology (Reading, Mass.)*, vol. 24. pp. 17–27, 1992.

[98] R. Scherberger, R., H. Kaess, and S. Brueckner, "Studies on the action of an anticholinergic in combination with a tranquilizer on gastric juice secretion in man," *Arzneimittel-Forschung/Drug Res.*, vol. 25, no. 9, pp. 1460–1463, 1975.

[99] C. Yuan *et al.*, "Viral loads in throat and anal swabs in children infected with SARS-CoV-2," *Emerg. Microbes Infect.*, vol. 9, no. 1, pp. 1233–1237, 2020.

[100] L. Chen *et al.*, "RNA based mNGS approach identifies a novel human coronavirus from two individual pneumonia cases in 2019 Wuhan outbreak," *Emerg. Microbes Infect.*, vol. 9, no. 1, pp. 313–319, 2020.

[101] D. Wang *et al.*, "Clinical characteristics of 138 hospitalized patients with 2019 novel Coronavirus-infected pneumonia in Wuhan, China," *JAMA - J. Am. Med. Assoc.*, vol. 323, no. 11, pp. 1061–1069, 2020.

[102] E. Tuaillon *et al.*, "Detection of SARS-CoV-2 antibodies using commercial assays and seroconversion patterns in hospitalized patients," *J. Infect.*, vol. 81, no. 2, pp. e39–e45, 2020.

[103] H. Ma *et al.*, "Serum IgA, IgM, and IgG responses in COVID-19," *Cell. Mol. Immunol.*, vol. 17, no. 7, pp. 773–775, 2020.

[104] M. C. Smithgall, M. Dowlatshahi, S. L. Spitalnik, E. A. Hod, and A. J. Rai, "Types of assays for SARS-CoV-2 testing: A review," *Lab. Med.*, vol. 51, no. 5, pp. e59–e65, 2020.

[105] A. Ghaffari, R. Meurant, and A. Ardakani, "COVID-19 serological tests: how well do they actually perform?," *Diagnostics*, vol. 10, no. 7, pp. 1–14, 2020.

[106] W. Liu *et al.*, "Evaluation of nucleocapsid and spike protein-based ELISAs for detecting antibodies against SARS-CoV-2," *medRxiv*, no. March, pp. 1–7, 2020.

[107] Z. Chen *et al.*, "Rapid and sensitive detection of anti-SARS-CoV-2 IgG, using lanthanide-doped nanoparticles-based lateral flow immunoassay," *Anal. Chem.*, vol. 92, no. 10, pp. 7226–7231, 2020.

[108] L. Cinquanta, D. E. Fontana, and N. Bizzaro, "Chemiluminescent immunoassay technology: what does it change in autoantibody detection?," *Autoimmun. Highlights*, vol. 8, no. 1, 2017.

[109] E. S. Theel, J. Harring, H. Hilgart, and D. Granger, "Performance characteristics of four high-throughput immunoassays for detection of igg antibodies against sars-cov-2," *J. Clin. Microbiol.*, vol. 58, no. 8, pp. 1–11, 2020.

[110] R. Lassaunière *et al.*, "Evaluation of nine commercial SARS-CoV-2 immunoassays," *medRxiv*, pp. 1–15, 2020.

[111] A. J. Jääskeläinen *et al.*, "Performance of six SARS-CoV-2 immunoassays in comparison with microneutralisation," *J. Clin. Virol.*, vol. 129, pp. 1–10, 2020.

[112] M. A. Black *et al.*, "Analytical performance of lateral flow immunoassay for SARS-CoV-2 exposure screening on venous and capillary blood samples," *J. Immunol. Methods*, vol. 489, pp. 1–7, 2021.

[113] I. Assay, S. Boise, P. C. Mathias, and L. Greninger, "Performance characteristics of the Abbott architect SARS-CoV-2 IgG assay and seroprevalence in Boise, Idaho," *J. Clin. Microbiol.*, vol. 58, no. 8, pp. 4–11, 2020.

[114] M. Infantino *et al.*, "Diagnostic accuracy of an automated chemiluminescent immunoassay for anti-SARS-CoV-2 IgM and IgG antibodies: an Italian experience," *J. Med. Virol.*, vol. 92, no. 9, pp. 1671–1675, 2020.

[115] M. Tré-Hardy, A. Wilmet, I. Beukinga, J. M. Dogné, J. Douxfils, and L. Blairon, "Validation of a chemiluminescent assay for specific SARS-CoV-2 antibody," *Clin. Chem. Lab. Med.*, vol. 58, no. 8, pp. 1357–1364, 2020.

[116] M. Nuccetelli, M. Pieri, F. Gisone, and S. Bernardini, "Combined anti-SARS-CoV-2 IgA, IgG, and IgM detection as a better strategy to prevent second infection spreading waves," *Immunol. Invest.*, vol. 00, no. 00, pp. 1–13, 2020.

[117] M. P. Cheng *et al.*, "Diagnostic testing for severe acute respiratory syndrome-related coronavirus 2: A narrative review," *Ann. Intern. Med.*, vol. 172, no. 11, pp. 726–734, 2020.

[118] A. M. Bernard and R. R. Lauwerys, "Continuous-flow system for automation of latex immunoassay by particle counting.," *Clin. Chem.*, vol. 29, no. 6, pp. 1007–1011, 1983.

[119] J. Qu, M. Chenier, Y. Zhang, and C. Xu, "A microflow cytometry-based agglutination

immunoassay for point-of-care quantitative detection of SARS-CoV-2 IgM and IgG," *Micromachines*, vol. 12, no. 4, pp. 1–9, 2021.

[120] T. Guo *et al.*, "Counting of escherichia coli by a microflow cytometer based on a photonic-microfluidic integrated device," *Electrophoresis*, vol. 36, no. 2, pp. 298–304, 2015.

[121] J. Jin and J. L. Zehnder, "Prozone effect in the diagnosis of lupus anticoagulant for the lupus anticoagulant-hypoprothrombinemia syndrome," *Am. J. Clin. Pathol.*, vol. 146, no. 2, pp. 262–267, 2016.

[122] J. Qu, Y. Zhang, M. Chenier, C. Q. Xu, L. Chen, and Y. Wan, "A transit time-resolved microflow cytometry-based agglutination immunoassay for on-site c-reactive protein detection," *Micromachines*, vol. 12, no. 2, pp. 1–7, 2021.

[123] W. N. W. Azman, J. Omar, T. S. Koon, and T. S. T. Ismail, "Hemolyzed specimens: Major challenge for identifying and rejecting specimens in clinical laboratories," *Oman Med. J.*, vol. 34, no. 2, pp. 94–98, 2019.

[124] A. S. Iyer *et al.*, "Persistence and decay of human antibody responses to the receptor binding domain of SARS-CoV-2 spike protein in COVID-19 patients," *Sci. Immunol.*, vol. 5, no. 52, pp. 1–13, 2020.

[125] W. Y. Wan, S. H. Lim, and E. H. Seng, "Cross-reaction of sera from COVID-19 patients with SARS-CoV assays," *medRxiv*, pp. 1–12, 2020.